Toward a Precision Measurement of the Theta_13 Mixing Angle with the Double Chooz Detectors

A Dissertation Presented for the
Doctor of Philosophy
Degree
The University of Tennessee, Knoxville

Ben Thomas Rybolt
May 2016

Abstract

Neutrinos are the most numerous and least understood particle in the universe. In the last few decades numerous experiments have been devoted to discovering their properties. The Double Chooz experiment was designed to make a precise measurement of θ_{13} [theta 13], the neutrino mixing parameter which describes flavor oscillations governing short baselines. To accomplish this measurement, two identical neutrino detectors have been deployed at a near and far baseline outside two commercial nuclear reactors. The neutrino flux and spectrum at the near and far detector sites will determine the disappearance of anti-neutrinos created inside the reactors.

I have contributed to the construction and commissioning of the near detector. I will describe the quality assurance tests of photomultiplier tubes which comprise the near detector. Additionally, I will describe quality checks of the first physics data coming from the completed detector, including neutrino selection and background determination. With two high quality detectors, Double Chooz will provide a precision measurement of θ_{13} in the coming year.

Finally, I demonstrate the ability of two identical neutrino detectors to locate a hidden nuclear reactor. As a real-world example, I use the initial data from the two Double Chooz neutrino detectors to successfully constrain the location of the reactor. Locating a hidden reactor is of interest to the nuclear non-proliferation community.

Table of Contents

Chapter I: Introduction 1
Chapter II: Neutrino Physics.. 3
Standard Model 3
Neutrino Oscillations and the Standard Model 4
Two Flavor Neutrino Oscillation Model 5
Three Flavor Neutrino Oscillation Model 8
Importance of θ_{13}.. 9
Chapter III: Experimental Observations of Neutrinos 11
The First Neutrinos.. 11
The First Solar Neutrinos 15
Cherenkov Detectors 17
Oscillation Search.. 22
Establishing Oscillation with Atmospheric Neutrinos.. 22
Establishing Oscillation with Accelerators 24
Establishing Oscillation with Reactor... 29
Mixing angle θ_{13} 35
Chapter IV: The Double Chooz Experiment 36
Detector Design 36
Overview 36
Scintillator 40
Inner Detector Photomultiplier Tubes.. 45
Trigger System 50
Reconstruction Algorithms 50
Vertex reconstruction 50
Energy Reconstruction.. 51
Muon track reconstruction 59
Reactor anti-neutrino Flux Prediction 61
Predicting the anti-neutrino Flux.. 61
Chapter V: PMT System Installation and Testing... 65
Installation Contribution.. 65
IV PMT Tests.. 65
Inner Detector PMT Tests 71
In-situ PMT test and results.. 77
PMT installation Conclusions... 80
Chapter VI: Double Chooz Single Detector 83
Neutrino Signals.. 83
Background Signals 86
Accidentals.. 86
Lithium-9 and Helium-8 88

Fast Neutrons and Stopping Muons 93
Muons 93
Light Noise 94
One Detector θ_{13} results 99
Gadolinium 99
Hydrogen 107
Worldwide θ_{13} 109
Chapter VII: Two Detector Results 111
Two detector sensitivity 111
Near-Far Detector Similarities 112
Near-Far Detector Differences 115
Commissioning the trigger 118
Optimizing Muon Veto 122
Chapter VIII: Detecting a hidden reactor with two identical detectors 130
General formulism 130
Example using Double Chooz 135
One detector verse two discussion 138
Chapter VIII: Conclusions 139
List of References 140
Vita 143

List of Tables

Table 1: Distance from Reactor cores to Double Chooz Detectors 37
Table 2: Composition of Scintillators in Double Chooz Target and Gamma Catcher 40
Table 3: Gamma Spectroscopy results for Gd-Complex powder..................................... 41
Table 4: Radio purity results for PPO powder. Neutron Activation Analysis (NAA) and Atomic Activation Spectroscopy (AAS) are shown for Potassium in addition to the Gamma Spectroscopy (GeMPI). 42
Table 5: Detector PMTs rejected from installation in Near Detector 76
Table 6: Neutrons detected per hour for various of trigger conditions 121

List of Figures

Figure 1: Fundamental Particles in the Standard Model 3
Figure 2. Feynman diagram of the Electromagnetic force mediated by a photon exchange (left); Strong force mediated by a gluon exchange(center), and weak force mediated by a W^- exchange (right). 4
Figure 3: Oscillation Probabilities using $\Delta m_{13}^2 = 7.59x10^{-5}$ eV^2, $\Delta m_{32}^2 \approx \Delta m_{13}^2 = 2.32x10^{-3}$ eV^2, $\sin^2 2\theta_{12}$ =0.861, $\sin^2 2\theta_{23}$ =0.97, and $\sin^2 2\theta_{13}$ =0.1 . Black- υ_e , Blue -υ_μ and Red-υ_τ 9
Figure 4: Savannah River Detector. Tanks 1,2,3 contain liquid scintillator. Sandwiched between are tanks of Cadmium doped water. 12
Figure 5: Schematic of Savannah River Detector.. 13
Figure 6: Results from the Savannah River Experiment. 14
Figure 7: Solar Neutrino Spectrum 16
Figure 8:The Homestake Experiment located in Homestake Gold Mine in South Dakota. 19
Figure 9: Example of Vertex Reconstruction in SNO. Dots represent PMT light detection. 20
Figure 10: Sudbury Neutrino Observatory.. 21
Figure 11: Some of the 11,000 PMTs visible inside the Super-Kamiokande Detector 23
Figure 12: Super-Kamiokande data. Hatched data is assuming no oscillation and solid line includes oscillation with the best fit parameters. 24
Figure 13: Time structure of events in the near and far detector show well known beam structure.. 26
Figure 14: E_v distribution for μ-like events in the Super-K detector. Blue line is the un-oscillated prediction, and the red line is the oscillated predictions........................ 27
Figure 15: Fit Parameters of the K2K experiment. 28
Figure 16: Schematic of the KamLAND Detector 29
Figure 17: Ratio of observed to expected anti-neutrinos for reactor based neutrino detectors. Shaded region is the 95% CL of the Large Mixing Angle Hypothesis. 32
Figure 18: Neutrino oscillation analysis result of KamLAND. Dotted line at 2.6 MeV is the threshold for this analysis in order to neglect contributions from geo-neutrinos... 33
Figure 19: L_0 is the flux weighted average distance from the reactor. Strength of mixing angle Θ_{12} is manifest as the depth of the valley. The frequency is determined by Δm_{12}. 34
Figure 20: Aerial View of the Double Chooz site 38
Figure 21: Schematic of the Double Chooz Far Detector 39
Figure 22: Attenuation Length of Liquid in the Gamma Catcher.................................... 43
Figure 23: Scintillation photon emission time distribution for beta excitation in the Gamma Catcher (GC) and neutrino target(Target). 44

Figure 24: (Left) Hamamatsu R7801 PMT with acrylic mounting and Magnetic shield. A portion of the magnetic shield is removed to make the picture. (Right) Bare Detector PMT. 45
Figure 25: Hamamatsu defined time response for Detector PMTs. 46
Figure 26: Detector PMT efficiency from Hamamatsu 47
Figure 27: Single Photo-electron Spectrum data shown in red with the fit function in black. The fit is two Gaussians (green and yellow) and a decaying exponential (blue). 48
Figure 28: Output of PMT/(Output with no B field) for various mu-metal positions and external magnetic fields. 49
Figure 29 Schematic of the Double Chooz Electronics 50
Figure 30: 60Co source in the center of the detector. Black does are back ground subtracted data and red line is a Gaussian fit. 52
Figure 31: F_V = – ln(Likelihood function) Events to the left of blue line are point like i.e. n-Gd captures. Events to the right are not as point like i.e. Fast Neutron or Stopping muons 53
Figure 32: Typical pulse from the Flash ADC 54
Figure 33: Charge non-linearity caused by quantization effects of the flash ADC. 55
Figure 34: Uniformity Correction Map obtained from fitting the 2.223 MeV n-H peak from spallation Neutrons. 56
Figure 35: Effect of Light Non-Linearity (LNL) due to Birk's coefficient. 57
Figure 36: Time stability of the energy reconstruction for various sources. 58
Figure 37: Resolution of Muon tracking compared to OV reconstructed tracks for scintillation dominated. 59
Figure 38: Red and Purple lines represent the wave front of scintillation photons created by a muon (blue line). The intersection of the wave front with the PMTs on the buffer wall define expected start times for each PMT for a given muon track. 60
Figure 39: Binding Energy per Nucleon Curve. 61
Figure 40: Ab Initio calculation for U-235 is shown in red. Green and Blue are calculated using the Beta Conversion Method. Data point show similar shaped to the Ab Initio Calculation 63
Figure 41: Neutrino flux and cross section are convoluted to obtain the expected detected spectrum. 64
Figure 42: UT designed PMT testing Station consisting of a black box, oscilloscope, readout electronics and DAQ system. 66
Figure 43: IV PMT pulse with reflection due to faulty base 67
Figure 44: Gain of IV PMTs. Blue was measured in Tubingen and Red was measured in the Near Lab at Chooz. 68
Figure 45: Example of IV PMT spectrum with pedestal and poor SPE resolution 69
Figure 46: LED Efficiency Scan with PMT with similar encapsulation to IV PMT 70
Figure 47: SPE spectrum of Detector PMT self-triggered at ¼ SPE with fixed trigger pedestal. 71

Figure 48: Pre-Installation Test Results for Detector PMT Gains 72
Figure 49: Pre-Installation Test Results for Detector PMT Dark Rates............................ 73
Figure 50: Pre-Installation Test Results for Detector Peak-to-Valley Ratios 74
Figure 51:Testing Result for Detector PMT Peak-to-Valley Ratio and σSPE 75
Figure 52: Preparing for In-Situ tests by covering the detector put with black plastic (top) and preparing 8 Channel Readout electronics (bottom).. 78
Figure 53: Pre-Installation vs. In-situ PMT gain (only "good" cables are plotted) 79
Figure 54: Photos of the two types of signal cables 80
Figure 55: Pedestal widths of Near Detector PMTs. "Foil" cables show more noise pick-up than braided cables 81
Figure 56: Coherence between foil cables (teal and purple) and proper shielding of a braid cable shows very little noise (yellow)... 82
Figure 57: Inverse Beta Decay schematic 83
Figure 58: Time between IBD Prompt and Delay for Gd selection (left) and H selection(right). The n-Gd capture has a mean capture time of 30us while the n-H has a capture time of ~200 us.. 84
Figure 59: Gd Natural abundance and thermal Neutron Capture Cross sections. 85
Figure 60: Singles spectrum in the Far Detector. Commonly occurring radioactive elements dominate the spectrum. 87
Figure 61: Possible end products of Spallation on ^{18}O. Long dash denotes a stable isotope and short dash denotes long lived isotope, + denotes an isotope that undergoes β^+ decay.. 89
Figure 62: Time between Muon and Prompt for the Li-enriched sample....................... 90
Figure 63: Events selected as ^9Li by the lithium likelihood veto. Overlaid in red is a Monte Carlo prediction of the ^9Li decay spectrum. 91
Figure 64: Lateral distance profile for Muons above 600 MeV and the following IBD candidates. The best fit function is a decaying exponential convoluted with a Gaussian to take into account vertex reconstruction smearing of the Muon track and the Li-9 event. 92
Figure 65: A sample of epoxy used in the PMT base is glowing when high voltage is applied. 94
Figure 66:QRMS and RMSTstart cut is defined by the black line. Two populations are seen with Light Noise is defined as events to the right of the line and physics events to the left. 95
Figure 67: Light Noise and Physics event rate for the first two year data set of the Far detector.. 96
Figure 68: (Left) PMT base as it is in the Far detector. (Right) PMT base covered with black plastic to reduce light noise for the Near detector. 97
Figure 69: (Left) Light noise variables for the Far detector. (Right) same variables for the Near detector. Light Noise is greatly reduced in the ND due to the black plastic covering the base... 98

Figure 70: Correlation distance between prompt and delay for IBD signal and accidentals. This plot justifies the 100 cm cut in ΔR. 100
Figure 71:Population of Delay signals before FuncV cut is applied. The events to the left of the blue line are neutron captures on Gadolinium while to the right are events caused by fast neutrons or stopping muons. 101
Figure 72: Distributions of the prompt and delay events. Colored lines show the events rejected by the various selection criteria. 103
Figure 73: Observed neutrino spectrum with background overlaid with the best fit of $\sin^2 2\theta_{13}$. 104
Figure 74: Black points show ratio of background subtracted data to un-oscillated prediction. Red line is the expectation assuming the best fit value of $\sin^2 2\theta_{13}$=0.09. 105
Figure 75: Excess in the 4.25-6 MeV window scales with the reactor power. 106
Figure 76: Performance of IBD selection using neutron capture on Hydrogen. ANN cut reduces drastically reduces the accidental background. 107
Figure 77: (top) Final IBD selection with backgrounds. (bottom) Result of observed/predicted ratio for different energy bins. Similar shape is seen for neutrino disappearance and 4-6 MeV excess in both n-H and n-Gd selections. ... 108
Figure 78: Currently Running θ_{13} experiments. 109
Figure 79: Timeline of World-Wide Reactor based neutrino oscillation. Open point indicate the result is from Rate+Shape fit while close point is from Rate Only fit. Dashed lines indicate n-H analysis while solid lines are for n-Gd only.................. 110
Figure 80: Projected sensitivity with near and far detector. Assumed cosmogenic backgrounds are scaled with the increased muon rate in the near detector. 111
Figure 81: Low Energy Singles in the Near and Far detector taken from two 1 hour runs and normalized to the total singles rate. 113
Figure 82: Singles within 1 ms after a muon. Identical Energy response is seen in near and far detectors. 114
Figure 83: (left) Singles and Light Noise events in Far detector from a one hour run. (right) Singles and Light Noise in Near Detector for one hour run. Events which satisfy light noise cuts are mostly occurring in the top of the detector in the near. 116
Figure 84: Vertex of Light Noise events in 1 hour run of Near Detector. Events are reconstructed at the face of individual PMTs in the top of the detector. 117
Figure 85: Uniformity correction maps for Near and Far detector. Differences are due to difference in scintillator properties. 118
Figure 86: Schematic of the DDR trigger. The trigger threshold is increased for 50μs after a muon and then returns to the nominal level. 119
Figure 87: Performance on trigger configuration. Hydrogen captures (left) and Gadolinium captures (right). Both DDR and FDI triggers show decreased neutron detection efficiency compared to MOD trigger. 120

Figure 88: Neutrino candidates in one month data set of near detector. Events to the left of the horizontal line at 1 ms are vetoed by the after muon veto. A clear excess highlighted in orange is seen after the muon. 123
Figure 89: Time after muon verse prompt Energy of IBD candidates. Neutrinos coming from the reactor should provide a constant background as seen for times > 1 ms . Muon induced IBD candidates are seen at times < 1 ms. 124
Figure 90: IBD prompt candidates in 1 month data of Near Detector. Different color histograms correspond to different time windows after the previous muon. 125
Figure 91: ΔT distributions for the two muon classes and the IBD prompt. (blue) Veto Muon plotted when Buffer Muon veto of 1 ms is applied and (red) Buffer Muon plotted when Veto Muon veto time of 1 ms is applied. 127
Figure 92: Energy Spectra for alternative muon veto definitions. 128
Figure 93: IBD candidates from the 1 month sample of the Near Detector. Standard IBD candidates are shown in red with the additional candidates from a shortened muon veto time in black. The sum of the two is in blue. 129
Figure 94: Neutrinos detected per day with the Double Chooz Far detector. 130
Figure 95: Direction of the vector that points from delay to prompt for the Double Chooz Far detector. (left) is data points while (right) shows Monte Carlo prediction with higher statistics. 131
Figure 96: Green circles show possible reactor locations for different values of A. 133
Figure 97: Schematic showing the position of reactors with possible minimum and maximum thermal powers. 134
Figure 98:Prompt Energy (MeV) of neutrino candidates from the preliminary “1 month” data set. 136
Figure 99: Schematic of the predicted location of the hidden reactor (blue line) with 1 sigma uncertainties (red lines) based on the rate measurement overlaid with the actual location of the reactors (R1 and R2). 137

Chapter I: Introduction

The 2015 Nobel Prize in physics was awarded to Takaaki Kajita of the Super-Kamiokande collaboration and Arthur B. McDonald of the SNO collaboration “for the discovery of neutrino oscillations, which shows that neutrinos have mass.” Their discoveries were made possible by detecting neutrinos from the sun in the case of SNO and from atmospheric muons in the case of Super-Kamiokande. For a detailed history of these experiments please see “Chapter III: Experimental Observations of Neutrino.” The oscillation effect that the two experiments observed was a large deviation from the no oscillation expectation of about 50% reduction in the observed neutrinos, and KamLAND further confirmed neutrino oscillation by detecting anti-neutrinos from 53 nuclear reactors in Japan. Double Chooz together with other next-generation neutrino experiments have developed a precision technique for measuring a much smaller oscillation effect.

The precision refinement of the Double Chooz experiment was achieved by design improvements from previous experiments. Instead of relying on theoretical calculations for the reactor neutrino spectrum and fluxes as KamLAND and CHOOZ did, Double Chooz constructed two identical detectors. One detector measures the close-range flux and the other measures the far-range flux. Since the effect of neutrino oscillation depends on the distance from the source, the flux in the close-range detector is independent of the oscillation parameter θ_{13}. Where SNO, Super-Kamiokande and KamLAND all rely on cosmogenic background suppression by being located in very deep mines, Double Chooz has been constructed at a shallow overburden. Shallow overburden has necessitated the development of new background rejection techniques. Background suppression is enhanced by doping the liquid scintillator with gadolinium. Compared to KamLAND, where neutrons are captured on hydrogen, the neutron capture on gadolinium provides a faster prompt-delay coincidence and a higher energy gamma cascade of the delay event. The higher energy gamma is well above the energy range of dominating backgrounds.

I have contributed in the construction and commissioning of the Double Chooz near detector and the first analysis using both near and far detectors and thus to the development of more precise neutrino detection technique. Details of my contribution can be found in “Chapter V: PMT System Installation and Testing” and “Chapter VII: Two Detector Results”.

Why study neutrino physics? There are many unanswered questions in the field of physics: What is dark matter? What is dark Energy? Why is there more matter than anti-matter? Are there more fundamental particle?

Neutrinos could potentially provide or be a key to answers of these questions. Before these questions can be answered the basic properties of neutrinos must be established. The current generation of high precision neutrino detectors is laying the foundation for the discussion about what future experiments should be built. Furthermore, we are approaching an age where neutrino detection may enter the realm of practical application. One such application is of interest to the nuclear non-proliferation community. I have demonstrated some lessons that can be learned by the Double Chooz experiment in the section entitled: “Chapter VIII: Detecting a Hidden Reactor with Two Identical Detectors.”

Chapter II: Neutrino Physics

Standard Model

All matter is made of combinations of twelve fundamental particles. The particles are fermions and they are grouped into Quarks and Leptons (Figure 1). To date there have been 100's of particles detected by particle colliders and every one can be described by only twelve fundamental building blocks. This is one of the great successes of the standard model.

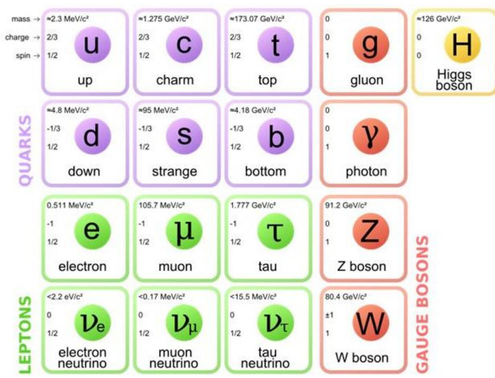

Figure 1: Fundamental Particles in the Standard Model

Within the standard model: electromagnetic, weak and strong forces are all mediated by particles called gauge bosons. In the simplest standard model all force mediators are massless; however this situation does not match observations. A massless force mediator results in a force that can reach infinitely far in space. Only the electromagnetic force and gravity exhibit this behavior. Likewise the photon is observed to be massless. The weak force occurs only at short distances which implies that the weak force mediators, the $W^{\pm}$ and Z bosons, have mass. The $W^{\pm}$ and Z bosons have been measured in the lab with masses of ~80 GeV/c^2. Using the Heisenberg uncertainty relation

Equation 1

$$\Delta x \Delta p \geq \frac{\hbar}{2}$$

one can estimate the range of the weak interaction which is ~10^{-18} m and this matches the experimental result.

The electromagnetic, weak, and strong force can all be represented with Feynman diagrams (Figure 2)

Each vertex with a gauge boson (γ, g, or W^-) represents the incoming particles interaction. Each interaction is defined by the Hamiltonian of the particular boson involved. If we know the Hamiltonians involved than we can predict the outcome of all possible particle interactions.

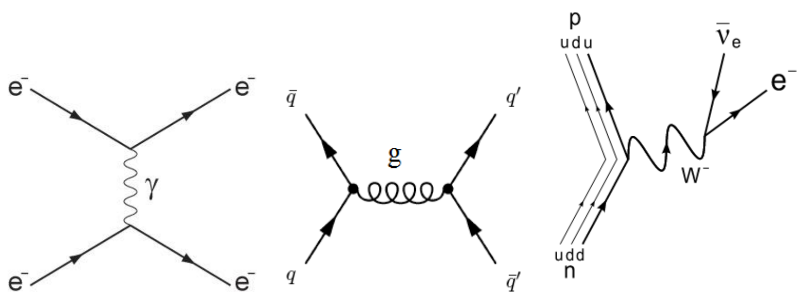

Figure 2. Feynman diagram of the Electromagnetic force mediated by a photon exchange (left); Strong force mediated by a gluon exchange(center), and weak force mediated by a W^- exchange (right).

Neutrino Oscillations and the Standard Model

In the standard model, it was assumed that neutrinos were massless. The observation of neutrino oscillation proves that neutrinos have a mass. Neutrino oscillations can determine the difference in mass of neutrino mass eigenstates, but they cannot determine the absolute mass of the neutrino. The absolute neutrino mass is presently unmeasured. The upper limit on the mass of the lightest neutrino is 2.2 eV [38], one million times lighter than the electron!

Neutrino oscillations arise because neutrino mass eigenstates are not identical to their flavor eigenstates. This makes them unique among the fundamental particles. Any quantum mechanical system can be described by a superposition of eigenstates. The eigenstates form a complete basis and have transformations well defined by the Hamiltonian of the system. Just as a function can be completely described by its Fourier transform, a quantum mechanical system can be completely described by a superposition of its eigenstates. For the neutrino there are two different bases that can describe the system: flavor eigenstates or mass eigenstates. Flavor states are the eigenstates of the Hamiltonian associated with the weak interaction and the mass eigenstates are associated with the propagation through free space.

In the Double Chooz experiment electron flavored anti-neutrinos are created in their flavor eigenstates via a weak interaction, beta decay. The neutrinos then propagate from the source to the detector as mass eigenstates which are mixtures of the flavor eigenstates. Upon arrival to the detector, only the electron flavored eigenstate is detected via Inverse Beta Decay. The μ and τ flavors go undetected in the detector and result in an electron flavored anti-neutrino disappearance.

Two Flavor Neutrino Oscillation Model

The full model of neutrino oscillation should include all three known neutrino flavors, but for simplicity I will first describe neutrino oscillation with only two flavors. The two flavor approximation is useful because it allows for a fundamental understanding with less complicated mathematical formulas and is a very good approximation for many experimental situations.

Since a neutrino can be represented in either a flavor or mass basis we would like to know how to transform from one basis to another. This can be represented by a mixing matrix $\mathbf{U_{fm}}$,

$$|f\rangle = (\boldsymbol{U_{fm}})|m\rangle = \left|\begin{matrix} e \\ \mu \end{matrix}\right\rangle = \begin{pmatrix} a & b \\ c & d \end{pmatrix} \left|\begin{matrix} m1 \\ m2 \end{matrix}\right\rangle$$

| f >- represents the flavor basis and m- represents the mass basis.

U_{fm} must be a unitary matrix, meaning:

$$\left(\boldsymbol{U^{*}_{fm} U_{fm}}\right) = \mathbf{1}$$

U_{fm} is a unitary matrix because it describes a transformation between two complete bases. The number of neutrinos remains constant independent of the bases by which it is described.

Since U_{fm} is a unitary matrix it can be parametrized as:

$$(\boldsymbol{T}) = \begin{pmatrix} a & \sqrt{1-a^2} \\ -\sqrt{1-a^2} & a \end{pmatrix} = \begin{pmatrix} cos\theta & sin\theta \\ -sin\theta & cos\theta \end{pmatrix} (\boldsymbol{T}) = \begin{pmatrix} a & b \\ -b & a \end{pmatrix}$$
$$= \begin{pmatrix} cos\theta & sin\theta \\ -sin\theta & cos\theta \end{pmatrix} \; where\; a^2 + b^2 = 1$$

U_{fm} has a single parameter either "a" or Θ. "a" has the physical meaning that a^2 and $1\text{-}a^2$ represent the proportion of m1 and m2 that mix to make the flavor eigenstate. For example, if a^2=0.2 than the flavor state e would be a superposition of 0.2 m1+0.8 m2. Θ is known as the mixing angle and is simply another way to parametrize the matrix. It has the convenient property that $\sin^2 \Theta + \cos^2 \Theta = 1$ and thus satisfies the unitary condition. Historically, neutrino mixing is represented by mixing angles rather than the parameter "a".

In addition to transforming from one basis to another we need to describe how neutrinos propagate through free space. A free neutrino of mass m (υ_m) traveling through free space can be described by a free particle propagator:

$$Prop\ \nu_m(E, T, p, L) = e^{-i(E\,T - \boldsymbol{p}\,L)}$$

E is the neutrino energy and p is the neutrino momentum, T is the lab time of flight and L is the lab distance of flight.
In the case of a relativistic particle the expression can be simplified since:

$$p = \sqrt{E^2 - m_i^2} \cong E - \frac{m_i^2}{2E} \quad and \quad T \cong L$$

In this limit the propagation through space as a mass eigenstate can be written:

$$Prop\ \nu_m(L, E) = e^{-i(\frac{m^2}{2E}L)}$$

The above result shows that if particles are propagating the same distance with the same energy but they have two different masses they will have different phases[1]. The phase difference between two mass eigenstates can be written as:

$$(E_1\,T - p_1\,L) - (E_2\,T - p_2\,L) = (E_1 - E_2)T - (p_1 - p_2)L$$

Using the general relativistic Energy-momentum relation:

$$E^2 = p^2 + m^2$$

The phase difference can be written:

$$(E_1 - E_2)\left[T - \frac{E_1 + E_2}{p_1 + p_2}L\right] + \frac{m_1^2 - m_2^2}{p_1 + p_2}L$$

In the case that E_1=E_2 the first term cancels and the resulting phase difference is:

$$\frac{m_1^2 - m_2^2}{p_1 + p_2} L = \frac{m_1^2 - m_2^2}{2p} L$$

Likewise if you do not assume that E_1=E_2 but instead consider that the neutrinos are relativistic such that E>>m. Then:

$$\frac{E_1+E_2}{p_1+p_2} \cong 1$$

And:

$$T \cong L$$

In this case the first term cancels again. So in either case the phase difference is:

$$\frac{m_1^2 - m_2^2}{2p} L$$

Since neutrinos are relativistic (which is the case for all past and present neutrino detectors) the expressions can be written:

$$\frac{m_1^2 - m_2^2}{2E} L$$

The probability that an electron neutrino is created, propagated a distance L and then detected in the muon flavor is given by:

$$Propability\ of\ \nu_e \rightarrow \nu_\mu = \left|\left(\boldsymbol{U_{fm}^*}\right)(Prop\ \nu_m(L,E))\left(\boldsymbol{U_{fm}}\right)\right|^2 = sin^2 2\theta\ sin^2 \frac{\Delta m^2}{2E} L$$

The right U_{fm} term represents a transformation from the electron flavor state into the mass eigenstates. Once in the mass eigenstates the neutrinos propagate according the Propagator term. Finally, only the electron flavor is detected and so U_{fm}^* transforms the propagated mass states back into the flavor eigenstates.

In the case of the Double Chooz experiment an electron anti-neutrino is created, propagated through space a distance L and then detected via its electron flavor. The probability of detecting the electron flavor after a propagation of distance L with energy E is shown in Equation 2.

Equation 2: Two flavor neutrino oscillation probability for $\boldsymbol{\nu_e} \rightarrow \boldsymbol{\nu_e}$

$$Propability\ of\ \nu_e \rightarrow \nu_e = 1 - Propability\ of\ \nu_e \rightarrow \nu_\mu = 1 - sin^2 2\theta\ sin^2 \frac{\Delta m^2}{2E} L$$

Three Flavor Neutrino Oscillation Model

To do a full treatment of neutrino oscillations all three neutrino flavors must be included. The derivation is analogous to the 2x2 case above but the matrix is a 3x3. The mixing between flavor and mass states is represented by the Pontecorvo-Masaki-Nakagawa-Sakata (PMNS) matrix [1].

$$U_{fm} = \begin{pmatrix} U_{e1} & U_{\mu 1} & U_{\tau 1} \\ U_{e2} & U_{\mu 2} & U_{\tau 2} \\ U_{e3} & U_{\mu 3} & U_{\tau 3} \end{pmatrix}$$

Each entry in the PMNS matrix describes the contribution of a mass state to a particular flavor state. For example, U_{e1}^2 represents the percentage of the first mass state contributing to the e flavor state. Likewise U_{e2}^2 represents the percentage of the second mass state contributing to the e flavor state. Just as we used a convenient parametrization in the 2x2 case, this matrix can be parametrized to have three mixing angles and one phase parameter corresponding to CP-violation (an additional parameter could be added if the neutrino is a Marjorana particle but I will discuss this in a later section). The parametrized version of the PMNS is chosen because in many experimental situations most of the terms can be ignored. In its common parametrization the PMNS matrix is:

Equation 3: Parametrized PMNS matrix

$$\mathbf{U_{fm}} = \begin{bmatrix} \mathbf{1} & \mathbf{0} & \mathbf{0} \\ \mathbf{0} & \boldsymbol{c_{23}} & \boldsymbol{s_{23}} \\ \mathbf{0} & \boldsymbol{-s_{23}} & \boldsymbol{c_{23}} \end{bmatrix} \times \begin{bmatrix} \boldsymbol{c_{13}} & \mathbf{0} & \boldsymbol{s_{13}e^{-i\delta}} \\ \mathbf{0} & \mathbf{1} & \mathbf{0} \\ \boldsymbol{-s_{13}e^{i\delta}} & \mathbf{0} & \boldsymbol{c_{13}} \end{bmatrix} \times \begin{bmatrix} \boldsymbol{c_{12}} & \boldsymbol{s_{12}} & \mathbf{0} \\ \boldsymbol{-s_{12}} & \boldsymbol{c_{12}} & \mathbf{0} \\ \mathbf{0} & \mathbf{0} & \mathbf{1} \end{bmatrix}$$
$$= \begin{bmatrix} \boldsymbol{c_{12}c_{13}} & \boldsymbol{s_{12}c_{13}} & \boldsymbol{s_{13}e^{-i\delta}} \\ \boldsymbol{-s_{12}c_{23} - c_{12}s_{23}s_{13}e^{i\delta}} & \boldsymbol{c_{12}c_{23} - s_{12}s_{23}s_{13}e^{i\delta}} & \boldsymbol{s_{23}c_{13}} \\ \boldsymbol{s_{12}s_{23} - c_{12}c_{23}s_{13}e^{i\delta}} & \boldsymbol{-c_{12}s_{23} - s_{12}c_{23}s_{13}e^{i\delta}} & \boldsymbol{c_{23}c_{13}} \end{bmatrix}$$

Where: $\boldsymbol{c_{ij}} = cos\theta_{ij}$, $\boldsymbol{s_{ij2}} = sin\theta_{ij}\ and\ \delta = CP\ violating\ phase$

If the phase, δ, is non-zero it means that neutrinos and antineutrinos will behave differently in their oscillation amplitudes. So far experimental evidence shows that δ is consistent with zero but there is significant effort in the field to design future experiments to measure this more precisely.

The mixing angles θ_{12} and $\theta_{23,}$ have been measured within the past two decades (see "Chapter III: Experimental Observations of Neutrinos"). The purpose of the Double Chooz experiment is to make a precision measurement of the mixing angle θ_{13}. If we take into account the best measurements of the mixing angles and assume that δ=0 we can plot the expected neutrino oscillation.

The frequency of oscillation is determined by the Δm^2 term from Eq. 1. The fast oscillation is due to Δm_{13}^2 and the slow oscillation is due to Δm_{12}^2 and Δm_{23}^2. The maximum amplitude of the oscillation is determined by the mixing angles. The small amplitude of the fast oscillations is determined by the smallness of θ_{13} while the large amplitude oscillations are low frequency are determined by θ_{12} and θ_{23}.

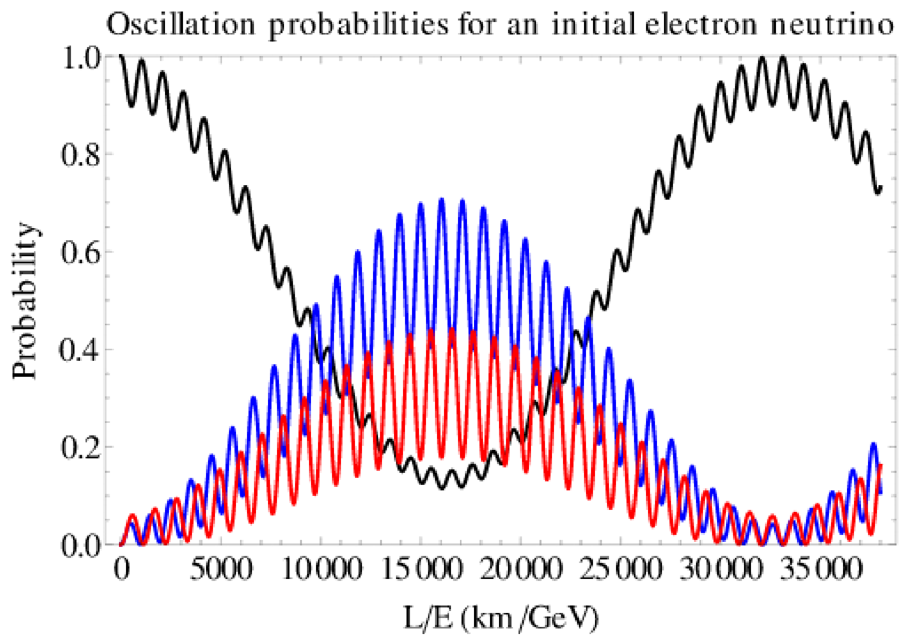

Figure 3: Oscillation Probabilities using Δm_{13}^2 = 7.59x10^{-5} eV^2, $\Delta m_{32}^2 \approx \Delta m_{13}^2$= 2.32x10^{-3} eV^2, $\sin^2 2\theta_{12}$ =0.861, $\sin^2 2\theta_{23}$ =0.97, and $\sin^2 2\theta_{13}$ =0.1 . Black- υ_e , Blue -υ_μ and Red-υ_τ

Importance of ϑ_{13}

Only recently has there been any experimental evidence to suggest that θ_{13} was not equal to zero. If θ_{13} =0, then CP violation will not have an impact on neutrino oscillations. To see this fact one only needs to examine Equation 3 and observe that every place that the CP violating phase δ appears there is also a $\sin\theta_{13}$ term. If $\sin\theta_{13}$=0 or is negligibly small, then then neutrino oscillations are independent of δ. In 2012 the Double Chooz collaboration published a measurement of $\sin^2 2\theta_{13}$ =0.086 ±0.016 (stat) ±0.040 (sys). This measurement provided an indication that θ_{13} was greater than zero

[2]. Currently there is ongoing effort to make a precise measurement of $\theta_{13.}$ The precise measurement is an important input toward designing experiments to measure CP violation.

Chapter III: Experimental Observations of Neutrinos

The First Neutrinos

The Neutrino was first proposed in a letter sent by Wolfgang Pauli to The University of Tubingen in 1930 [3]. Pauli proposed the neutrino, which he called "neutron", in order to explain the continuous beta decay spectrum that was observed at that time. If beta decay only involved two particles then the electron and nuclear recoil should share the total energy and the electron would carry most of the energy due to kinematics. However, if there was a third particle in the interaction, then the electron could share some energy with this unknown particle and thus have a continuous energy spectrum. He proposed that the neutrino was a fermion with no electric charge and that it should penetrate matter in a way that made it undetectable at that time. Pauli said, "I have done a terrible thing, I have postulated a particle that cannot be detected."

The first neutrino was detected in 1953 by Reines and Cowan [4] at the Hanford nuclear reactor site in Washington State. In 1956 a follow-up experiment was conducted at the Savannah River Site in South Carolina. The experiment at Savannah River, now known as the Reines-Cowan neutrino Experiment, confirmed what was observed in Hanford. In 1995 Reines was awarded the Nobel Prize in Physics for the first detection of the neutrino.

The Savannah River Detector consisted of three tanks of liquid scintillator instrumented with 110 photomultiplier tubes each (Figure 4). Between the liquid scintillator tanks are two target tanks of Cadmium Chloride dissolved in water. The mechanism of detection was inverse Beta Decay:

$$\bar{\nu} + p \rightarrow e^{+} + n$$

When an anti-neutrino from the nuclear reactor interacts with a Hydrogen nucleus in the water target, a positron and neutron are created (Figure 5). The positron annihilates with an electron and the resulting gamma rays can travel into the scintillator tanks. Simultaneously, the neutron is thermalized and absorbed on Cadmium providing a 9 MeV gamma ray. The positron annihilation and the 9 MeV gamma signal have a characteristic time delay that allows the signal to be separated from the background radiation. This same detection technique is employed in current reactor-based neutrino oscillation experiments such as Double Chooz, RENO, and Daya Bay.

The Savannah River Experiment was able to take data with the nuclear reactor on and off to show that the signal was coming from the reactor. To rule out other sources of background they did runs with additional neutron and gamma shielding and were able to show that the signal was unaffected.

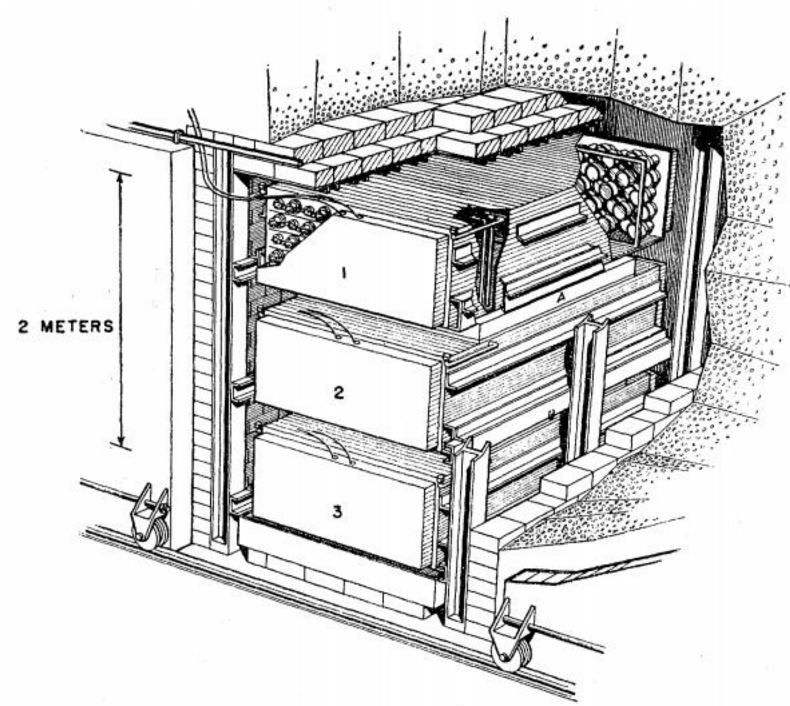

Figure 4: Savannah River Detector. Tanks 1,2,3 contain liquid scintillator. Sandwiched between are tanks of Cadmium doped water.

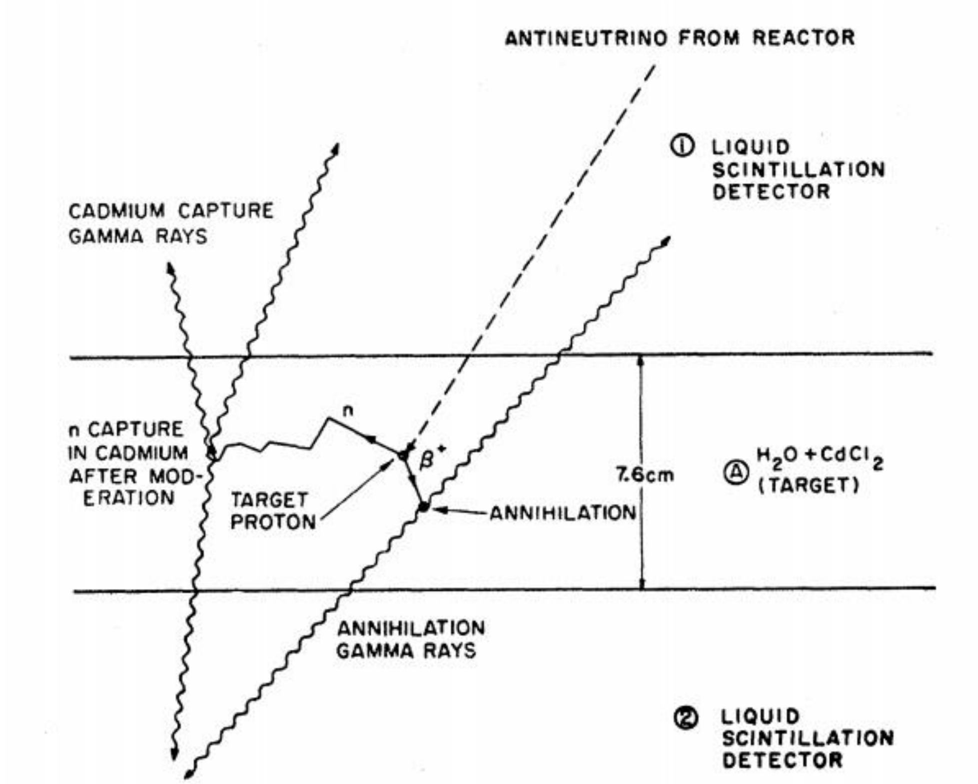

Figure 5: Schematic of Savannah River Detector

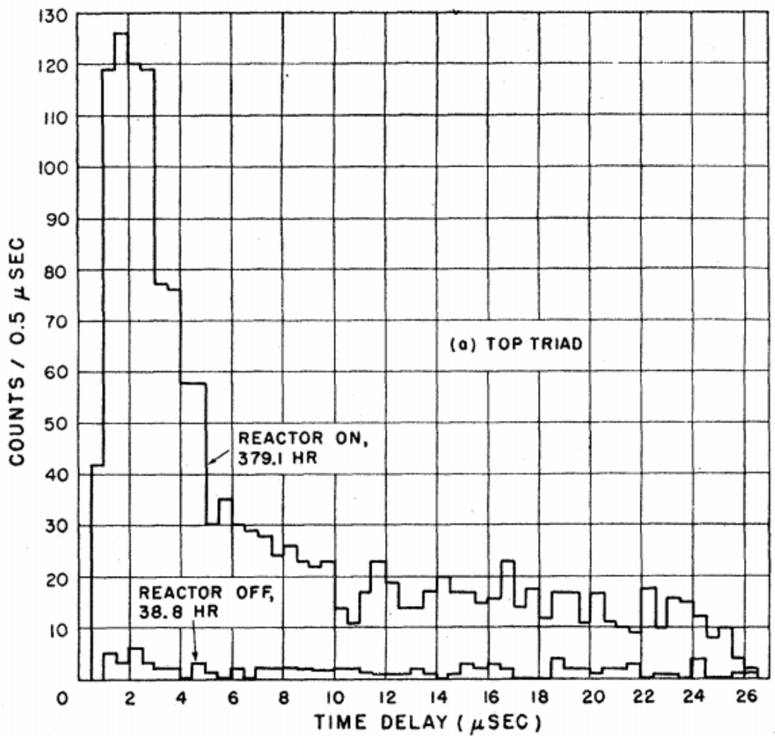

Figure 6: Results from the Savannah River Experiment.

Twenty-six years after Pauli proposed an undetectable particle Reines and Cowan detected neutrinos from a nuclear reactor, and thus opened the field of neutrino physics.

The First Solar Neutrinos

The first solar neutrinos were observed in the 1970s using radiochemical detection techniques. The flux of neutrinos coming from the Savannah River Reactor was ~10^{14} υ /(s cm^2.) The solar neutrino flux is predicted to be ~6 x 10^{10} υ/(s cm^2) ten thousand times smaller than the reactor flux. The neutrino counting rate at Savannah River was 2.8 counts/hour. To detect solar neutrinos a much larger detector was needed. Making the situation even more difficult is the fact <99% of solar neutrinos [5] (Figure 7) have less than the 1.8 MeV of energy required to do inverse beta decay. Not only is a large detector needed, but a new detection method.

The Homestake Experiment was started in 1968 with the purpose of detecting solar neutrinos. The Homestake Experiment [6] was located in the Homestake mine in South Dakota with 4200 m.w.e. overburden, and contained 615 metric tons of tetrachloroethylene (C_2Cl_4), a common household cleaner. The detection mechanism in this experiment was the transmutation of chlorine to argon through the interaction:

$$\nu_e + {}^{37}_{17}Cl \rightarrow {}^{37}_{18}Ar + e^-$$

Electron neutrinos, provided by the sun, can interact with a neutron in the chlorine nuclei to form a proton and an electron. The energy transfer from the neutrino to the proton is smaller than the proton binding energy so it remains inside the nucleus. Chemically, the chlorine changes to argon. This reaction has the advantage over inverse beta decay (IBD) in that its threshold is 0.814 MeV compared to 1.8 MeV for IBD..

At periodic intervals the tank holding the tetrachloroethylene was purged with helium in order to collect the newly created Argon atoms. The argon was then separated and transported with high efficiency [7] to a particle counter where it decayed with a half-life of 35 days and was counted. For each argon decay count, there must have been a neutrino interaction somewhere inside the tank. Argon can be produced in the tank by other mechanisms such as

$$p + {}^{37}_{17}Cl \rightarrow {}^{37}_{18}Ar + n$$

where the proton is provided from a muon interaction. This type of muon-induced background was reduced by providing the detector with the maximum available overburden. Since muons are charged particles they lose energy as they travel through

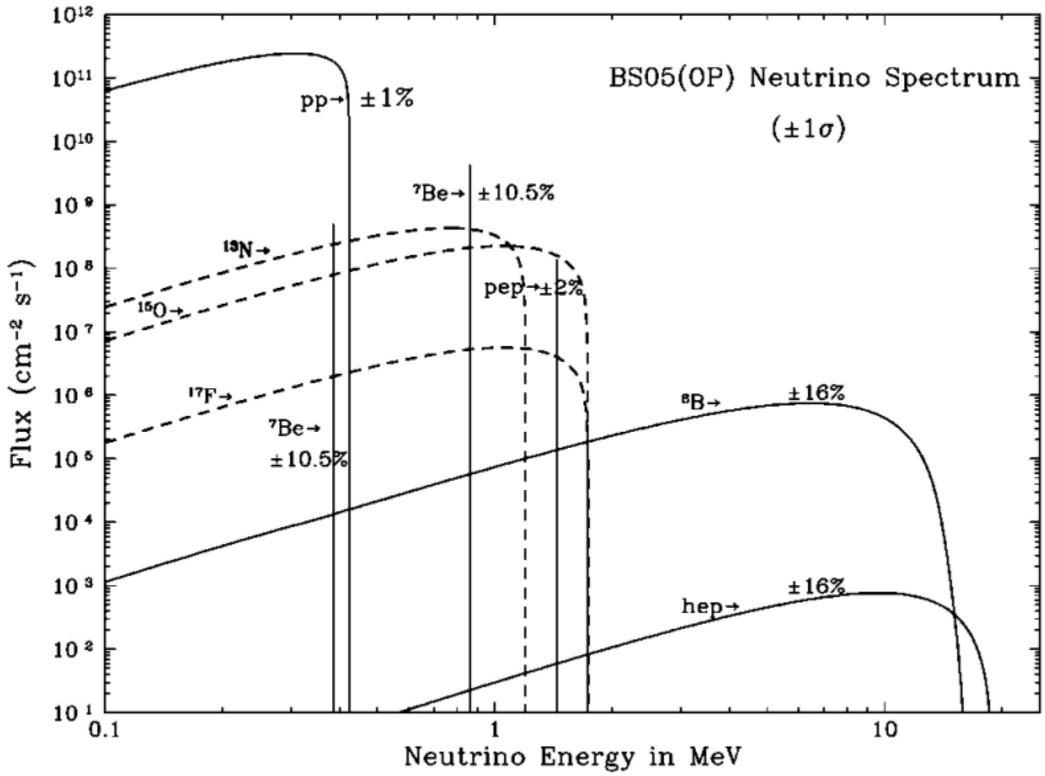

Figure 7: Solar Neutrino Spectrum

the Earth whereas the un-charged neutrinos will be unaffected. Radiochemical detection has the advantage that there is a high efficiency to detect even a small number of events. The target volume can be very large because it does not need to be instrumented with photo detectors as is the case for scintillation based experiments. The distinct disadvantage is that you only learn information on the rate of interaction averaged over the length of each run but there is no way of knowing when or where each interaction took place and there is no way to measure the energy of the neutrino. Despite these limitations, the Homestake Experiment was able to measure the flux of solar neutrinos and found that it was 2.56 ±.016 SNU. An SNU (solar neutrino unit) is the flux required to produce 10^{-36} neutrino interactions per second per target atom. The predicted value based on solar models was 9.3± 1.3 SNU. This discrepancy became known as the solar neutrino anomaly and was resolved with future neutrino experiments and the introduction of neutrino flavor oscillations.

Cherenkov Detectors

In 1991 the Sudbury Neutrino Observatory (SNO) resolved the solar neutrino anomaly [8]. They achieved this by employing a heavy waCherenkov Detector and three mechanisms of neutrino interaction.

a) $\nu_e + d \rightarrow p + p + e^-$ (charged current)

b) $\nu_x + d \rightarrow p + n + \nu_x$ (charged current)

c) $\nu_x + e^- \rightarrow \nu_x + e^-$(neutral current)

Mechanism a) is a charged current interaction; the virtual boson being exchanged in the interaction is a charged W^+. Both inverse beta decay, which was used to detect the first neutrinos, and the radiochemical experiments are charged current interactions. SNO was unique in that in addition to charge current interactions it was also able to detect neutral current interactions by mechanism b). Neutral current interactions are mediated by the exchange of a neutral particle $Z_{0.}$ Charge current reactions are only sensitive to electron flavored neutrinos whereas neutral current reactions are sensitive to all flavors of neutrinos. SNO was also able to detect neutrinos by mechanism c) elastic scattering with electrons. This process is also sensitive to all neutrino flavors but has heightened cross section to electron neutrinos.

The SNO detector was located in a mine in Sudbury, Ontario with a depth of 6010 m.w.e. Its main detector volume was filled with ultrapure heavy water (D_2O) and encased in a transparent acrylic vessel. The vessel was surrounded by a PMT support system which held 9456 20-cm PMTs and the entire detector was surrounded by water. Cherenkov detectors produce light when charged particles move faster than the speed of light in the medium. The particles must slow down in this situation and do so by emitting Cherenkov light in the forward direction. Cherenkov light is detected as a light cone by the PMTs. The vertex of interaction can be reconstructed by examining the pattern of light detected by the PMTs.

The initial results from the SNO detector compared the flux of neutrinos coming from the sun via the Charge Current interaction and the Elastic Scattering interaction. If we assume that there is no neutrino oscillation you would expect the fluxes on each interaction would be identical. If ν_e are allowed to oscillate into ν_μ and ν_τ the flux measured by Charge Current will be decreased and the flux by Elastic Scattering will be enhanced. The SNO detector reported a flux measured by Charge Current of $1.75\pm0.25 \times 10^6\ cm^{-2}\ s^{-1}$ and a flux measured by Elastic Scattering of $2.39\pm0.5\times 10^6\ cm^{-2}\ s^{-1}$. The difference in flux was the first direct evidence of solar neutrino oscillations.

The SNO collaboration did a follow-up study where they doped the heavy water with salt (NaCl) allowing an increased efficiency in detecting the neutral current events [9]. Neutrons created in the interaction could be captured by ^{17}Cl in the salt and result in multiple gammas as the ^{18}Cl de-excites. The detector could measure Cherenkov light produced by Compton electrons scattering off the gamma. These events can have more than one Compton electron and are easy to distinguish from the electron scattering events. In this phase they report the flux ratio of (charge current /neutral current) =$0.3 \pm 0.0510^6\ cm^{-2}\ s^{-1}$. The result can be understood to mean that ~1/3 of the ν_e coming from the sun are detected on earth as ν_e and ~2/3 have oscillated into ν_μ and ν_τ.

The SNO result resolved the tension between the solar neutrino flux predictions based on neutrino detection and Solar Modeling. At this point in history it was clear that neutrinos oscillate in flavor as they travel through space but the details of the oscillations were yet to be determined. Some of the questions that remained for future experiments were: Do other neutrino flavors oscillate? What is the frequency of oscillation? What is the amplitude? Since electron neutrinos oscillate flavors do anti-electron neutrinos oscillate in the same way? Is oscillation only between three flavors or can there be more flavors? Future experiments were designed to answer these questions and will be the focus of the next section.

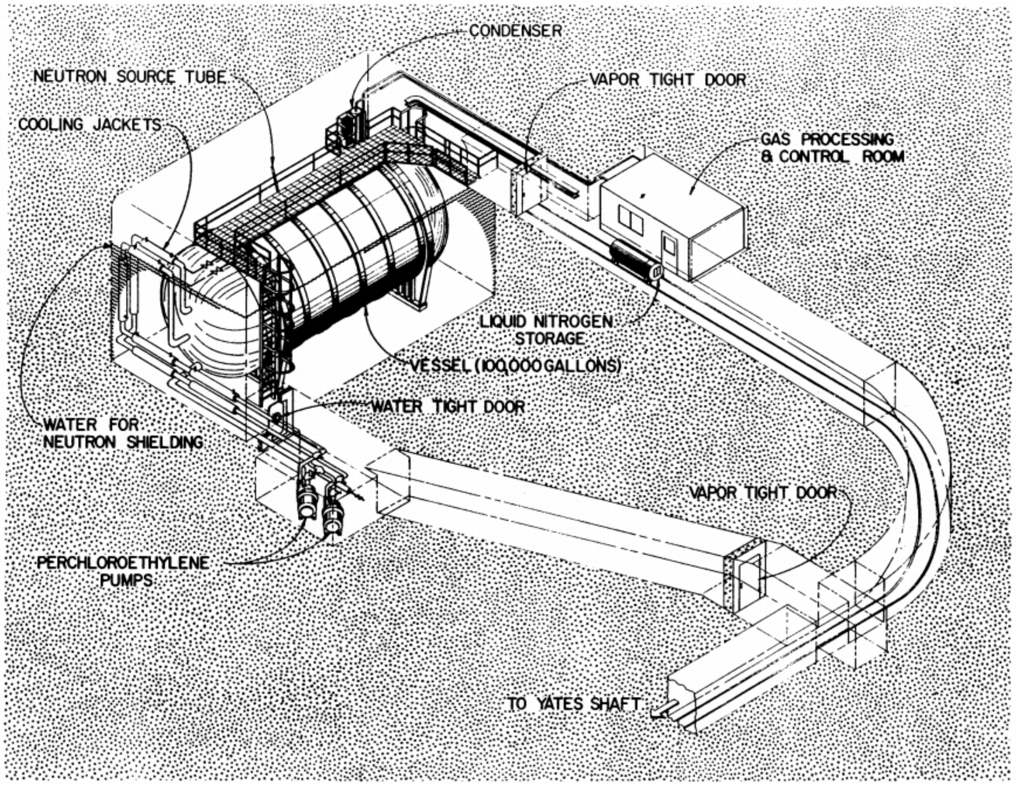

Figure 8:The Homestake Experiment located in Homestake Gold Mine in South Dakota.

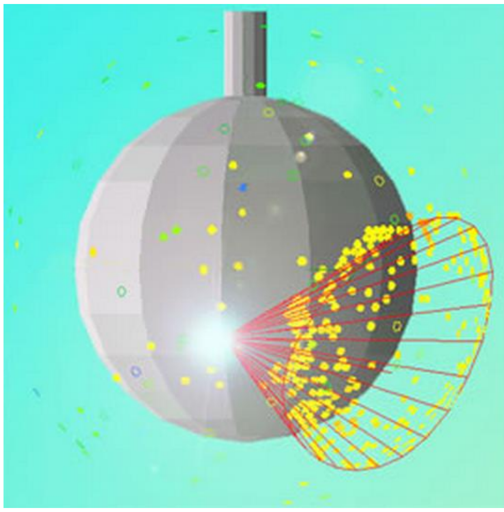

Figure 9: Example of Vertex Reconstruction in SNO. Dots represent PMT light detection.

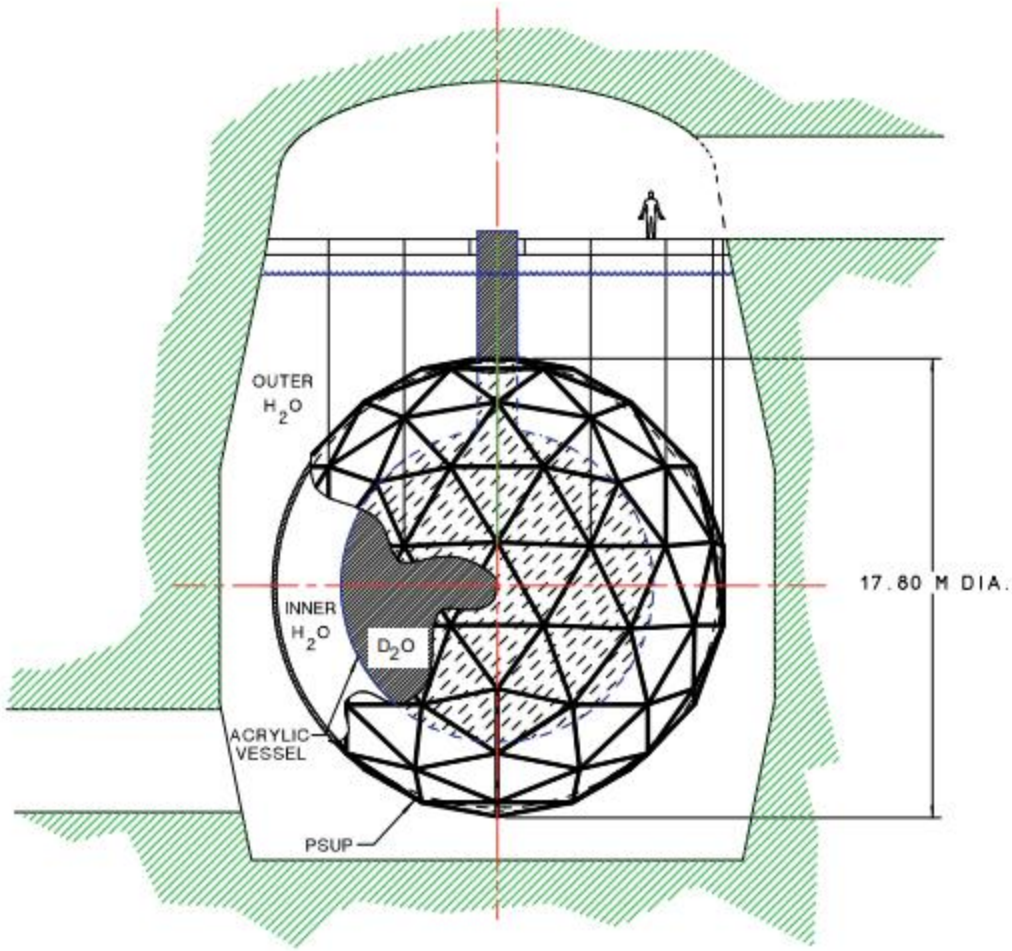

Figure 10: Sudbury Neutrino Observatory

Oscillation Search

Establishing Oscillation with Atmospheric Neutrinos

The Super-Kamiokande Experiment provided evidence of neutrino oscillation by looking at the asymmetry of upward and downward traveling atmospheric neutrinos. Atmospheric neutrinos have their origin in cosmic rays. When cosmic rays interact with matter in the atmosphere they create hadronic showers. One of the shower products can be a pion. Pions can decay into muons and muons can decay into electrons in the following manner.

$$\pi^+ \rightarrow \mu^+ + \nu_u \qquad \mu^+ \rightarrow e^+ + \nu_e + \bar{\nu}_\mu$$
$$\pi^- \rightarrow \mu^- + \bar{\nu}_u \qquad \mu^- \rightarrow e^- + \bar{\nu}_e + \nu_\mu$$

If all pions decay through the above channels the resulting ratio of neutrino flavors $\nu_\mu / \nu_e = 2$. In reality cosmic showers are more complicated but they have been modeled with Monte Carlo. After the hadronic shower, all of the charged components interact with the earth and are stopped. Only the neutrinos propagate though the earth and into the detector. It is interesting to note that the entire earth essentially provides no shielding from the flux of neutrino. Even with 13,000 km of iron (assuming the whole earth is iron) <1 in 10^8 neutrinos would interact. Once reaching the detector volume the neutrino/anti-neutrino can interact through a charged current interaction resulting in either an electron/positron or a muon/anti-muon.

$$\nu_\mu + n \rightarrow p + \mu^- \qquad \nu_e + n \rightarrow p + e^-$$
$$\bar{\nu}_u + p \rightarrow n + \mu^+ \qquad \bar{\nu}_e + p \rightarrow n + e^+$$

The Super-Kamiokande experiment was able to distinguish electrons from muons and thus aimed to evaluate the ratio for neutrinos traveling up and compare it for neutrinos traveling down. Assuming an isotropic flux of cosmic rays the ratio should be ~ $\nu_\mu / \nu_e = 2$. If however neutrinos were oscillating the ratio would be changed due to their flavor oscillation as they traveled through the earth. In the two flavor oscillation model the amount of disappearance of the electron flavored neutrino depends upon the L/E of the neutrino. L is given from the position of the cosmic ray shower and can be anywhere from 15 km for downward going neutrinos and 13000 km for upward going neutrinos that had to pass all the way through the earth. The Energy (E) of the neutrino was measured by the detector. For neutrinos with large L/E the oscillations would have an impact whereas for small L/E the oscillations would be small.

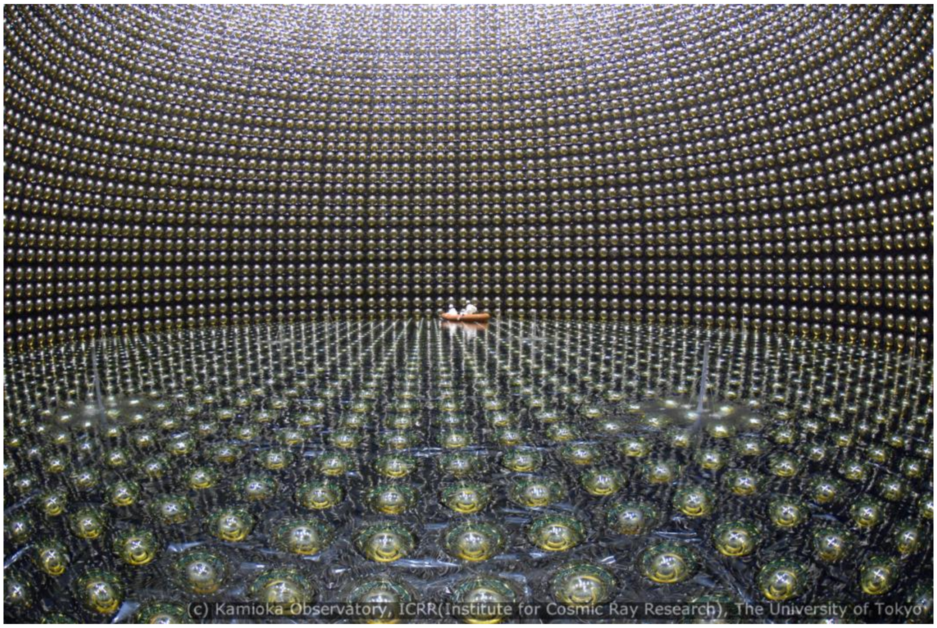

Figure 11: Some of the 11,000 PMTs visible inside the Super-Kamiokande Detector

The Super-Kamiokande Detector is located at the Kamioka mine in Japan at a depth of 2700 m.w.e. It is a water Cherekov detector with the main detector volume instrumented with 11,000 PMTs. It is surrounded by a 2 m active water Cherenkov Veto. The outer volume ensures that events are coming from within the main volume and not from cosmic muons. Flavor identification is possible because muons and electrons give different patterned light cones. Since electrons are much lighter they can scatter many times and result in a light cone that is wider than the light cone of a muon. Furthermore, the light cones are used to define the direction of the incoming neutrino and the total amount of light is related to the energy of the neutrino. Using these techniques they report an up-down asymmetry of : $0.52^{+0.07}_{-0.06(stat)}$ ±0.01(sys) for μ-like events [10]. For e-like events the asymmetry was consistent with no oscillation. This result can be interpreted within the frame work of neutrino flavor oscillation to mean that because of larger L/E of the muon neutrinos coming up through the earth, they have oscillated into tau neutrinos and are not detected. Since neutrino oscillations depend on L/E (which is measured), a mixing angle and Δm^2, the data can be fit to derive the parameters. Within this framework a maximum mixing angle and a Δm^2 between 5×10^{-4} and 6×10^{-3} eV^2 shows good agreement between data and prediction (Figure 12). This measurement provides further evidence of neutrino oscillations occurring not only in e flavor as with the solar experiment but also in μ flavor.

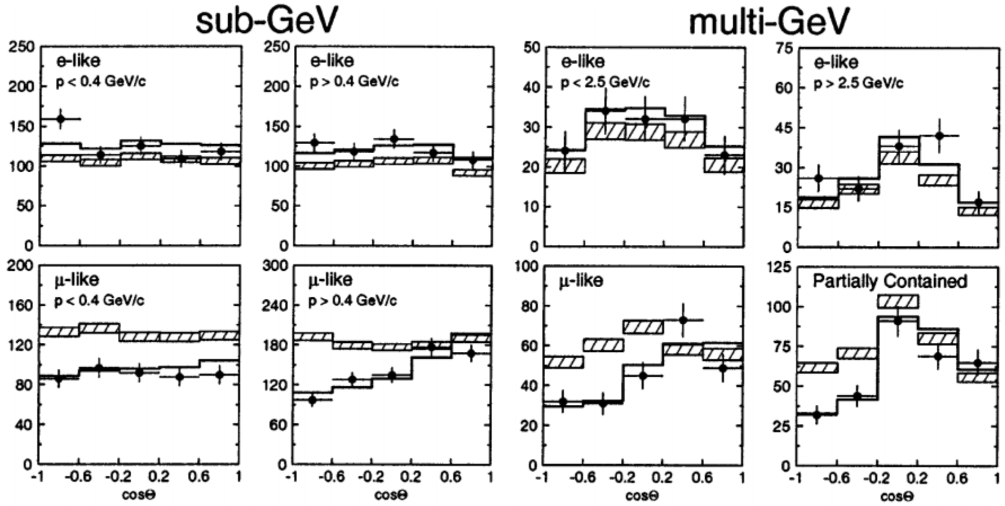

Figure 12: Super-Kamiokande data. Hatched data is assuming no oscillation and solid line includes oscillation with the best fit parameters.

Establishing Oscillation with Accelerators

While results from both solar neutrinos and atmospheric neutrinos agree well with neutrino oscillations, both experiments rely on complex models to predict the un-oscillated flux from a natural source. These sources (the sun and cosmic rays) have positive attributes in that they are free and abundant, but the drawback toward using them for neutrino oscillation is that they cannot be controlled. In the K2K experiment both the neutrino source and the neutrino detector were controlled by man.

The basic design of the K2K experiment was to have a neutrinos created by a particle accelerator travel toward a near detector to measure the initial flux of neutrinos and then to let the neutrinos travel through the earth, oscillate and then measure them again with a large far detector[11]. The Super-Kamiokande detector was chosen as the far detector since it had already proven its ability to detect ν_e and ν_μ from cosmic ray showers. The KEK accelerator in Japan was used to produce the neutrinos. It is located 250 km from the Kamiokande Mine. A smaller version of the Super-Kamiokande detector was installed as a near detector just 300 m from the neutrino production target.

The neutrino beam was provided by an accelerator with a well-known bunch structure (Figure 13). This information was propagated to the far detector and used to define a selection window. Additional quality cuts were applied in the far detector to obtain the final data set. A total of 158 events were observed in the far detector. The best fit value for both Δm_{23}^2 and Θ_{23} were obtained by using knowledge of the overall flux from the near detector and fitting the energy spectrum (Figure 14) from the far detector.

The final result of the K2K experiment put strong constraints on the Δm_{23}^2 and the mixing parameter Θ_{23}. The method of comparing a near and far detector would be used in future searches for the remaining mixing parameters.

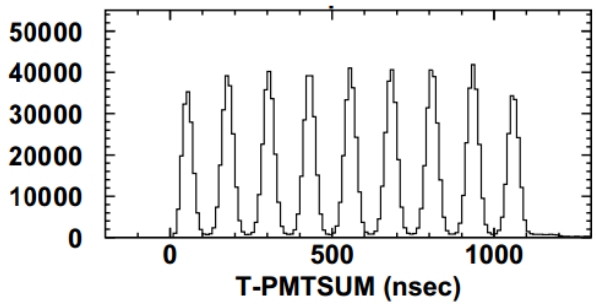

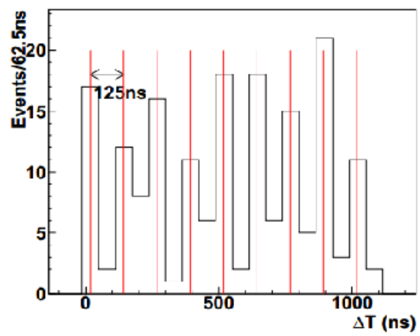

Figure 13: Time structure of events in the near and far detector show well known beam structure.

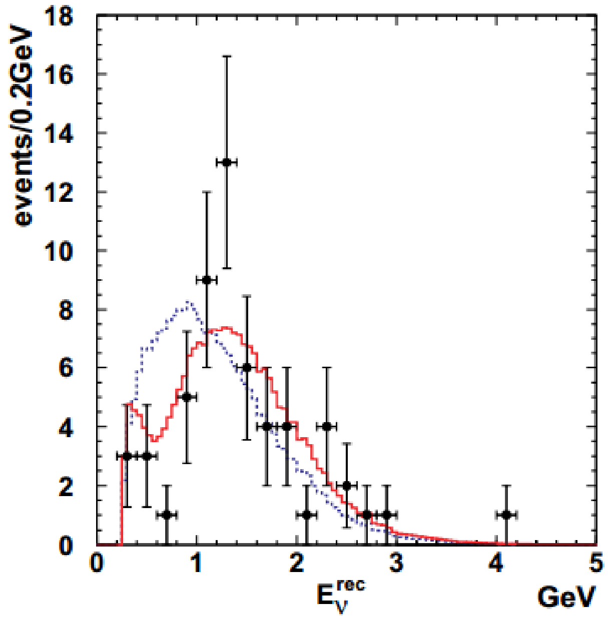

Figure 14: E_ν distribution for μ-like events in the Super-K detector. Blue line is the un-oscillated prediction, and the red line is the oscillated predictions.

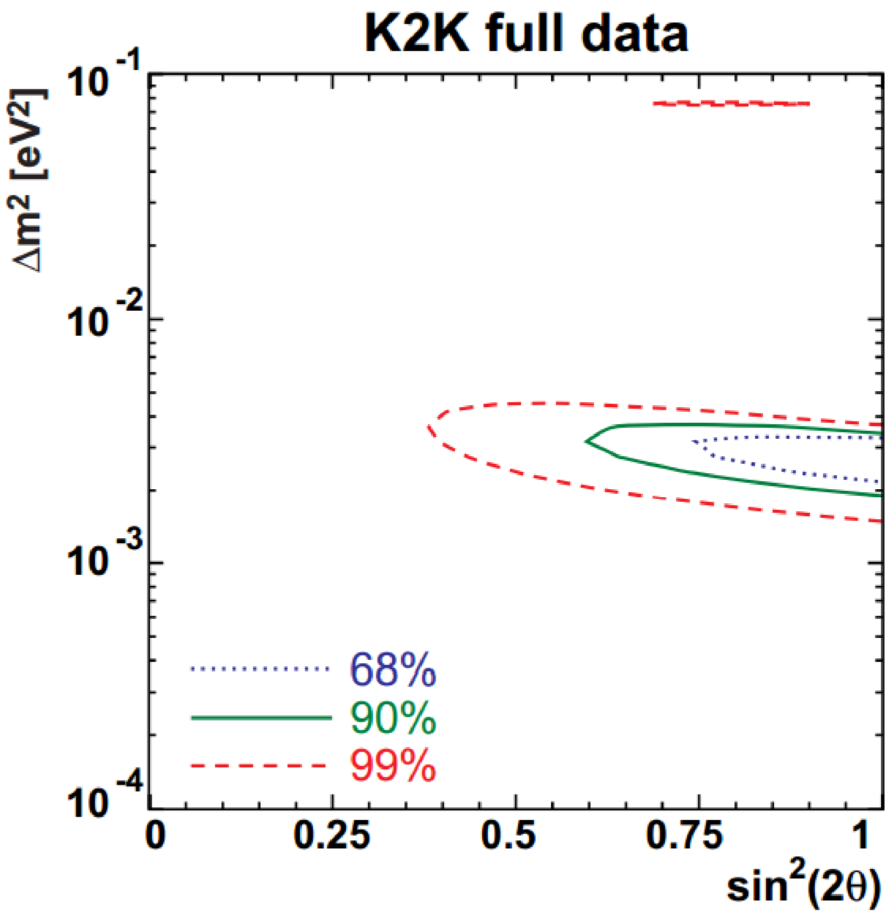

Figure 15: Fit Parameters of the K2K experiment.

Establishing Oscillation with Reactor

The KamLAND detector was the first to measure disappearance of reactor-based anti-neutrinos at large distances [12]. This confirmed the hypothesis of neutrino mixing which was first proposed to resolve the solar neutrino anomaly. Where previous experiments made a direct measurement of the neutrinos coming from the sun, KamLAND measured anti-neutrinos created in nuclear reactors. In the Standard Model, matter and anti-matter should behave symmetrically. By looking for oscillations from both anti-neutrino and neutrinos you can probe matter-antimatter asymmetries which would be evidence of physics beyond the standard model. Since the KamLAND result is in good agreement with previous solar neutrino experiments no matter-antimatter asymmetries have been found.

The KamLAND detector is located in the Kamiokande mine. With an overburden of ~2700 m.w.e. the detector observes a muon rate of only 0.34 Hz. The main detector volume is composed of liquid scintillator and is contained in a nylon balloon with a diameter of 13 meters (Figure 16). Surrounding the balloon is the containment vessel, a sphere 18 m across which holds 1879 photo multiplier tubes (PMTs). The space between the containment vessel and the balloon is filled with non-scintillating oil and acts as a passive shield from radioactive decays in the containment vessel and PMTs. The PMTs are comprised of 1325 new 17 inch tubes and 554 older 50 cm tubes which were reused from the Kamiokande experiment. Outside of the containment vessel is the outer detector which contains water and acts as an active veto from both muons and muon products such as fast neutrons that can be created as muons pass through the rock outside of the detector. The total trigger rate for the KamLAND detector is ~30 Hz.

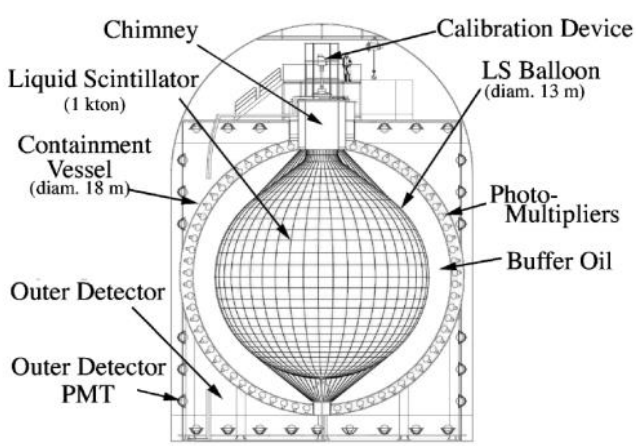

Figure 16: Schematic of the KamLAND Detector

The anti-neutrino sources for the KamLAND detector were the 55 nuclear reactors in Japan. Reactors in South Korea also contributed to the flux of anti-neutrinos, but their contribution was <3% of the total. The total flux of the rest of the world's reactors is <1%. KamLAND was the first to detect geo-neutrinos [13], which are neutrinos created inside the earth from the decay chains of Uranium and Thorium. These neutrinos contribute only at energies < 3.3 MeV and so they can be effectively omitted from oscillation analysis. Their measurement has implications for Geoscience and KamLAND was able to put upper limits on the amount of heat in the core that is generated by radioactive decays.

The mechanism for detection in KamLAND was inverse beta decay (IBD).

Equation 4: Inverse Beta Decay

$$\bar{\nu} + p \rightarrow e^{+} + N$$

This is the same mechanism for first neutrino detectors. In the Savannah River Experiment the liquid scintillator was doped with cadmium which provided fast capture of neutrons and a higher energy gamma ray (9 MeV). The KamLAND scintillator is not doped with cadmium, instead neutrons are captured on hydrogen. Capture on hydrogen occurs more than 99% of the time and results in a 2.2 MeV gamma. The neutron capture signal is preceded by the scintillation and subsequent annihilation of the positron. The anti-neutrino energy is required to provide the difference in rest mass between the initial proton and final neutron and positron. The detection threshold of an anti-neutrino can be simply calculated from the following equation:

$$m_{\nu} = m_{n} + m_{e^{+}} - m_{p} = 1.804\ MeV$$

An anti-neutrino with 1.804 MeV of energy would result in a positron at rest. When the positron annihilates with an electron two 0.511 MeV gammas are produced. Therefore the observed energy resulting from a 1.804 MeV anti-neutrinos is 1.022 MeV. In this way the neutrino energy is calculated as the observed energy +0.782 MeV. In addition, the energy observed in the PMTs is related to the vertex of the initial interaction. The vertex dependence of the energy arises from the geometry of the detector and from optical properties of the scintillator. Scintillator exhibits more light attenuation for large distances so that if the vertex is close to the top of the detector volume some of the light will be attenuated before it reaches the bottom PMTs. Similarly, the geometry of the detector influences the observed light because PMTs that are closer to the vertex will collect more light because of their larger solid angle. In the KamLAND detector the interaction vertex is calculated using PMT timing information. The vertex reconstruction procedure is accurate to ~25 cm and has been verified using calibration sources with known positions.

The KamLAND detector measured fewer neutrinos that what was predicted. The ratio of observed/ predicted was 0.611±0.085(stat) ±0.041(syst) (Figure 17). This result is consistent with the mixing angle required to explain solar experiments. The measured shape of the anti-neutrino spectrum also matched the result expected with a neutrino oscillation(Figure 18).

In an updated analysis with longer running time, KamLAND presented a measurement of the mixing angle $\tan^2\theta_{13}=0.56^{+0.1}_{-0.06}(\mathrm{stat})\ ^{+0.01}_{-0.07}(\mathrm{sys})$. With the increase in statistics they rule out alternative theoretical explanations of the solar neutrino problem and show that neutrinos oscillate with a large mixing angle (Figure 19).

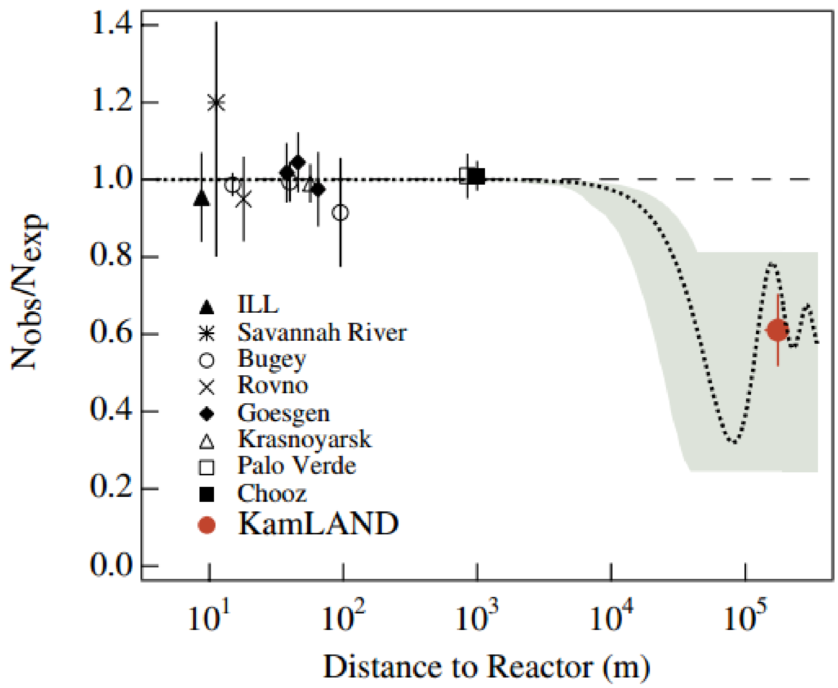

Figure 17: Ratio of observed to expected anti-neutrinos for reactor based neutrino detectors. Shaded region is the 95% CL of the Large Mixing Angle Hypothesis.

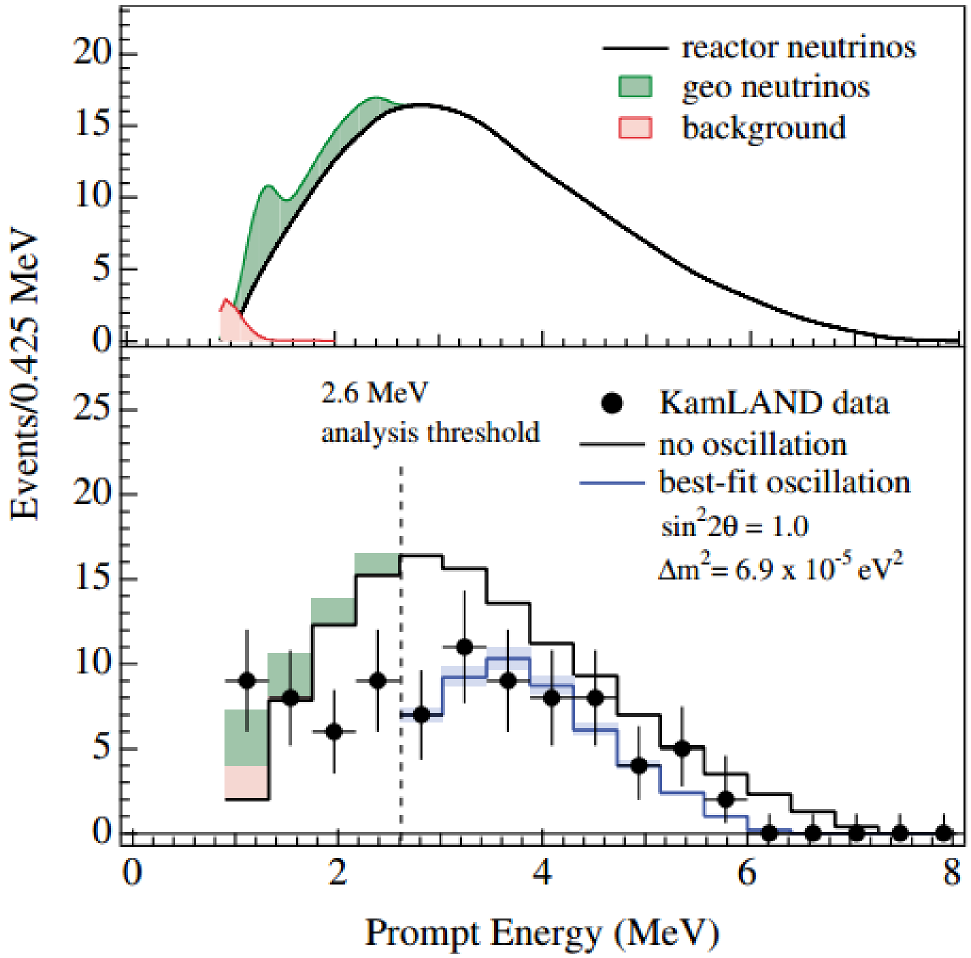

Figure 18: Neutrino oscillation analysis result of KamLAND. Dotted line at 2.6 MeV is the threshold for this analysis in order to neglect contributions from geo-neutrinos.

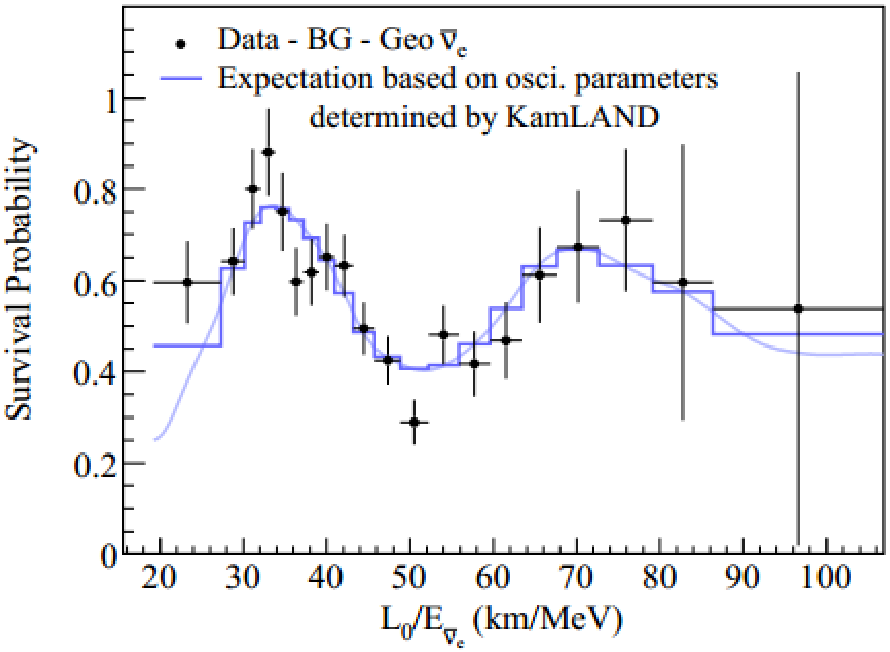

Figure 19: L_0 is the flux weighted average distance from the reactor. Strength of mixing angle Θ_{12} is manifest as the depth of the valley. The frequency is determined by Δm_{12}.

Mixing angle θ_{13}

By the early 2000's neutrino oscillations were firmly established. Mixing angles θ_{122} and θ_{23} were measured and were shown to be large. At this time there was an effort to make a first measurement of mixing angle θ_{13}. The experiments of CHOOZ[14] and Palo Verde[15] both published results that placed upper limits on the size of θ_{13}. No experiment at this time had observed a positive signal for mixing angle θ_{13} and many people speculated that it was very small. Both experiments relied on a neutrino detector ~1km from multiple nuclear reactors. Since neither experiment observed oscillations another set of experiments were designed to improve the sensitivity to observe θ_{13}.

Three experiments were started with the same goal of measuring short baseline neutrino oscillations from nuclear reactors. The three experiments were RENO (South Korea), Daya Bay (China), and Double Chooz (France). Each experiment is very similar in design in that they consist of a Near and Far Detector with excellent Energy Reconstruction. The purpose of the Near Detector is to measure an un-oscillated neutrino flux, while the far detector should measure the oscillated neutrino flux. Both total rate and shape information can be used to look for small amplitude oscillations.

Double Chooz was the first experiment to publish a positive signal for mixing angle θ_{13} in 2011 and did so with only the far detector running [16]. Daya Bay[17] and RENO [18] both confirmed the result in 2012 with both far and near detectors. To improve sensitivity to small θ_{13} angles the Double Chooz experiment will need to have a near detector. It is toward this end that I have contributed to the Double Chooz Collaboration.

Chapter IV: The Double Chooz Experiment

The Double Chooz experiment consists of two nearly identical detectors: one near to the nuclear reactors, to measure the un-oscillated flux, and one far, to measure the oscillated flux. The distances from each detector to the reactor cores are given in Table 1. Figure 20 shows the general layout of the reactor site in Chooz, France. The far detector began taking data in April 2011 and the Near Detector began taking data in January 2015.

Detector Design

Overview

The Double Chooz detectors consist of four separate volumes (Figure 21). The center Target volume is made from transparent acrylic and holds Gd doped liquid scintillator. The Target contains 6.8×10^{29} free protons that serve as the interaction target for anti-neutrinos generated inside the nuclear reactor cores. The Gamma Catcher, also made from transparent acrylic, surrounds the target and holds un-doped liquid scintillator. The Gamma Catcher ensures that gammas emitted in the Target travel through a sufficient amount of scintillator in order to deposit their full energy. Surrounding the Gamma Catcher is the Buffer. The Buffer is made of stainless steel and is filled with non-scintillating oil. Attached to the Buffer are 390 10" PMTs. The Buffer reduces the rate of radioactive decays in the detector by providing a region where decays in the PMT glass (mostly Potassium and Radium decay series) can lose energy before entering the scintillating region of the Gamma Catcher. The buffer has an additional requirement that it must be transparent to scintillation light so that light created in the target can reach the PMTs. Outside the Buffer is the Inner Veto. The Inner Veto is made from steel (optically separate from the inner detector), filled with scintillator, and holds 78 8-inch PMTs. The Inner Veto detects muons entering the Buffer and serves as an active veto. Above the detector pit is the Outer Veto. The Outer Veto is made from multiple layers of 25 mm segmented plastic scintillator and provides an addition muon tag and since it extends beyond the Inner Veto it can be used to study fast neutrons created by muons passing near the detector but not crossing the Inner Veto. The detectors are sealed and contain a nitrogen gas blanket to prevent oxygen from interacting with the scintillator. The detectors can be opened to deploy calibration sources. The sources enter the detector through a sealed glove box to prevent contamination of the detector with outside air. Above the Glove Box is an additional Outer Veto called the Upper Outer Veto. It is much smaller that the Outer Veto but has the advantage that it covers the small area in the very center of the detector. Vertical muons entering the Detector in this region cannot be seen by the Inner Veto because of optical separation caused from the filling pipes. If a muon travels through the Upper Outer Veto and the Outer Veto an accurate track can be reconstructed. Additionally, muon tracks can also be reconstructed from Inner Detector and Inner Veto PMT timing information.

Table 1: Distance from Reactor cores to Double Chooz Detectors

Detector	Distance to B1 (m)	Distance to B2(m)
Near	465	351
Far	1115	998

Figure 20: Aerial View of the Double Chooz site

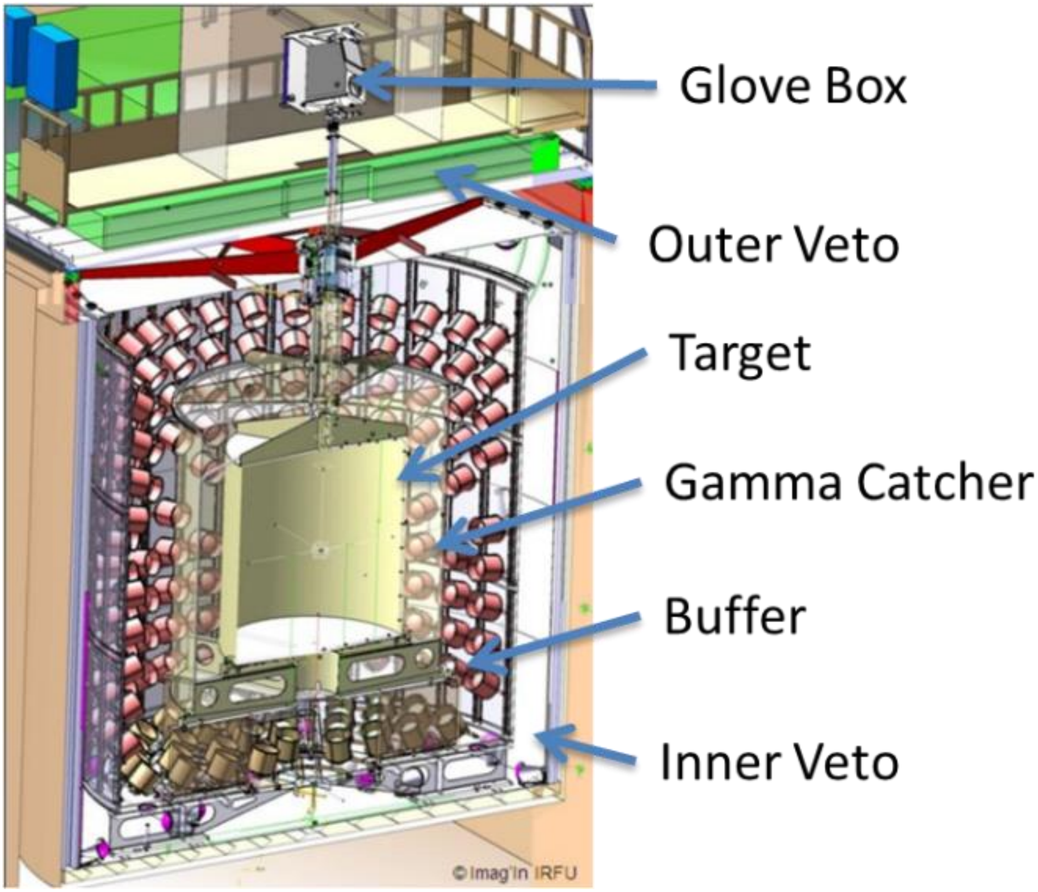

Figure 21: Schematic of the Double Chooz Far Detector

Scintillator

When a charged particle moves through scintillator the molecules of the scintillator absorb some of the energy of the particle and become electromagnetically excited. When the molecules de-excite they do so by emitting photons. The number and wavelength of these photons depend on the details of the scintillator. In Double Chooz we use a liquid hydrocarbon based scintillator. The requirements for the Double Chooz scintillator are: it should have an attenuation length >5 m in the blue-green region, it must be pure of radioactive isotopes, the different liquids should be of constant density, it must have excellent light yield, and it must be stable over the running period of the Double Chooz experiment (>5 years). The stability is a high priority because the previous Gd-doped scintillators in the first Chooz experiment have been shown to decrease attenuation length over the course of one year [14].

The scintillator in Double Chooz consists of PXE, PPO, bis-MSB, Gadolinium (Gd) in a beta-diketonate complex and n-dodecane. The n-dodecane serves as a base in which the PPO scintillator is dissolved. PPO and bis-MSB are both wavelength shifting fluors whose purpose is to transform the scintillation light into a frequency which is readily detected by the photomultiplier tubes. The light yield of the Target and the Gamma Catcher are matched to obtain a homogeneous detector response. The Gd-complex in the Target lowers the light yield so the Target requires more PXE to get the same light yield as the Gamma Catcher (Table 2).

Table 2: Composition of Scintillators in Double Chooz Target and Gamma Catcher

Scintillator	Composition
Target	80%$_{vol}$ n-dodecane 20%$_{vol}$ o-PXE 4.5g/l Gd-(thd)$_3$ (Gd(III)-tris-(2,2,6,6-tetramethyl-heptane-3,5-dionate)) 0.5%$_{wt.}$ Oxolane (tetrahydrofuran, THF) 7 g/l PPO (2,5-Diphenyloxazole) 20mg/l bis-MSB (4-bis-2(-Methylstyryl)benzene)
Gamma Catcher	66%$_{vol}$ Mineral oil (Shell Ondina 909) 30%$_{vol}$ n-dodecane 4%$_{vol}$ o-PXE (ortho-Phenylxylylethane) 2 g/l PPO (2,5-Diphenyloxazole) 20mg/l bis-MSB (4-bis-2(-Methylstyryl)benzene)

To ensure radio purity the liquid components were distilled. The n-dodecane used for Double Chooz is from the same plant that produced it for the KAMLAND detector, because its radio purity was already established. The PXE was used in the Borexino experiment and its contamination was known. The major contribution of potassium and uranium and thorium are from the fluors and Gd-complex. The Gd-complex initially had a potassium level of >100 ppm but since the Gd-complex has a high vapor pressure it was able to be purified using sublimation to a level of 1ppm. The Gd-complex and the PPO were tested using a gamma-spectroscopy (GE-MPI) located in a underground laboratory in Gran Sasso, Italy. The results of the radio-purity exceeded the need for the detector (Table 3,Table 4) [19].

The densities of the all liquids used in the Double Chooz must be within 1%. The Target and Gamma Catcher volumes are supported by acrylic vessels which could bend or break if there was a hydrostatic pressure between them. During filling the levels in each volume were held to within 1 cm to ensure that the acrylics were not strained.

The attenuation length of the Gamma Catcher fulfills the requirement that in the blue-green region the attenuation length is greater than 5 m (Figure 22). This ensures that there is minimal loss of photons from the target to the PMTs. The light yield of the scintillator was measured to be 40% the light yield of anthracene. This light yield results in ~180 PE/MeV and is very uniform throughout the Target. It is important that the scintillation time is short so that efficient triggers can be activated and the total charge can be within a 256 ns integration window. The Double Chooz liquids easily fulfill this requirement (Figure 23).

Table 3: Gamma Spectroscopy results for Gd-Complex powder.

Isotope	Concentration in Gd-Complex	Concentration in Target
^{nat}K	0.43 ppm	2.4 ppb
^{235}U	<1 ppb	<6 ppt
^{238}U (^{226}Ra)	<0.05 ppb	<0.3 ppt
^{228}Th	<0.2 ppb	<1.1 ppt

Table 4: Radio purity results for PPO powder. Neutron Activation Analysis (NAA) and Atomic Activation Spectroscopy (AAS) are shown for Potassium in addition to the Gamma Spectroscopy (GeMPI).

Isotope	method	Concentration in PPO
^{nat}K	NAA	0.35±0.16 ppm
^{nat}K	AAS	0.25±0.04 ppm
^{nat}K	GeMPI	0.5±0.1 ppm
^{235}U	GeMPI	<0.72 ppb
^{238}U (^{226}Ra)	GeMPI	<0.05 ppb
^{228}Th	GeMPI	<0.26 ppb

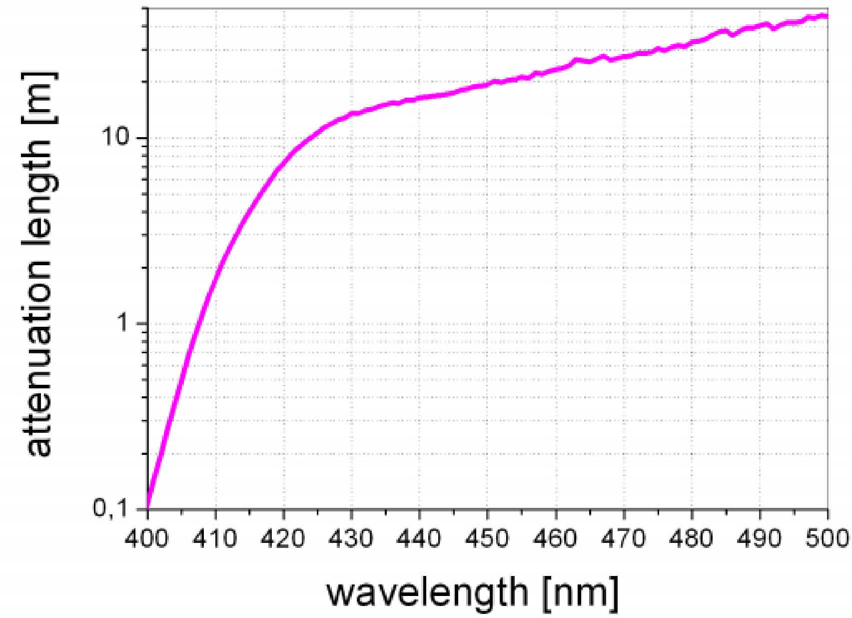

Figure 22: Attenuation Length of Liquid in the Gamma Catcher.

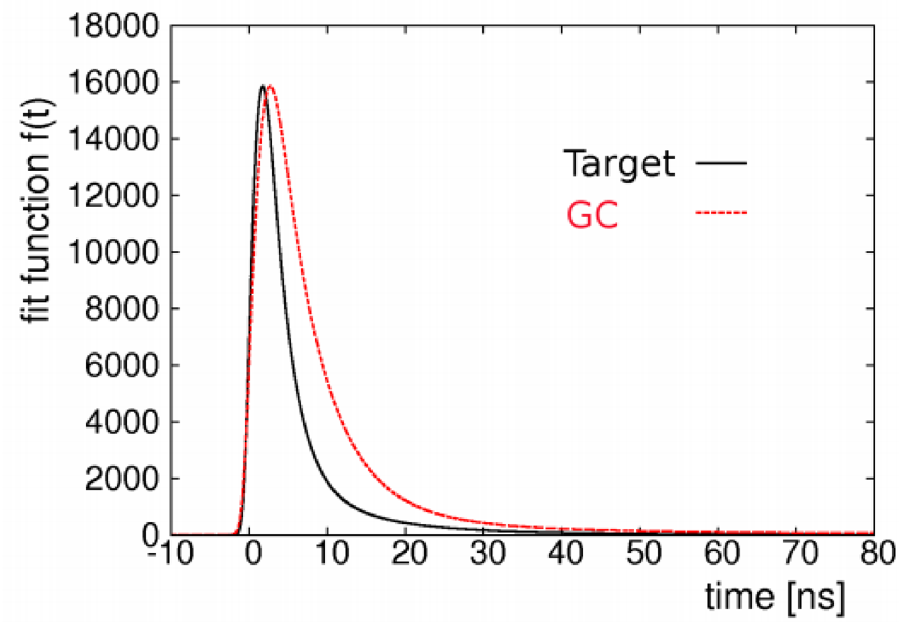

Figure 23: Scintillation photon emission time distribution for beta excitation in the Gamma Catcher (GC) and neutrino target(Target).

__Inner Detector Photomultiplier Tubes__

The Inner Detector photomultiplier tubes (PMTs) detect light created by particle interactions with the scintillator. They are the only instruments that detect neutrino signals in the Double Chooz experiment. The basic design of a PMT consists of photo cathode an electric field to guide the electron and dynodes. The photo cathode creates an electron when a photon strikes its surface. The electric field accelerates the electron onto a series of dynodes which act as electron multipliers. For the R7801 a single photo-electron is converted into 10^7 electrons after passing through all the dynodes. The PMT converts a single photon into in a measureable electric current. The typical timing of the PMT response is slower for larger PMTs (Figure 25) but cost constraints demand using fewer, larger PMTs to obtain a good photo-coverage.

There are 390 10 –inch Hamamatsu R7801 PMTs installed on the Buffer Wall (Figure 24). They provide 13.5% coverage. The Hamamatsu R7801 was chosen because of good Single Photo-Electron resolution (Figure 27) and it was produced using low radioactive glass to reduce the counting rate within the detector. The Double Chooz scintillator was designed to produce light in the region of the highest sensitivity of the PMT (Figure 26).

After production the PMTs were transported to Germany and Japan for characterization test. Gain, dark rate, transit time, transit time spread and quantum efficiency were tested for each PMT [20]. As a result of these preliminary tests 8 PMTs were withheld from installation. One PMT did not give a signal, one lost its vacuum after initial test and six had unstable or high dark rates.

Figure 24: (Left) Hamamatsu R7801 PMT with acrylic mounting and Magnetic shield. A portion of the magnetic shield is removed to make the picture. (Right) Bare Detector PMT.

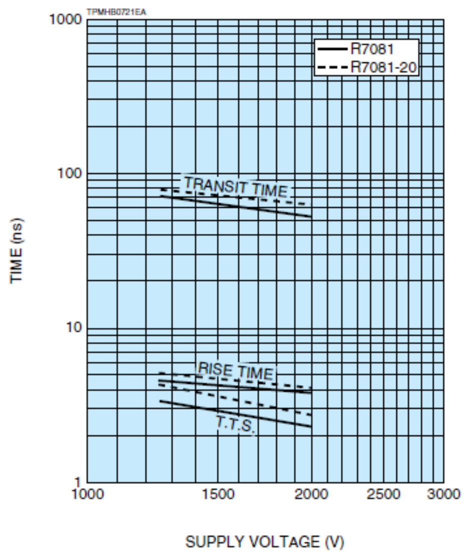

Figure 25: Hamamatsu defined time response for Detector PMTs.

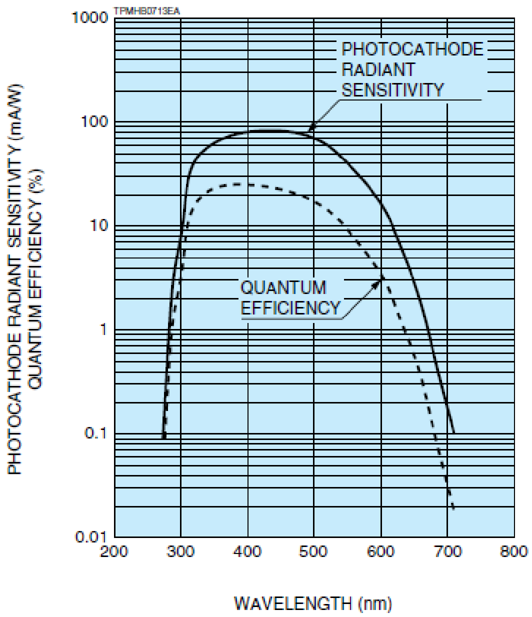

Figure 26: Detector PMT efficiency from Hamamatsu

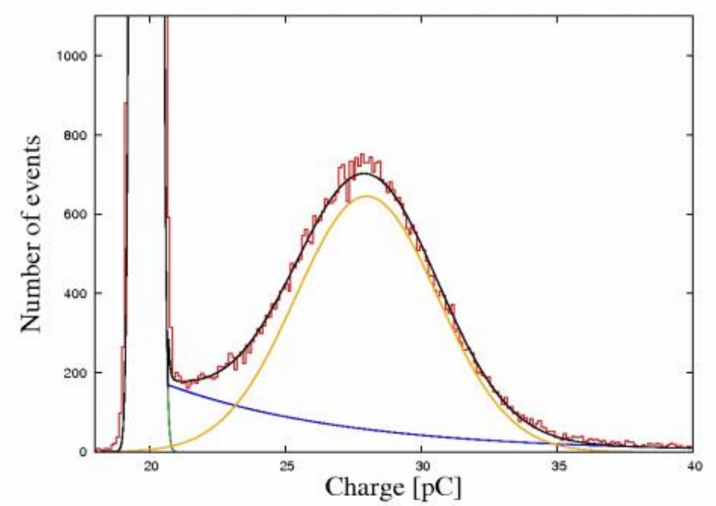

Figure 27: Single Photo-electron Spectrum data shown in red with the fit function in black. The fit is two Gaussians (green and yellow) and a decaying exponential (blue).

A PMT SPE response depends on external magnetic field. Independent tests on the R7801 confirmed the SPE dependence on Earth's magnetic field, and additionally measured the dependence of the spe response on the location of the photon on the PMT face [21]. To ensure a PMT response independent of Earth's magnetic field, a mu metal cylinder was placed around every PMT to shield it from external magnetic fields. With the specific design outlined in [22] the SPE response in the presence of an earth like magnetic field is reduced by 5%. With no shielding the SPE response was reduced by 60% for Earth-like Magnetic fields (Figure 28). The magnetic field shield extends beyond the face of the PMT and causes a decreased in light collection. When the shield extends 5.5 cm above the PMT face the light collection is reduced by 14%. This was chosen as the final design.

After delivery of the PMTs to the detector site in Chooz France, further onsite tests were conducted by the UT group. More details on this can be found in "Chapter V: PMT System Installation and Testing."

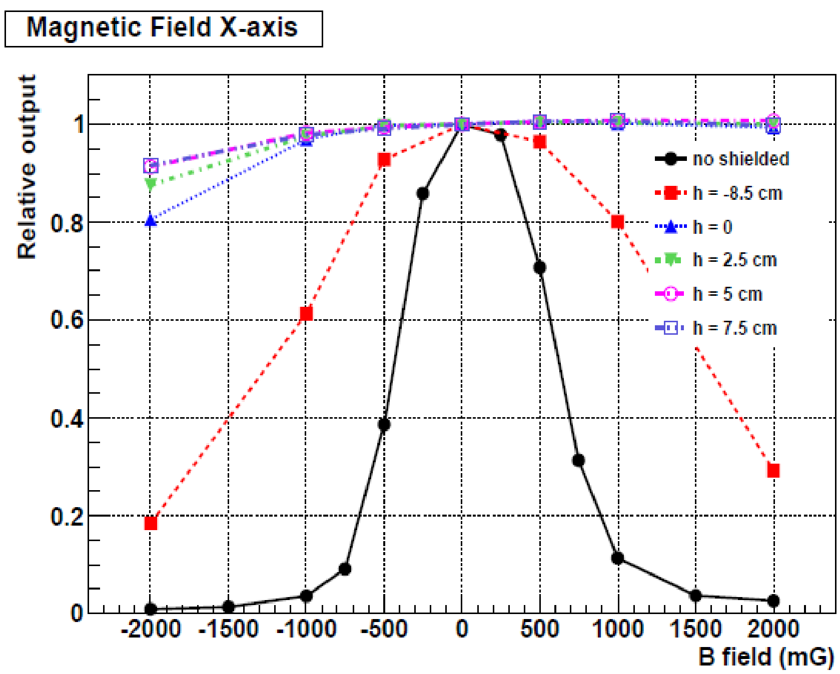

Figure 28: Output of PMT/(Output with no B field) for various mu-metal positions and external magnetic fields.

Inner Veto PMTs

There are 78 R1408 8-inch diameter PMT made by Hamamatsu in the Inner Veto. These PMTs provide very little solid angle coverage but were arranged in such a way so that they see light in all corners of the IV vessel. The Inner Veto Vessel has highly reflective walls so that the maximum number of PMTs will see light in the event of a muon. More information on the Inner Veto PMTs can be found in the section “IV PMT Tests”.

Trigger System

The Double Chooz Detector can be triggered by the Inner Veto or the Inner Detector. The PMTs of the ID are divided into two groups designated “A” and “B”. Each group consists of 195 PMTs uniformly distributed throughout the detector. Groups A, B and IV PMTs are summed and if any group sum is above threshold the detector is triggered. Upon triggering a 256 ns window is open and the waveforms of both IV and ID are recorded by a 500 MHz flash ADC. Using the summed signals to trigger ensures that there are minimal contributions from dark rate signals that occur in individual PMTs. While the Dark Rate can be 1000s of Hz the signals will occur at random times so that the chance of having a trigger due to alignment of many random signals is small.

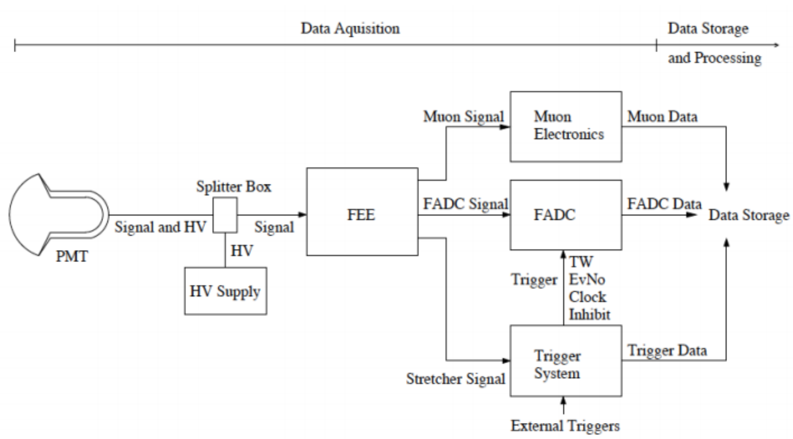

Figure 29 Schematic of the Double Chooz Electronics

Reconstruction Algorithms

Vertex reconstruction

Vertex reconstruction is done using charge and timing information from every PMT. The event reconstruction assumes that the event is created at a single point in the detector and predicts the position and time of the event using a maximum likelihood algorithm. The algorithm has been tuned using laser calibration data and source calibrations. To check the vertex reconstruction quality we can compare the reconstruction to a known source location. With a ^{60}Co source in the center of the detector the uncertainty of the vertex reconstruction is 21 cm (Figure 30).

The vertex reconstruction has some power to discriminate against non-point-like events. Fast Neutrons can undergo multiple scatters in the detector causing multiple sources of light and muons that stop near the edge of the scintillating volume will leave a track of scintillation rather that a single point. In both these cases the reconstruction algorithm will return a worse likelihood than for a point like event (Figure 31).

Energy Reconstruction

When a charged particle travels through scintillator in the detector it loses energy and creates scintillation light. The light propagates to the PMT face which causes a current proportional to the number of photoelectrons created on the PMT face. We observe the current of the PMT through a 8-bit flash ADC with 500 MHz sampling (Figure 32). To determine the total energy of the event we must first convert the measured charge to number of photoelectrons and second convert number of photoelectrons to the energy of the initial particle. To convert the measured charge to the number of photoelectrons you must know the gain of each PMT i.e. how much charge is created by one photoelectron. Gains of each PMT are calculated using the Inner Detector Light Injection System (IDLI). Dedicated runs are taken on a regular basis where LEDs illuminate the PMTs with light and the gain is determined by fitting the resulting spectrum. A second correction in the gain is applied due to quantization effects of the flash ADC which results in non-linear gains at low PE values (Figure 33) [23]. After the charge non-linearity is corrected the number of photoelectrons can be summed from every channel.

The next step in energy reconstruction is to convert the total number of photoelectrons to a MeV scale. Toward this end, a detector wise map is created to account for positional dependence of light collection efficiencies. The map is created by fitting the 2.223 MeV gamma peak resulting from a neutron capture on hydrogen. The neutrons that result from spallation muons are abundant and evenly distributed throughout the detector volume. This correction is fairly uniform in the detector’s center but can be as large as 5% in the corners of the Target and up to 15% in the corners of the Gamma Catcher.

Liquid scintillator has light non-linearity’s that are parametrized in terms of Birk’s coefficient. To determine the scintillator’s light non-linearity a Monte Carlo study was performed and compared to gamma calibration data. The value of Birk’s coefficient was chosen so that Data and Monte Carlo agreed (Figure 35).

Finally, the time dependence of the Energy reconstruction was checked using over the entire running period using muon induced spallation neutron captures on hydrogen (H) and Gadolinium (Gd) as well as the alpha decay of ^{212}Po. The energy reconstruction was stable in time to <2% over the almost two years of running for the Far Detector.

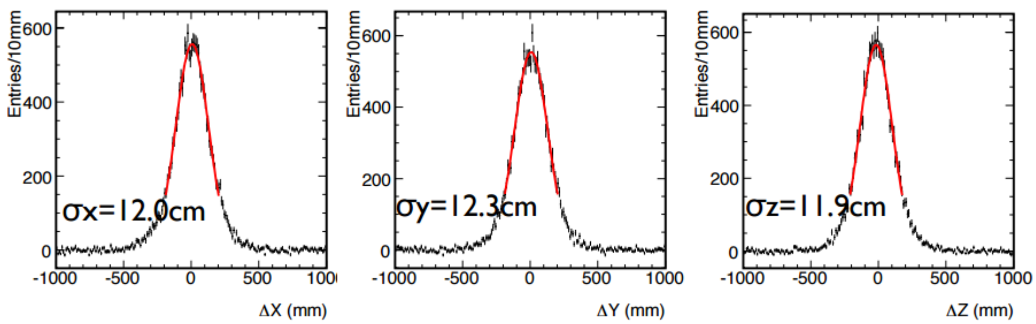

Figure 30: 60Co source in the center of the detector. Black does are back ground subtracted data and red line is a Gaussian fit.

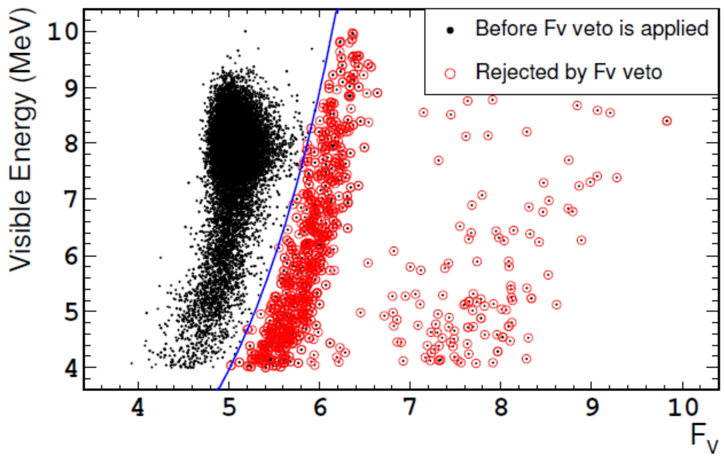

Figure 31: F_V = – ln(Likelihood function) Events to the left of blue line are point like i.e. n-Gd captures. Events to the right are not as point like i.e. Fast Neutron or Stopping muons

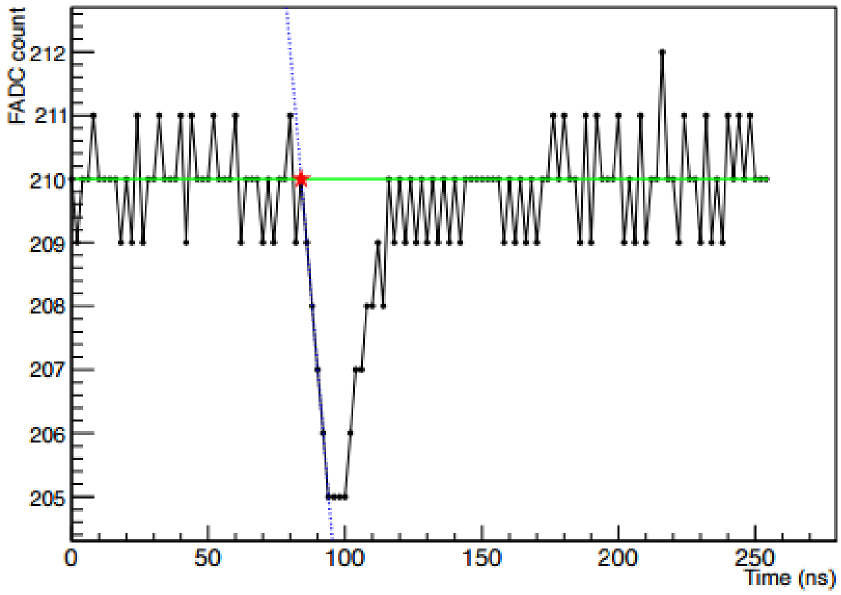

Figure 32: Typical pulse from the Flash ADC

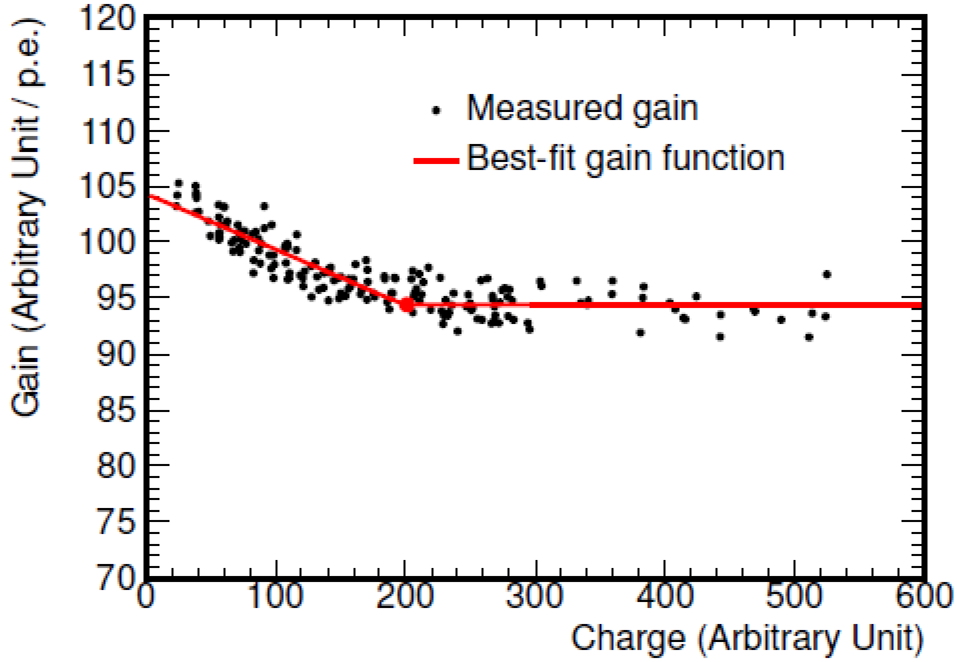

Figure 33: Charge non-linearity caused by quantization effects of the flash ADC.

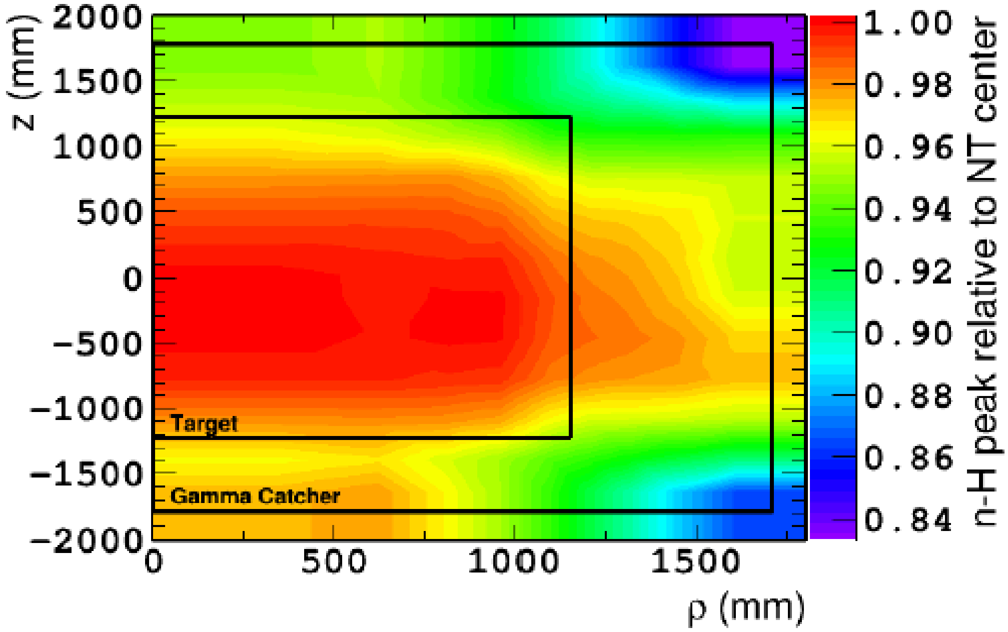

Figure 34: Uniformity Correction Map obtained from fitting the 2.223 MeV n-H peak from spallation Neutrons.

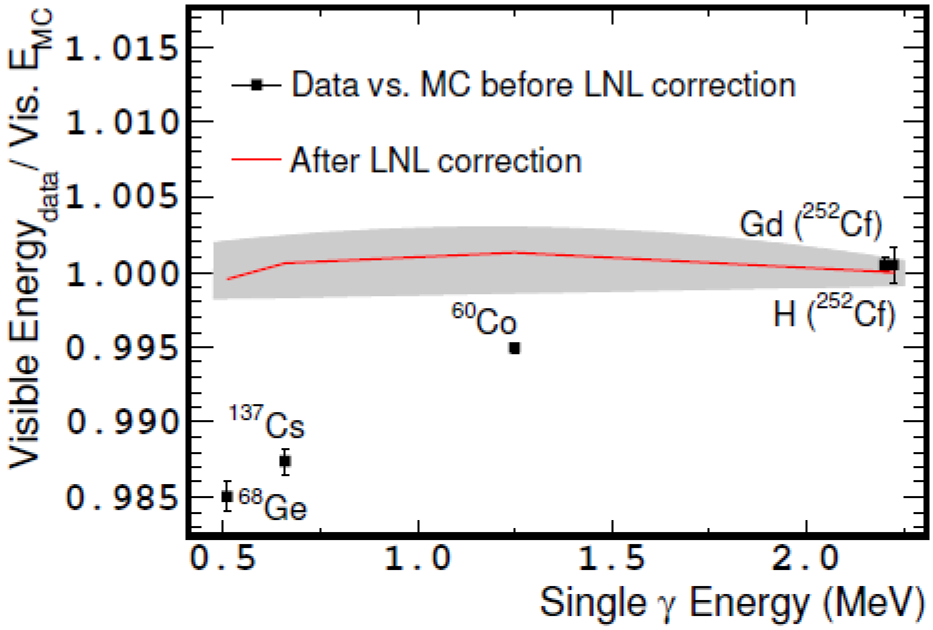

Figure 35: Effect of Light Non-Linearity (LNL) due to Birk's coefficient.

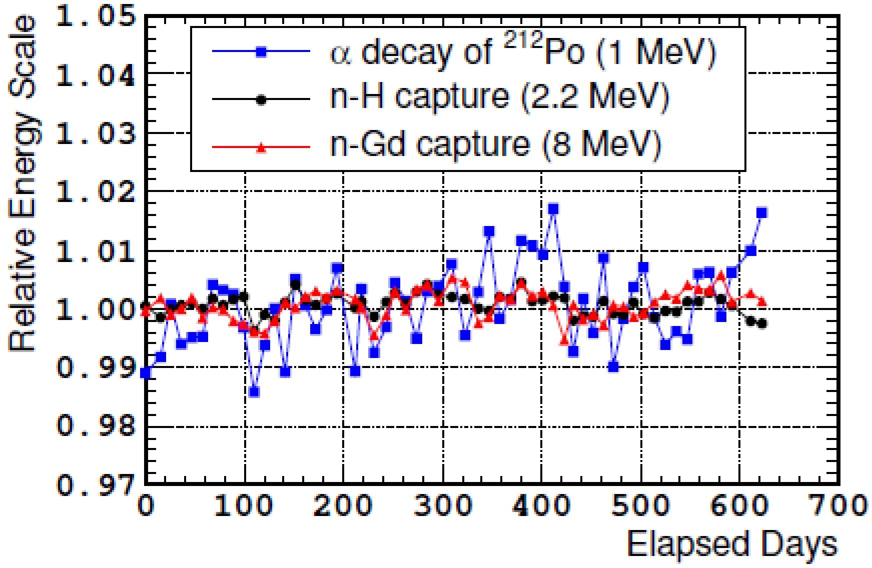

Figure 36: Time stability of the energy reconstruction for various sources.

Muon track reconstruction

Muon tracks can be reconstructed in the detector using timing information. When a muon passes through the central detector it creates both scintillation and Cherenkov light which then propagates to each PMT (Figure 38). Scintillation will be the dominant source of light for muons that pass through the GC or Target and Cherenkov radiation will dominate if the muon only passes through the buffer. The total event charge is used to classify the muon as one that is scintillation dominated or Cherenkov dominated. For both cases the theoretical start times of each PMT are calculated based on different muon track positions and a best fit is obtained. If a muon passes through the OV and Upper OV then an accurate track can be reconstructed solely based on OV information. Comparing the track reconstruction only using the main detector verse the track of OV yields an accuracy of Detector reconstruction of ~100 mm (Figure 37). When muons are Cherenkov dominated the resolution is about 3 times worse.

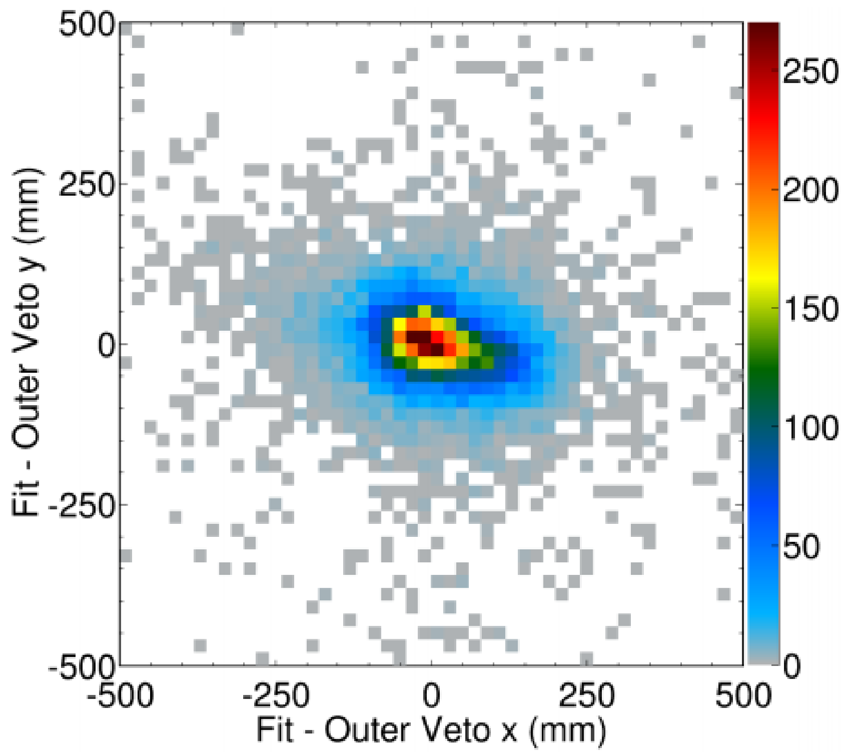

Figure 37: Resolution of Muon tracking compared to OV reconstructed tracks for scintillation dominated.

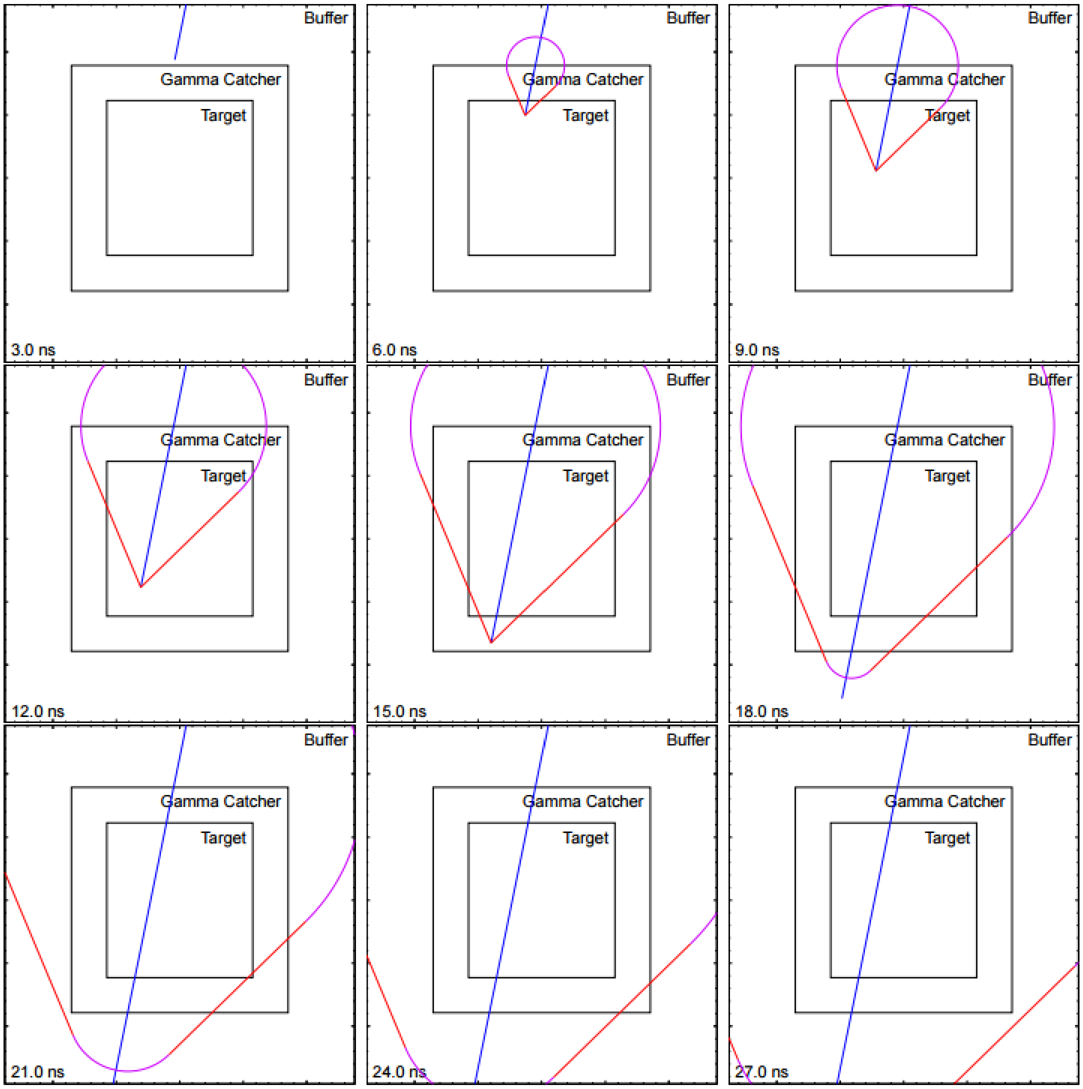

Figure 38: Red and Purple lines represent the wave front of scintillation photons created by a muon (blue line). The intersection of the wave front with the PMTs on the buffer wall define expected start times for each PMT for a given muon track.

Reactor anti-neutrino Flux Prediction

In the one detector phase of the Double Chooz experiment, the anti-neutrino flux from the reactor must be accurately modeled in order to provide an un-oscillated spectrum prediction. The un-oscillated prediction is then compared to the observation at the far detector to extract the θ_{13} mixing parameter. In the two detector phase of the experiment there is the possibility to use the near detector to measure the un-oscillated flux with the near detector and then compare the oscillated measurement at the far detector. Additionally, in the two detector phase, the Near Detector can be used to make an accurate measurement of the reactor flux and compared to the reactor model as a test of the model.

Predicting the anti-neutrino Flux

Anti-neutrinos are created when an atom undergoes beta decay. However, the driving mechanism of a nuclear reactor is not beta decay but fission. Atoms that are sufficiently large can release energy by undergoing fission (Figure 39). The four main fissionable atoms used in nuclear reactors are ^{235}U, ^{238}U, ^{241}Pu, and ^{240}Pu. On average when these atoms fission they release 200 MeV of Energy which is eventually used to generate electricity. Since the initial parent nuclei (^{235}U, ^{238}U, ^{241}Pu, and ^{240}Pu) are all neutron rich (neutron/proton > 1.5) the resulting daughter nuclei are also neutron rich. These neutron rich daughters undergo β^- decay until they reach stability. On average, there are six β^- decays for every fission. To first order, the total anti-neutrino rate is proportional to the power output of the reactor core. The Double Chooz reactor cores are monitored by the EDF (Electricity Company of France) and the thermal power is calculated every minute by temperature sensors within the primary water loop.

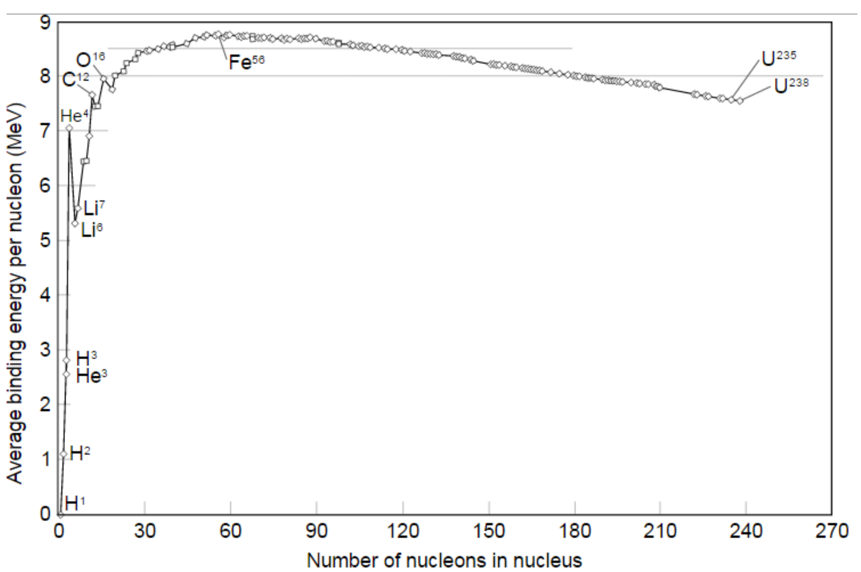

Figure 39: Binding Energy per Nucleon Curve.

For a precise measurement of the neutrino oscillation additional information about the shape of the anti-neutrino spectrum is also required. The anti-neutrino spectrum can be calculated from first principles via the Ab Initio Method. Inputs into this calculation include: the amount of ^{235}U, ^{238}U, ^{241}Pu, and ^{240}Pu in the core, the daughter nuclei that can be populated by each of these fissions, all Q-values and branching ratios of possible daughter decays, and the shape of the anti-neutrino spectrum of each decay. There are over 1000 daughter nuclei that are populated and over 6000 unique Beta decays that are involved in this calculation and ~6% have unknown Q values and branching fractions [24]. Generally, the unknown decays are the ones that are far from stability and therefore difficult to measure. These are also the decays with the highest Q values. The Spectrum shape is well understood for Fermi and Gamow-Teller Decays but ~25% of the resulting decays can be forbidden and therefore require additional shape corrections.

An alternative to the Ab Initio Method is the β Conversion Method. This relies on a series of measurements made at the ILL research reactor [27,28,29] in which a Target of ^{235}U, ^{238}U, ^{241}Pu, or ^{240}Pu was irradiated with thermal neutrons and a magnetic spectrometer was used to measure the energy of the electrons in the resulting β decays. This experiment provides the integrated sum of all decays and therefore is not affected by missing nuclear physics information. However, the ILL experiments measured the electron spectrum, but we would like to predict the anti-neutrino spectrum. β decays are described by three body relativistic kinematics. In the limit where one body is much more massive (as is the case since the nuclei is much more massive than the electron and anti-neutrino) the problem can be effectively reduced to a two body decay. In this limit the neutrino energy is completely determined by measuring the electron energy. However this picture is complicated by the following factors: when exiting the nuclei the electron will interact via the electromagnetic force but the neutrino will not, in forbidden decays the nucleus is forced to carry away energy, and the weak interaction is not truly a point-like interaction. These effects have been taken into account in detail [25, 26] and the neutrino spectrum calculated to a final uncertainty of <2%.

Recent measurements by the RENO and Daya Bay near detectors show an excess of events in the region from 5-7 MeV. A recent update to the Ab Initio Method [24]has attempted to explain the deviation of the shape by considering the contribution from ^{235}U, which is the least well measured spectrum (Figure 40). The Double Chooz Near detector will be able provide precision data to this puzzle within a few years.

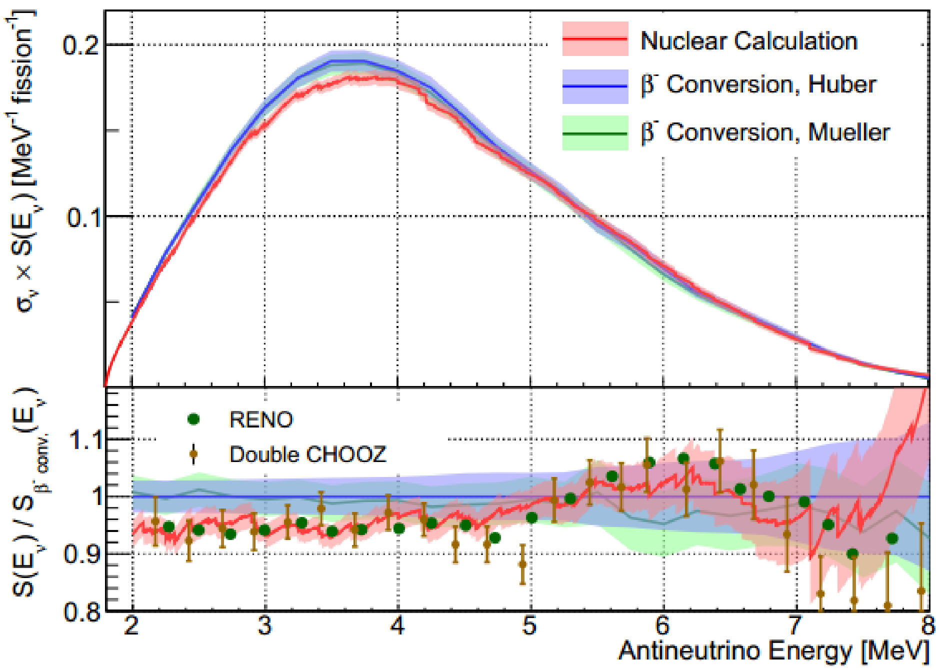

Figure 40: Ab Initio calculation for U-235 is shown in red. Green and Blue are calculated using the Beta Conversion Method. Data point show similar shaped to the Ab Initio Calculation

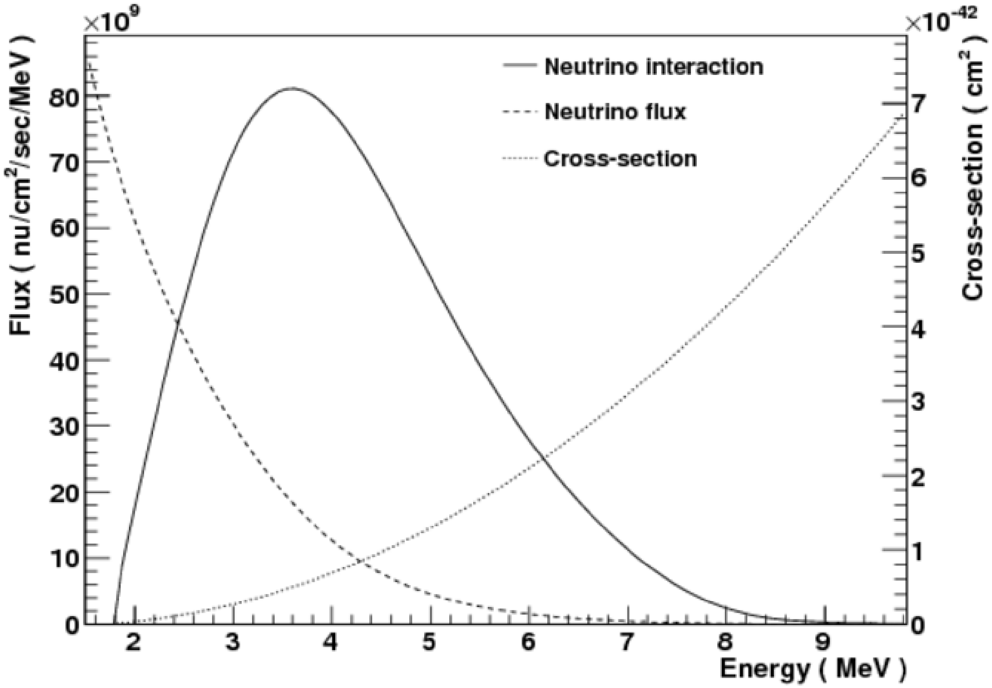

Figure 41: Neutrino flux and cross section are convoluted to obtain the expected detected spectrum.

Chapter V: PMT System Installation and Testing

Installation Contribution

The University of Tennessee was responsible for ensuring the quality of all the PMTs that were installed inside the Detector. To this end, a portable testing station was designed. The testing station consists of a black box, NIM and CAMAC electronics, an oscilloscope and a DAQ system. Initially, the testing station was transported to France for use in the construction of the far detector. Brandon White, a previous UT graduate student, completed these test for the Far detector. I have used the same testing system for the tests of the Near Detector.

IV PMT Tests

The Inner Veto PMTs were previously used in the IMB experiment which started running in 1986. After the IMB experiment was completed the PMTs were sent to The University of Tübingen in Germany for encapsulation. After encapsulation, I tested the PMTs in Tübingen to ensure that no damage was done during transportation and encapsulation. At this time a handful of PMTs were found to have reflections in their pulses caused by damaged internal resistors in the base. These PMT were repaired and retested.

My measurements serve as the baseline by which to compare with later tests. Most of the PMTs had known high voltage value corresponding to a gain of 10^7, but for a batch of 18 PMTs the nominal voltage was unknown. For the PMTs with unknown nominal voltage a voltage scan was completed and a nominal voltage was assigned. For the PMTs with existing nominal values I determined the gain. Following the initial test in Germany, the PMTs were shipped to France for installation in the detector. At this time, I repeated tests to ensure that no PMT was damaged during transportation. The results of the two tests (Figure 44) show that the PMTs have similar performance and no PMTs were damaged during transportation.

The IV PMTs have poor single-photoelectron (SPE) resolution (Figure 45). In order to obtain a gain measurement the PMTs were tested using a low efficiency LED. To test the LED efficiency a PMT with similar encapsulation, but better SPE response was used. We gate with the LED pulse and vary the pulse time of the LED in order to tune the SPE efficiencies (Figure 46). A LED efficiency of 20% was chosen so that higher order photon effects could be ignored and to minimize data acquisition time.

Figure 42: UT designed PMT testing Station consisting of a black box, oscilloscope, readout electronics and DAQ system.

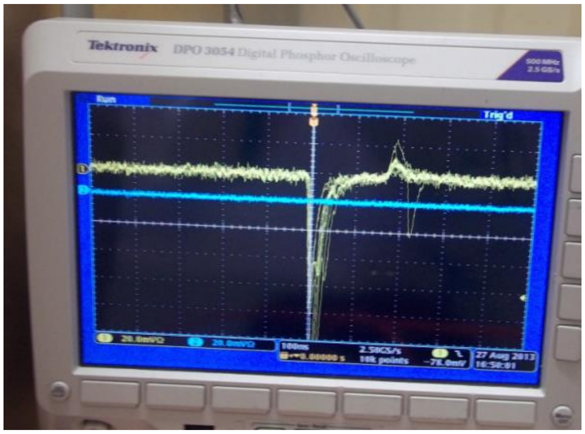

Figure 43: IV PMT pulse with reflection due to faulty base

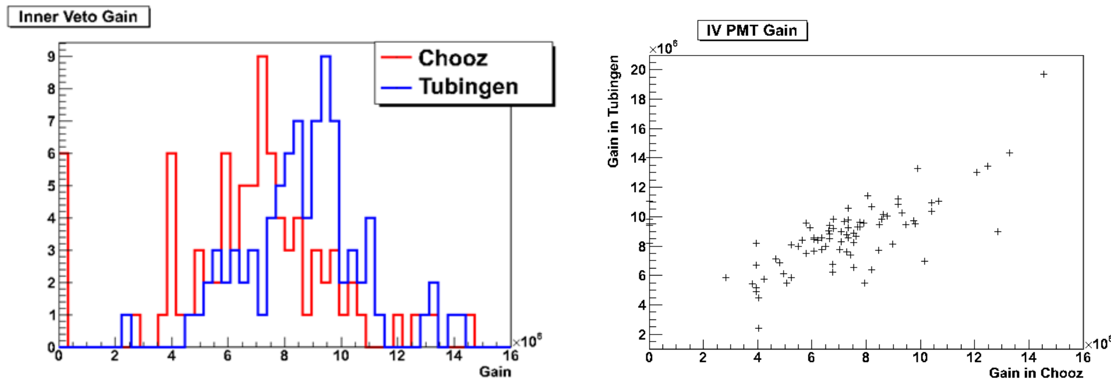

Figure 44: Gain of IV PMTs. Blue was measured in Tubingen and Red was measured in the Near Lab at Chooz.

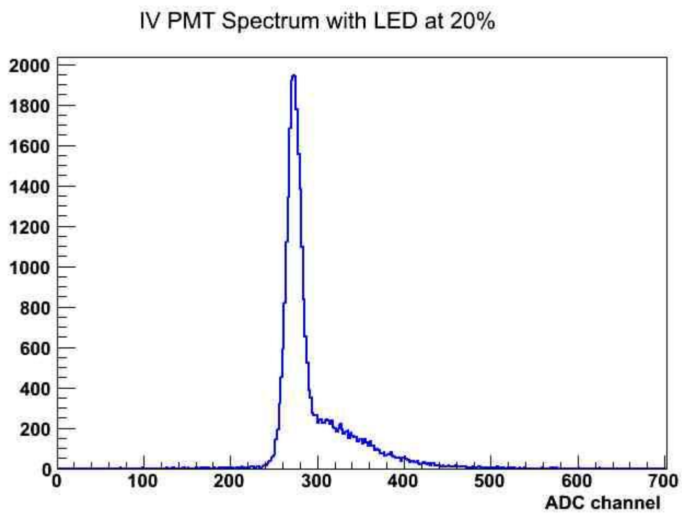

Figure 45: Example of IV PMT spectrum with pedestal and poor SPE resolution

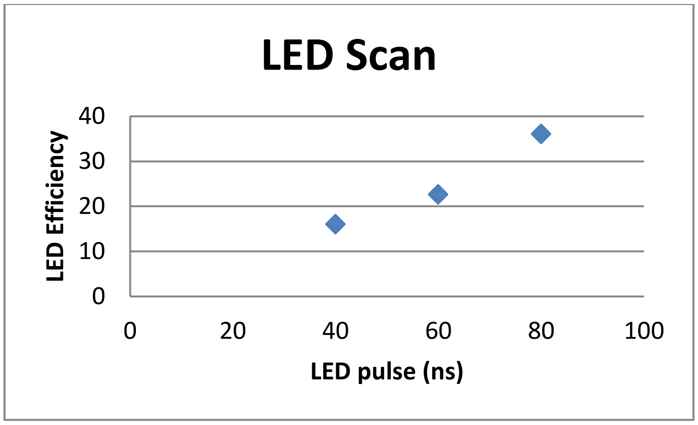

Figure 46: LED Efficiency Scan with PMT with similar encapsulation to IV PMT

Inner Detector PMT Tests

Detector PMTs

The Inner Detector consists of 390, R7081 10-inch PMTs made by Hamamatsu. These PMTs are essential to the Double Chooz experiment, because they are used inside the main detector volume and ultimately are used to reconstruct the energy and positions of neutrinos that interact with the Target. These are superior quality PMTs newly produced with low radioactivity glass specifically for use in Double Chooz . In contrast to the Inner Veto PMTs, the Detector PMTs have excellent SPE resolution (Figure 47). Ensuring that all installed PMTs are functioning properly is a high priority in order to maintain a high quality of reconstruction.

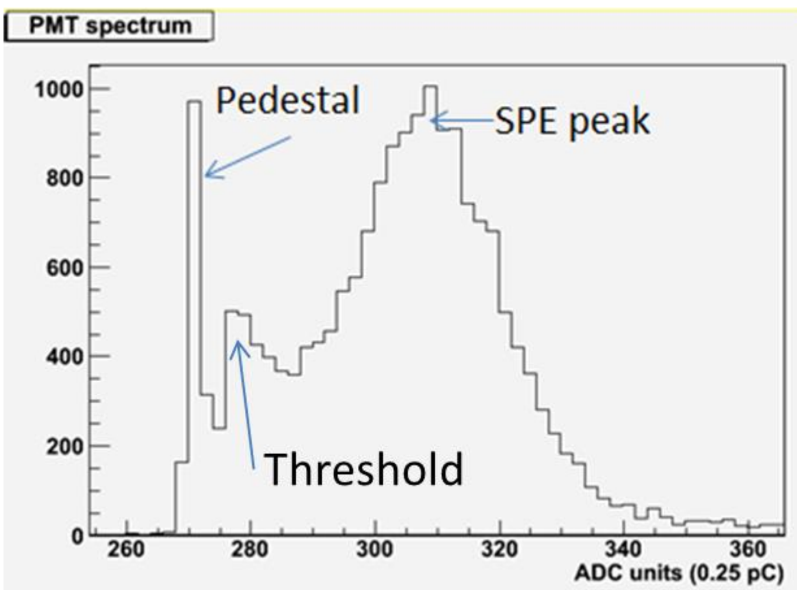

Figure 47: SPE spectrum of Detector PMT self-triggered at ¼ SPE with fixed trigger pedestal

Initial characterization tests of the Detector PMTs were performed by collaborators in Heidelberg, Germany at the Max Plank Institute of Physics (MPIK) [30] and concurrently in Japan at the Tokyo Institute of Technology (TiTech) [31]. With independent testing systems, each institution verified the quality of the PMT and determined the High Voltage corresponding to a gain of 10^7. The PMTs in Japan were transported to MPIK, and the tests were repeated to ensure that there was no damage during transportation. While in Germany, cross checks between the two testing systems was performed and good agreement was confirmed.

After the Far Detector was completed, it was found that the PMTs were emitting light and adding to the trigger rate of the detector. Follow-up test determined that all the

PMTs produce light emissions but a handful occurs at a rate above 100 Hz. To reduce the light emission in the near detector a black covering was included around the PMT base and the PMTs with the highest glowing rate are to be used as spares.

I was responsible for the onsite quality test of the inner detector PMTs for the dear detector. Since the detector PMTs have good SPE resolution we obtain the SPE spectrum by self-triggering at the ¼ SPE. Pedestal measurements were taken during the test runs using a fixed trigger. In order to determine the gain of the PMT, the spectrum was fit with two Gaussians and a decaying exponential. The mean of the two Gaussians was used as input into the equation (1) to determine the gain.

$$gain = \frac{(\mu_{SPE} - \mu_{Pedestal}) * 0.25 \frac{pC}{ADC\ channel}}{2 * e * Amplification}$$

In addition to the gain: the Peak-to-Valley Ratio, sigma of SPE, Dark Rate, and pulse shape were all checked for each PMT and the results are shown below(Figure 48-Figure 51).

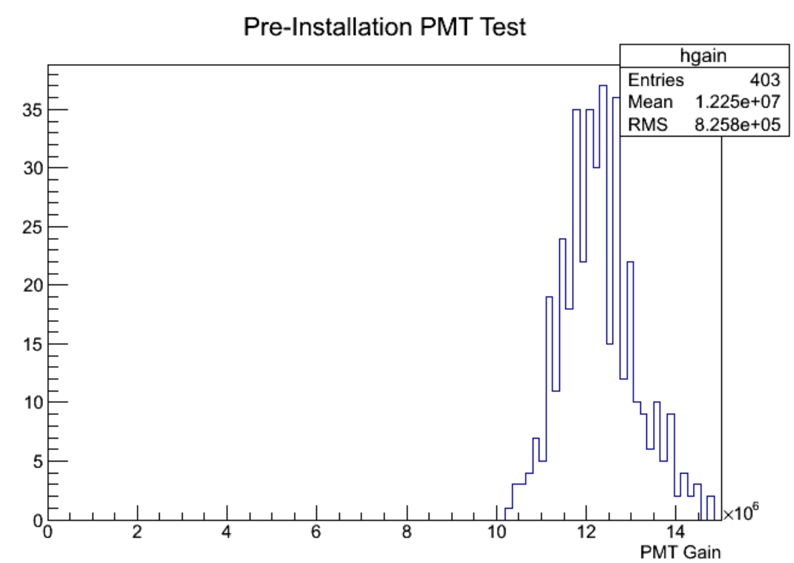

Figure 48: Pre-Installation Test Results for Detector PMT Gains

As a result of the Pre-Installation Tests 11 PMTs were rejected from installation in the Near Detector. The PMTs and the reasons for withholding them from installation are shown in Table 5. There were a total of 403 PMTs tested but only 390 were needed in the Detector, so that there was no need to install rejected PMTs.

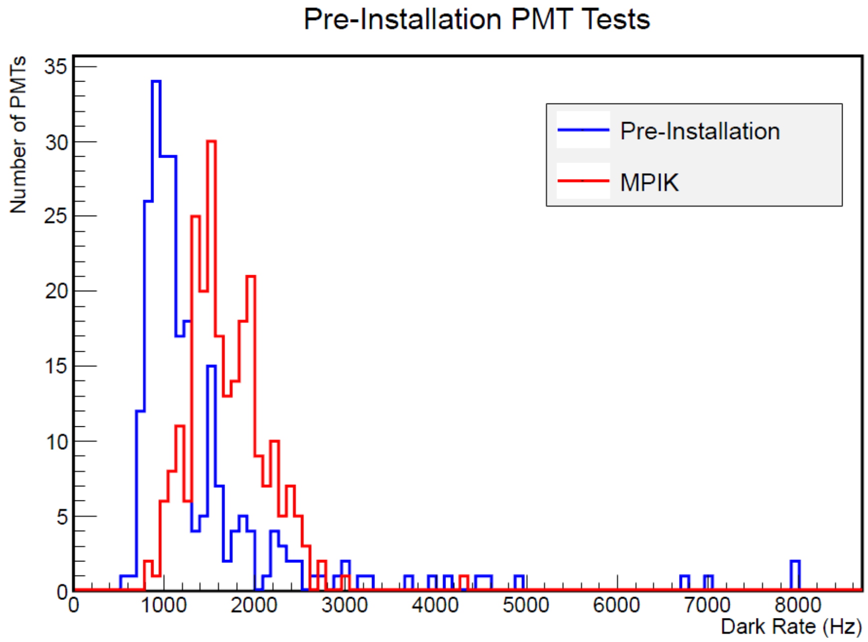

Figure 49: Pre-Installation Test Results for Detector PMT Dark Rates

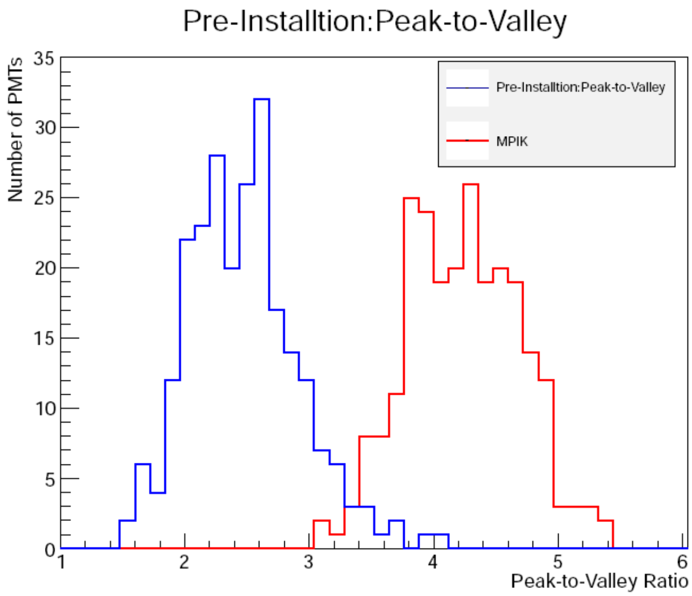

Figure 50: Pre-Installation Test Results for Detector Peak-to-Valley Ratios

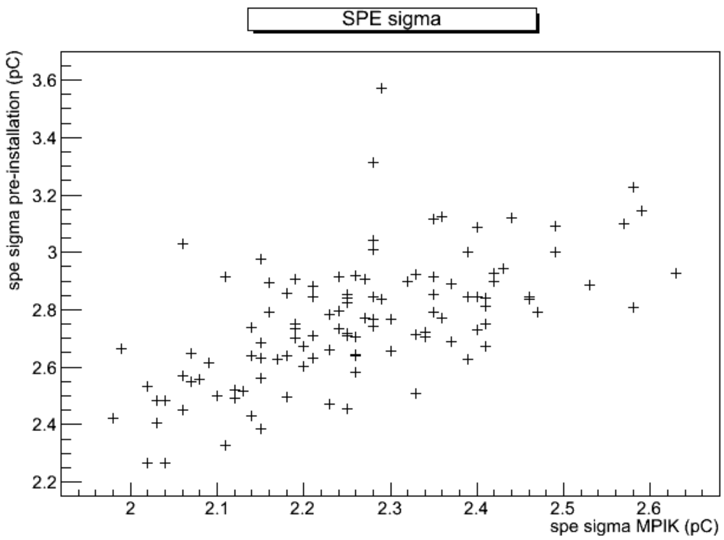

Figure 51:**Testing Result for Detector PMT Peak-to-Valley Ratio and σ_{SPE}**

Table 5: Detector PMTs rejected from installation in Near Detector

PMT Serial Number	Reason for Rejection
JP 1090	σ SPE wide
JP 856	Dark Rate 3300 Hz
GE 867	Glow Rate 133 Hz
JP 1088	σ SPE wide
GE 636	Glow Rate 174 Hz
JP 1129	Glow Rate 200 Hz
JP 644	Glow Rate 224 Hz
GE 700	Glow Rate 325 Hz
JP 622	Glow Rate 423 Hz
GE 1149	Dark Rate 6200 Hz
GE 615	Dark Rate 6700 Hz

In-situ PMT test and results

The Detector PMTs were installed in two phases. In phase 1 the 330 PMTs on the bottom and side of the buffer vessel were installed, completed in December 2013, in phase 2 the 60 PMTs on the buffer lid were installed in spring 2014. After Phase 1 was complete, the 330 PMTs were tested in-situ. In order to do these test the PMTs needed to be shielded from all light. To accomplish this, the PMTs were covered with two layers of black bag, there was a large black plastic sheet that covered the detector pit, and the tests were performed with the laboratory lights off (Figure 52). The UT testing system was used at this time, but the electronics were altered to readout 8 channels at a time instead of just one. The testing plan was to set all 8 PMT thresholds to ¼ SPE and take all the same measurements that were done in the pre-installation phase. To get a pedestal measurement in the pre-installation tests a fixed trigger was used, in the post test an external fixed trigger was unnecessary because a SPE in one PMT would cause pedestal trigger in the other seven .

The in-situ tests were performed to ensure that all PMTs installed were functioning. This was the last time that PMTs could be replaced before the detector was sealed and filled with liquid. In addition to ensuring the quality of all installed PMTs, the in-situ tests were the first test of the mapping between: PMTs, splitter boxes, High Voltage supply channels and front end electronic (FEE) connectors and the first test of the HV system.

Once all preparations for the in-situ test were complete we found that it was impossible to take measurements with the thresholds set to ¼ SPE because of a higher noise level in the PMT signal cables (more details will be given in the next section), but as a result the threshold was set to ¾ SPE. Due to this change the Dark Rates, peak-to-valley ratios and σ_{SPE} cannot be directly compared between the pre-installation test and the in-situ tests. The results from the Gain Measurement are shown below in figure 12 and they show that all Detector PMTs are functioning properly.

During the in-situ test we discovered 4 mislabeled signal cables, 18 FEE connectors that need to be replaced, one HV channel that was not working and two HV channels that experienced cross talk to their nearest neighbors. We also tested the IV PMTs that were installed in phase 1 and found one that gave no signal. This PMT had a short between its signal and ground possibly due to damage during the lowering of the buffer vessel into the IV. All the faults we discovered were successfully corrected.

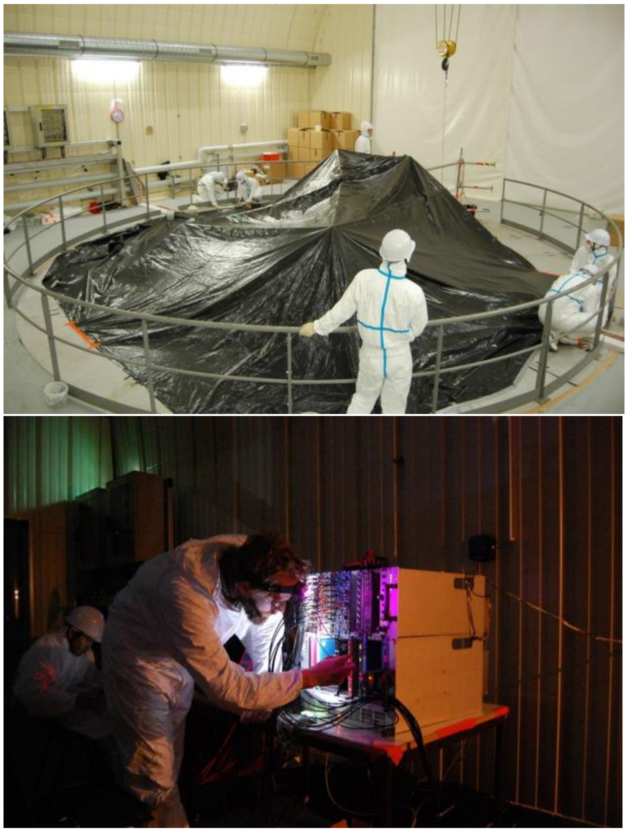

Figure 52: Preparing for In-Situ tests by covering the detector put with black plastic (top) and preparing 8 Channel Readout electronics (bottom)

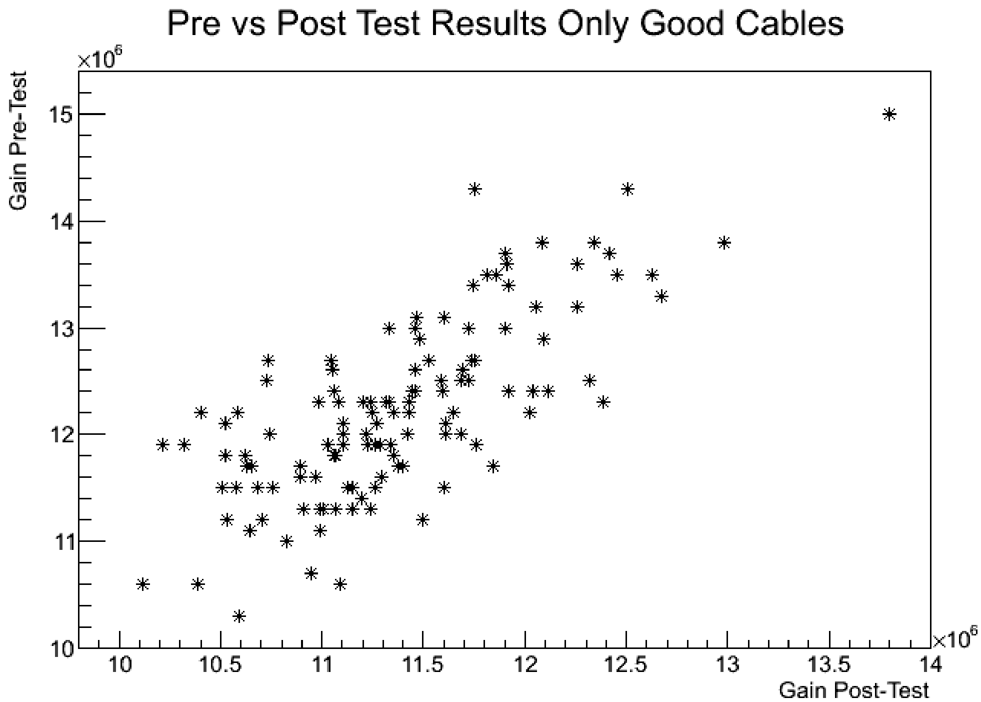

Figure 53: Pre-Installation vs. In-situ PMT gain (only "good" cables are plotted)

Cable Noise
During in-situ PMT testing there was a higher level of background noise observed in ~1/2 the PMTs. I discovered that two different types of cable were used for propagating the PMT signal from the splitter box to the FEE. One cable has a silver braided shielding and one has a copper braiding and a foil shielding (Figure 54). There was a strong correlation between the amount of noise in the cable and the type of cable. At the time the source of the noise was unknown but it was concluded that the foil cables were of a lower quality and would possibly need to be replaced (Figure 55).

To determine whether or not the foil cables needed to be replaced, dedicated noise test were taken. It was found that the noise could be a potential problem because coherence between multiple cables could swamp the trigger system with fake signals (Figure 56). Different resistivities of the cables were measured and might account for the larger noise pickup of the foil cable. Finally, it was found that grounding the metal cable tray to the outlet ground removed the noise from the foil cables. While the exact source of the noise is still unknown, the new grounding configuration gave us confidence that the noise would not be a problem in the final configuration, as long as the electronics system was properly grounded.

PMT installation Conclusions

The Double Chooz PMTs were tested and retested including initial quality test, onsite quality tests, and in-situ test. As a result of all these test the PMT system was delivered to the collaboration with every single PMT functioning. This was a necessary but tedious and thankless job that fulfilled the University to Tennessee’s responsibility to the Double Chooz PMT working group.

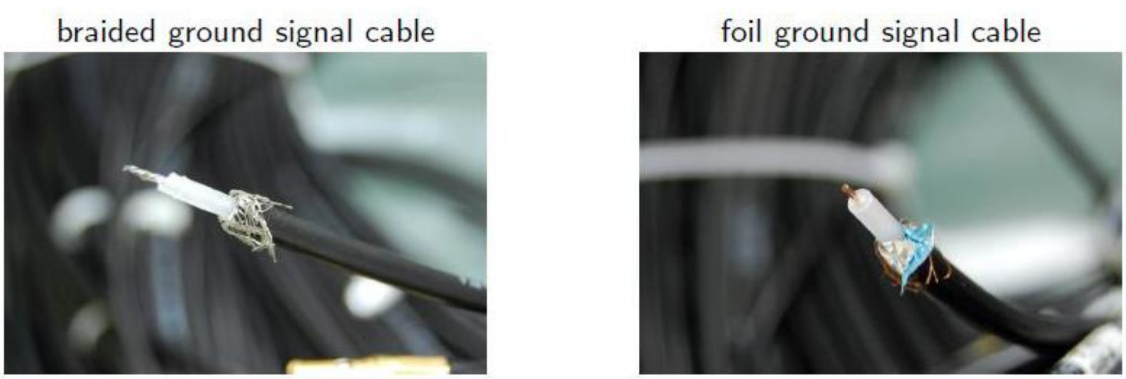

Figure 54: Photos of the two types of signal cables

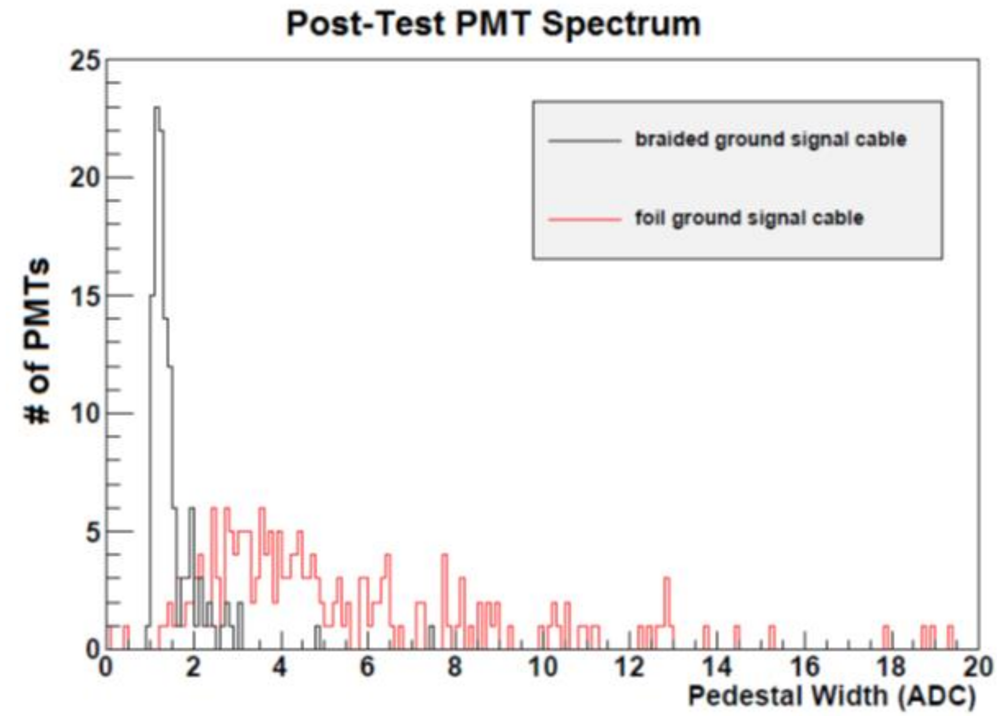

Figure 55: Pedestal widths of Near Detector PMTs. "Foil" cables show more noise pick-up than braided cables

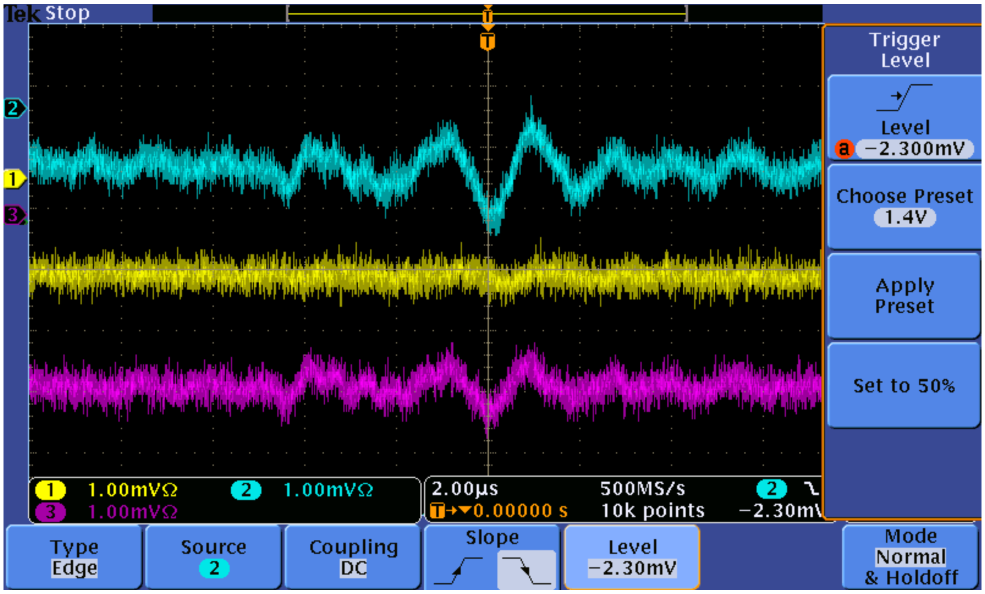

Figure 56: Coherence between foil cables (teal and purple) and proper shielding of a braid cable shows very little noise (yellow)

Chapter VI: Double Chooz Single Detector

Neutrino Signals

Neutrinos interact inside the Double Chooz Target via Inverse Beta Decay (IBD) (Equation 4, Figure 57). The characteristic signal for an IBD event contains a prompt and delay signal. The prompt signal is given by the positron scintillation and subsequent annihilation while the delay signal is from thermal neutron capture on a nucleus.

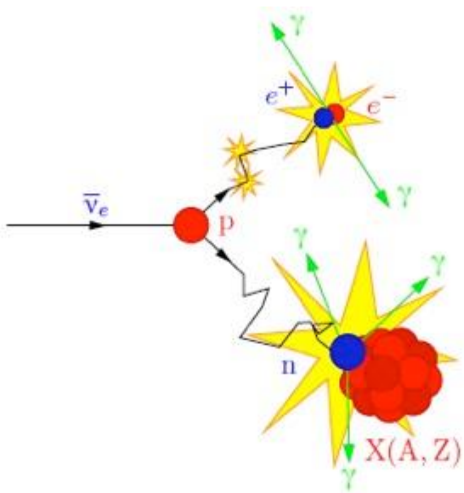

Figure 57: Inverse Beta Decay schematic

The delay signal is delayed in time from the prompt signal because of the time it takes a free neutron to thermalize and capture within the scintillator. Inside the DC Target, which contains Gd, the mean lifetime for a neutron to capture is 30 µs whereas in the Gamma Catcher, which has no Gd, the capture time is ~200 us (Figure 58).
The energy observed from the prompt signal is related to the neutrino energy associated with the interaction (Equation 5).

Equation 5: Relation between Detected energy and Neutrino Energy

$$E_{obs} = E_{\bar{\nu}} - 0.78\ MeV$$

The delay signal does not contain any information about the initial neutrino energy and only depends on the nuclear de-excitation of the Gd (or H). Hydrogen de-excites with a single 2.2 MeV gamma while Gd de-excites with multiple gammas with a mean energy of 8 MeV and mean gamma multiplicity of 5. For naturally occurring Gd, the main isotopes and their cross sections are shown in (Figure 59). The two isotopes with the highest cross section, ^{155}Gd and ^{157}Gd, dominate the neutron captures.

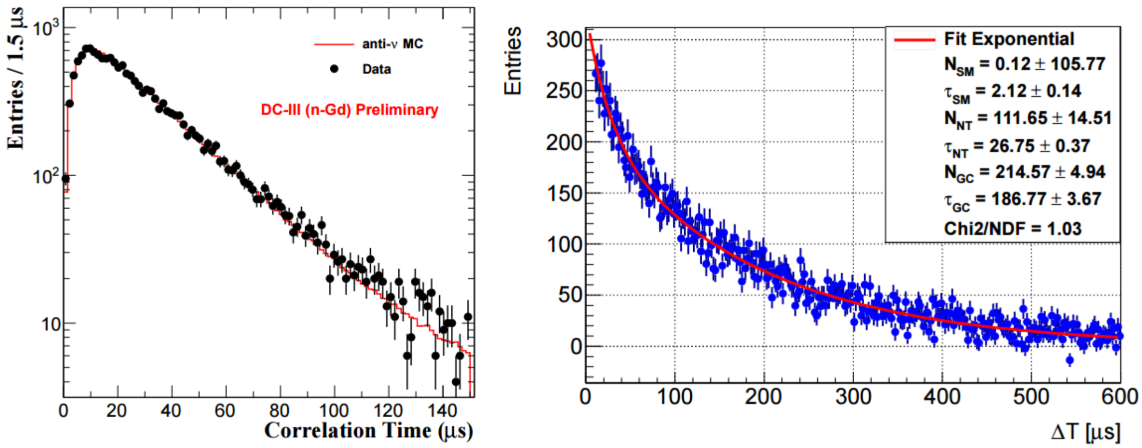

Figure 58: Time between IBD Prompt and Delay for Gd selection (left) and H selection(right). The n-Gd capture has a mean capture time of 30us while the n-H has a capture time of ~200 us.

Thermal Capture Cross Sections: A Comparison of ENDF/B-VI to RPI Results*

Thermal Capture Cross Sections							
		ENDF			RPI		
Isotope	Abundance	Thermal Capture	Contribution to Elemental	Percent	Thermal Capture	Contribution to Elemental	Percent
^{152}Gd	0.200	1 050	2.10	0.00430	1 050	2.10	0.00430
^{154}Gd	2.18	85.0	1.85	0.00379	85.8	1.87	0.00422
^{155}Gd	14.80	60 700	8 980	18.4	60 200	8 910	20.1
^{156}Gd	20.47	1.71	0.350	0.000717	1.74	0.356	0.000804
^{157}Gd	15.65	254 000	39 800	81.6	226 000	35 400	79.9
^{158}Gd	24.84	2.01	0.499	0.00102	2.19	0.544	0.00122
^{160}Gd	21.86	0.765	0.167	0.000342	0.755	0.165	0.000372
Gd	—		48 800	100.0		44 300	100.0

*The units of all cross sections are barns. The units of abundance are percent.

Figure 59: Gd Natural abundance and thermal Neutron Capture Cross sections.

Background Signals

The double coincidence requirement for and IBD signal results in an enormous background suppression from uncorrelated energy depositions (accidentals), however there are a few sources of background that mimic the IBD double coincidence. The isotopes, Lithium-9 and Helium-8, are short lived and undergo beta decay while simultaneously emitting a neutron. This decay results in a double coincident signal. Similarly, muons which stop inside the detector volume can decay with a Michel electron with a 2.2 μs half-life causing a double coincidence. Finally, fast neutrons can be created in high number through muon spallation with rock. These neutrons can enter the detector and create multiple events in short time intervals, thereby faking IBD coincidence. In this section I will explore each of these backgrounds in more detail and describe methods to veto and estimate their rates.

Accidentals

After vetoing the large signals cause by Muons and imposing a 1 ms veto after each muon, and rejecting Light Noise events that are not point like energy depositions. The resulting rate of events (Singles) is ~12 Hz. The Energy Spectrum of the Singles is dominated by radioactive decay of Isotopes such as K^{40}, Tl^{208} and Bi^{214} these isotopes are commonly occurring in the earth and are present in trace amounts in most materials (Figure 60). The glass of the PMTs is a large contributor of K^{40} because potassium is used to make glass while the Thallium and Bismuth are part of the decay chains of Thorium and Uranium respectively.

With a Singles rate of 12 Hz the average time between each event is 83 ms this time scale is much too long to mimic a IBD double coincidence , but there is a small chance that two events will randomly occur within the time window of double coincidence. The rate of accidental coincidence is measured using an off-time window where the delay and the prompt are separated by more than 1 second. The resulting rate of accidental background in the Gd sample is 0.070±0.003 events per day. In the Hydrogen analysis the accidental rate is higher due to the frequency of events in the delay energy window of hydrogen capture. Since Gadolinium capture, with its resulting 8 MeV gamma cascade, is much higher energy than the typical singles even it is suppressed compared to the 2.2 MeV of hydrogen capture. The resulting rate of accidental coincidence in the Hydrogen analysis is 4.33±0.01 events per day.

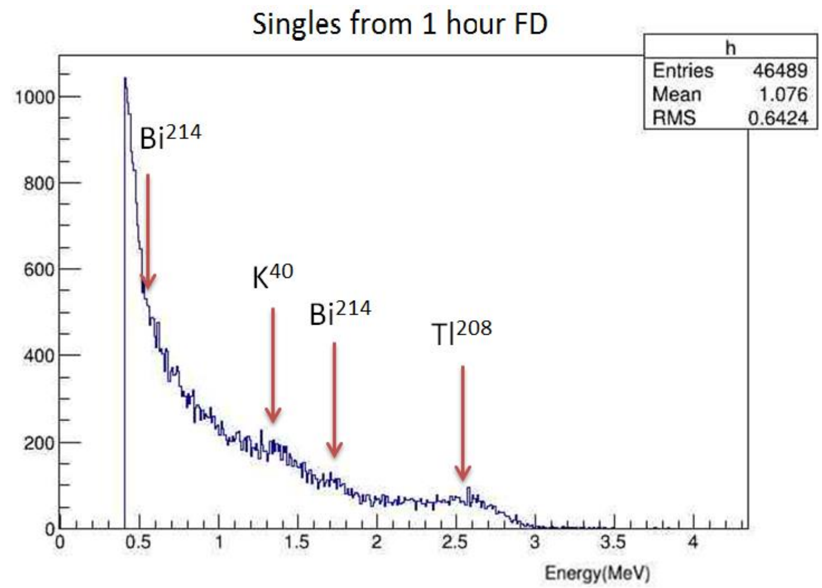

Figure 60: Singles spectrum in the Far Detector. Commonly occurring radioactive elements dominate the spectrum.

Lithium-9 and Helium-8

Muons which are products of cosmic ray showers interact with the detectors at a rate of ~40 Hz in the Far and ~ 250Hz in the Near. The majority of these (~3/4) pass only through the Inner Veto. Most of the time when a muon passes through the detector it does so as a minimum ionizing particle. Occasionally, the muon causes the more violent process of spallation where it transfers enough energy to a nucleus to make it become unbound. The end result of this process is that the parent isotope breaks into two or more parts. Every isotope that can be created will be created (Figure 61). The majority of parent elements in the central detector are Carbon, Nitrogen, and Oxygen. Gadolinium exists but the mass of Gd is much smaller than the other elements and will be ignored.

Of all the possible products of spallation Figure 61 only two can mimic an IBD signals. ^{9}Li and ^{8}He both undergo β^- or β^- n decay meaning they emit an electron or an electron and a neutron. In the case that they β^- n decay they will mimic an IBD event because the electron causes a prompt and the neutron thermalizes, is captured, and cause a delay. If we could tell the difference between positrons and electrons it would be possible to discriminate between these signals but we cannot. ^{9}Li has a Q-value of 13.6 MeV, a half-life of 178ms and a 50% probability to β^- n decay while ^{8}He has a Q-value of 10.6MeV, a half-life of 119 ms and a 16% probability to β^- n decay. From now on I will refer to the mixture of lithium and helium simply as lithium. Since both these isotopes live much longer than the 1 ms veto after muons they will enter into the neutrino sample.

One way to determine the rate of ^{9}Li and ^{8}He is to look for the triple coincidence of muon, prompt, delay. Due to the high rate of muon for every IBD event there will be many muons within a few half-lives of ^{9}Li and ^{8}He. If the event is a neutrino IBD then on average the preceding muons will be randomly distributed. If the event is a ^{9}Li or ^{8}He that is mimicking the IBD signal then there will be an excess of muons in the window corresponding to the half-life or ^{9}Li and ^{8}He which can observed in Figure 62.

The Lithium enriched sample only includes muons that have more than 600 MeV deposited in the Inner Detector or muons that deposit more than 300 MeV with at least one neutron in the 1 ms window following. This sub sample of muons is more likely to produce ^{9}Li. Including the muons that only pass through the Inner Veto or only clip the central volume increases the flat background to such a level that makes the Lithium decay signal hard to discern. It is possible that the clipping muons will produce ^{9}Li but since they are not included in the enriched sample the enriched sample gives only a lower estimate for the total Lithium rate. To increase the purity of the sample there is a requirement that the IBD prompt-delay pair should occur within 0.75 m of the muon track. The spatial cut was chosen by obtaining a clean sample of ^{9}Li by selecting IBD events in coincidence with muons that containing more than 600 MeV (Figure 64).

		^{12}N	^{13}N+	—	—	^{16}N	^{17}N	^{18}N
^{9}C	^{10}C+	^{11}C+	—	—	–	^{15}C	^{16}C	^{17}C
^{8}B		—	—	^{12}B	^{13}B	^{14}B	^{15}B	
–		—	–	^{11}Be	^{12}Be		^{14}Be	
—	—	^{8}Li	^{9}Li		^{11}Li			
	^{6}He		^{8}He					

Figure 61: Possible end products of Spallation on ^{18}O. Long dash denotes a stable isotope and short dash denotes long lived isotope, + denotes an isotope that undergoes β^+ decay.

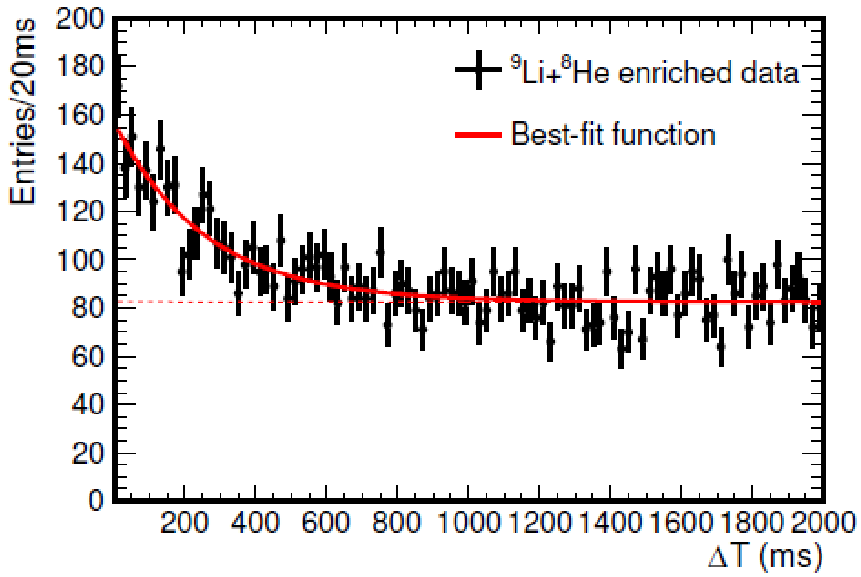

Figure 62: Time between Muon and Prompt for the Li-enriched sample.

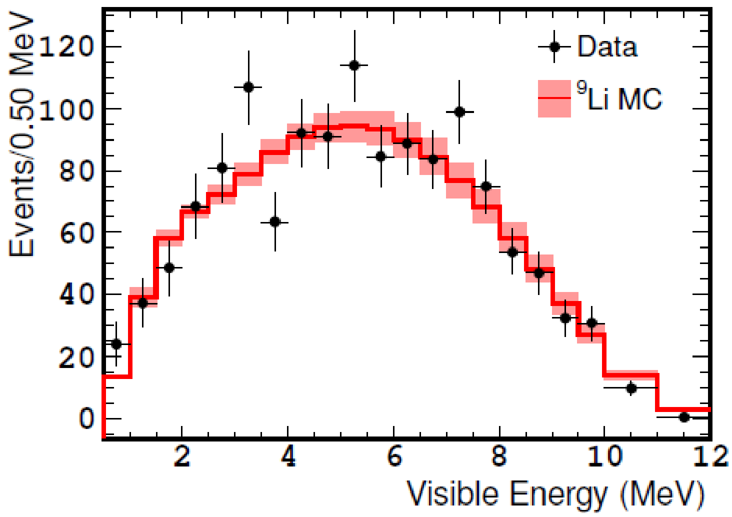

Figure 63: Events selected as ^{9}Li by the lithium likelihood veto. Overlaid in red is a Monte Carlo prediction of the ^{9}Li decay spectrum.

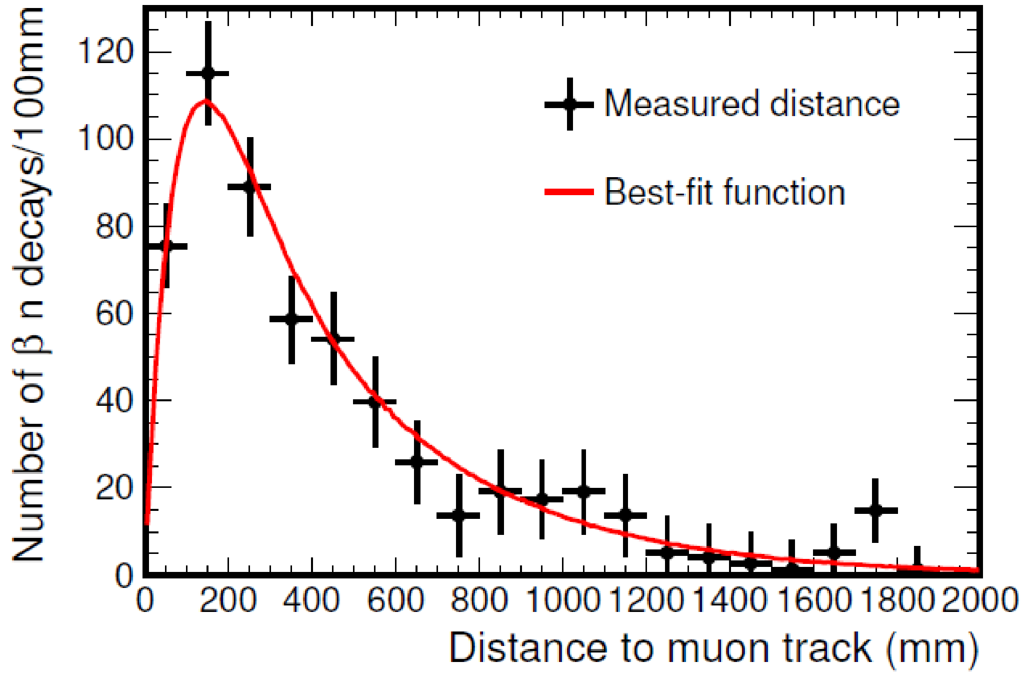

Figure 64: Lateral distance profile for Muons above 600 MeV and the following IBD candidates. The best fit function is a decaying exponential convoluted with a Gaussian to take into account vertex reconstruction smearing of the Muon track and the Li-9 event.

Another way to identify ^{9}Li in the detector is by using a likelihood approach. The Lithium likelihood predicts the probability that a Muon-IBD pair is actually ^{9}Li. To compute the likelihood, PDFs are generated for the distance between the Muon track and the IBD vertex and the number of neutrons following the muon. The PDFs are generated for ^{12}B events which are also made by muon spallation, but they have higher statistics. Other variables such as the Muon Energy, and the de/dx of the parent muon were tested but do not make the likelihood a better discriminator. The Lithium Likelihood Veto rejects 55% of the Lithium events in the FD Gd selection. The spectrum of the events rejected by the Lithium Likelihood veto is shown in Figure 63. It matches well the predicted shape so that we are confident that we are selection ^{9}Li events and not IBD events.

Fast Neutrons and Stopping Muons

Fast Neutrons created by spallation muons interacting with surrounding rock can enter the detector without depositing enough energy in the Inner Veto to satisfy the Muon definition. The fast neutrons can undergo nuclear recoil with protons in the target mimicking prompt or delay events. Since many neutrons can be created during the spallation process, multiple fast neutrons can interact in time coincidence to mimic an IBD signal. Often these fast neutrons make small energy depositions inside the Inver Veto but it is not enough to satisfy the IV muon threshold. These events can be tagged and rejected by examining the Inner Veto activity in coincidence with a prompt delay pair.

Muons can enter the detector through the chimney, thus avoiding detection by the Inner Veto. If the muon stops after passing through only a few cm of scintillator and then decays via Michel electron, it can mimic a prompt-delay event but instead of having a mean Δt of 30 μs these events show the 2.2 μs half-life of a muon at rest. In both the Near and Far detectors there is the Upper Outer Veto which lies above the chimney and can serve as an additional tag for rejecting stopping muons.

Muons

Muons are created as secondary particles in cosmic showers. Since they have large energies they can penetrate the earth and interact with our detectors. The muon flux and spectrum depends on the depth of the detector. The Near detector at only ~100 m.w.e. receives a muon rate of about 250 Hz while the Far detector, at 300 m.w.e. receives about 40 Hz. Muons impact the detectors ability to detect neutrinos in two ways. First, they create backgrounds like ^{9}Li and fast neutrons mentioned above. Secondly, following a muon signal there is a 1 ms veto applied in the software in order to neglect the many neutrons that can be created due to spallation. In the far detector this results in a dead-time of ~5% and in the near ~20%.

Light Noise

When the far detector was commissioned an unexpected rate of coincident triggers was observed that was correlated with the number of PMTs that were active. This indicated that the source was coming from the PMTs themselves. Follow-up external laboratory test revealed that with high temperatures and voltages it is possible to cause coronal discharge in the transparent epoxy that was used to bind the PMT base (sight Light noise paper when published). If the light is seen by many PMT it can cause the detector to trigger. These events are called Light Noise events.

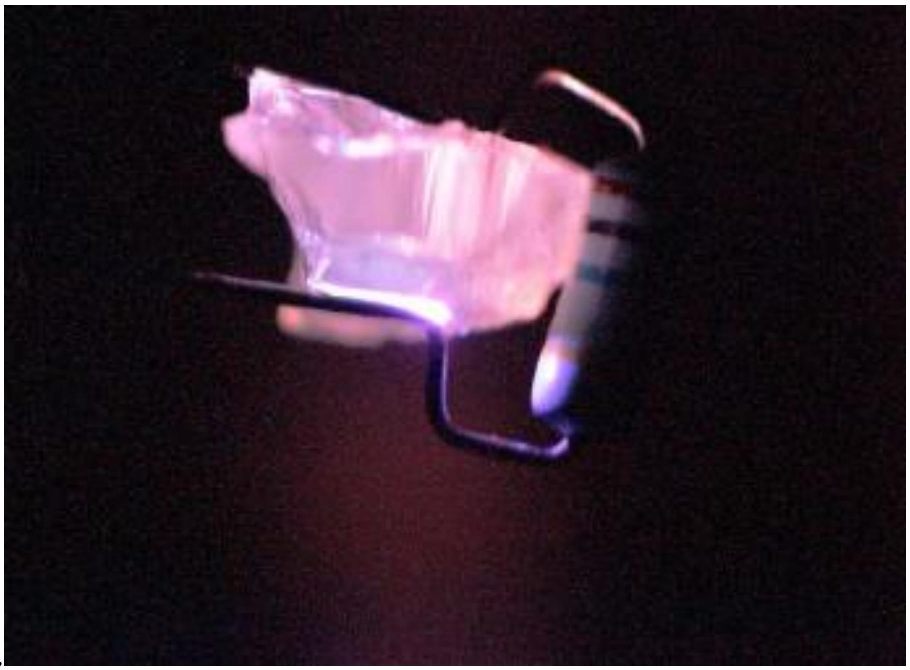
.

Figure 65: A sample of epoxy used in the PMT base is glowing when high voltage is applied.

The Light Noise is removed from the physics sample by making some quality cuts based on properties of the event reconstruction. The cuts are based on variables called Qdiff, Qmax/Qtot, QRMS and RMSTstart. Qdiff refers to the difference between the integrated charge between a PMT and its nearest neighbors. If a PMT is creating light it is likely that it will observe most of the light associated with the event. Qmax/Qtot is the ratio of the PMT with the maximum charge received over the total charge of the event. Again single PMTs that observe most of the charge are likely emitting the light. Finally. QRMS is the RMS of charge distribution seen by all PMTs for a single event and RMSTstart is the RMS of the start time of the PMT pulse. Events that occur in the center of the detector will have smaller RMSTstart times and smaller QRMS than events that originate at a PMT base. The light noise rejecting cuts are as follows: Qdiff<50000 duq**,** Qmax/Qtot<0.12, and (RMSTstart<36 OR QRMS < 464 - 8*RMSTstart) the cut based on QRMS and RMSTstart can be seen in Figure 66.

When the light noise was first discovered it was determined that 15 PMTs were responsible for a large portion of the light noise. These PMTs were switched off for the first two years of the Far detector data collection period. Once it was well established that the Light Noise could be controlled through offline cuts the 15 PMTs that were switched off were activated, so that currently no PMTs are switched off. Over time it was found that the rate of Light Noise events was increasing. In fact, currently the light noise rate is 250Hz up from an original rate of 30 Hz. The high rate is partially due to the increase in time and partly due to an increase in HV and more PMTs being on. The high rate of Light Noise can stress the DAQ by causing a higher data volume but it does not impact ability of the detector to detect physics events Even though the rate of light noise is increasing the physics events are constant as seen in Figure 67.

In an effort to reduce the rate of light noise triggers in the Near detector an opaque black plastic sheeting was installed on the PMT base (Figure 68). Initial results show that the black plastic reduced the light noise rate to less than 10 Hz. One demonstration of the marked improvement is seen in Figure 69 where the extra light noise population to the right of the cut line is seen in the Far detector but not the Near. Understanding light noise in Double Chooz will have an impact on future experiments that plan to use large number of photomultiplier tubes. It is important to have PMT bases that are optically separated from the detector volume. This can be achieved simply with opaque shielding around the base or possibly with opaque epoxy.

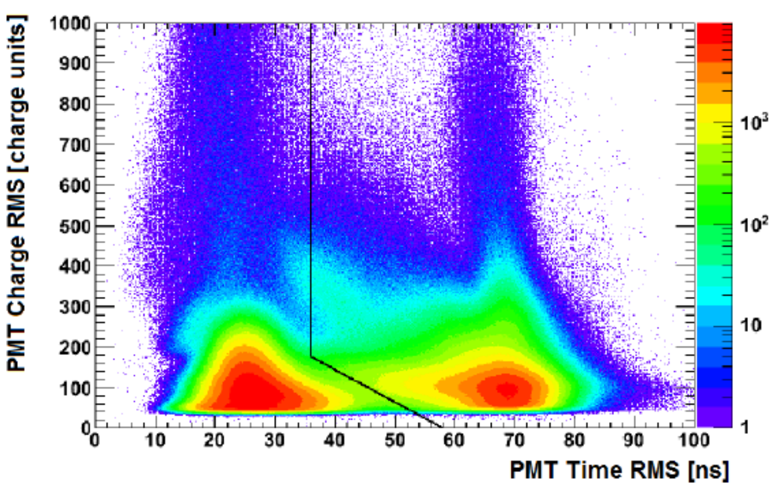

Figure 66:QRMS and RMSTstart cut is defined by the black line. Two populations are seen with Light Noise is defined as events to the right of the line and physics events to the left.

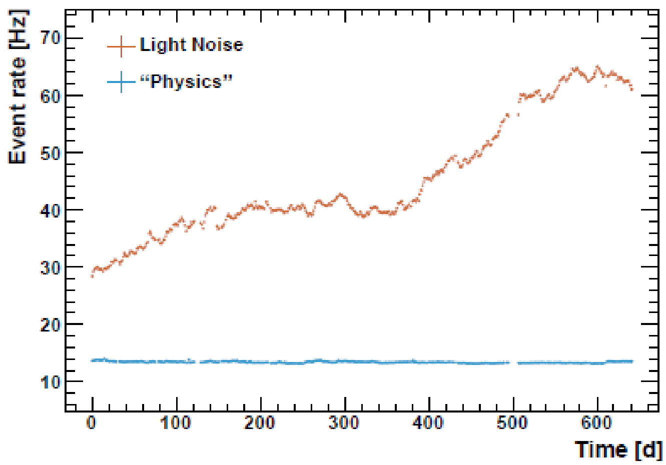

Figure 67: Light Noise and Physics event rate for the first two year data set of the Far detector.

Figure 68: (Left) PMT base as it is in the Far detector. (Right) PMT base covered with black plastic to reduce light noise for the Near detector.

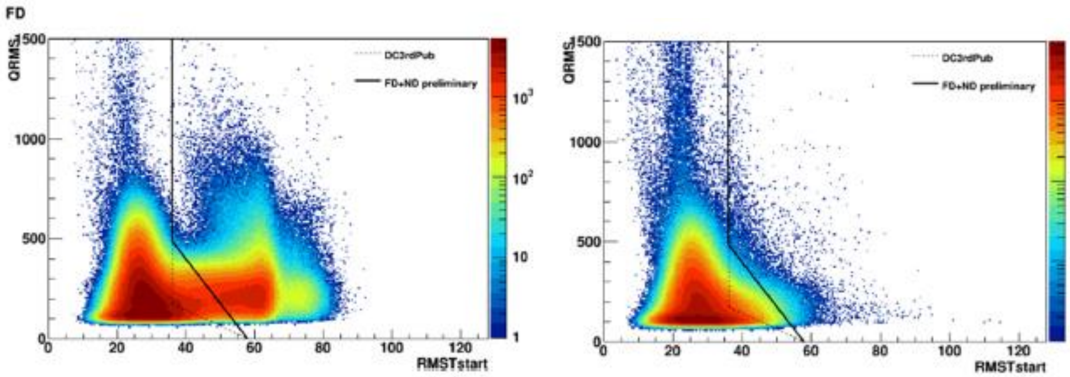

Figure 69: (Left) Light noise variables for the Far detector. (Right) same variables for the Near detector. Light Noise is greatly reduced in the ND due to the black plastic covering the base.

One Detector θ_{13} results

Double Chooz was designed to be a phased experiment. In the final operational phase the near detector measures the un-oscillated reactor flux and the far measure the oscillated flux. The far detector was constructed 4 years before the near detector. At that time there was no evidence that $\sin^2 2\theta_{13}$ was not zero and so the logic was to first confirm that there was a hint of neutrino oscillation with one detector before deciding to build two detectors to make a precise measure of it. In the one detector phase of Double Chooz we rely on a model of the reactor to make a prediction of the neutrino flux and spectrum. This section describes the results for the time period with only one detector.

Gadolinium

With a data set of 467.9 live days in the far detector we are able to measure anti-neutrino disappearance resulting in a $\sin^2 2\theta_{13}=0.090^{+0.032}_{-0.029}$ [32]. Neutrinos are selected by looking for a prompt-delay pair of events separated by less than 150 µs, where the delay is a capture on Gadolinium. The selection process goes like the following:

1) Veto all muons and 1 ms following muons where muons are defined as any event in the Inner Detector with >20 MeV or an event in the Inner Veto with >16 MeV
2) Reject events that are likely Light Noise the meet the criteria Qmax/Qtot>0.12, Qdifference>30000 DUQ and StartTimeRMS>36 ns or QRMS > (464-8xStartTimeRMS)
3) Remaining events are called valid triggers. With the valid triggers we obtain an initial IBD selection by requiring the
4) prompt event with 0.5 MeV<Energy<20 MeV and a delay event with 4MeV<Energy<10 MeV be separated by 0.5µs<ΔT<150 µs and a spatial cut of ΔR<100cm between prompt and delay vertex (Figure 70)
5)There is a requirement that no other valid triggers occur in the window from-200 µs to 600 µs around the prompt event and the prompt-delay pair is not a likely Li-event as described by the lithium likelihood veto.
6) Events of cosmogenic nature are suppressed with additional requirements that there was no activity in the OV coincident with the prompt-delay pair, IV activity vetoes the pair if it occurs with 50 ns of the event and has a charge > 0.2 MeV with a position < 3.7m from the prompt.
7)The log likelihood fit of the vertex reconstruction(FuncV) has the requirement that delay energy > 0.068 x $e^{FuncV/1.23}$. This requirement ensures that the delay event is a point-like event and does not arise from multiple neutron scatters. This requirement is called the FV veto.

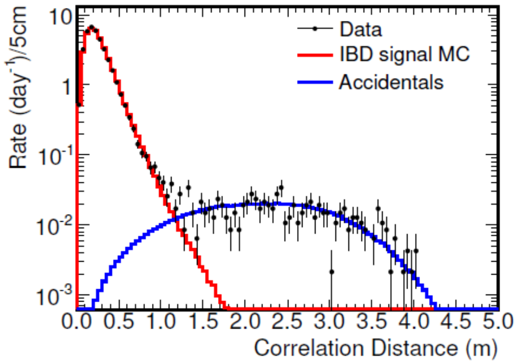

Figure 70: Correlation distance between prompt and delay for IBD signal and accidentals. This plot justifies the 100 cm cut in ΔR.

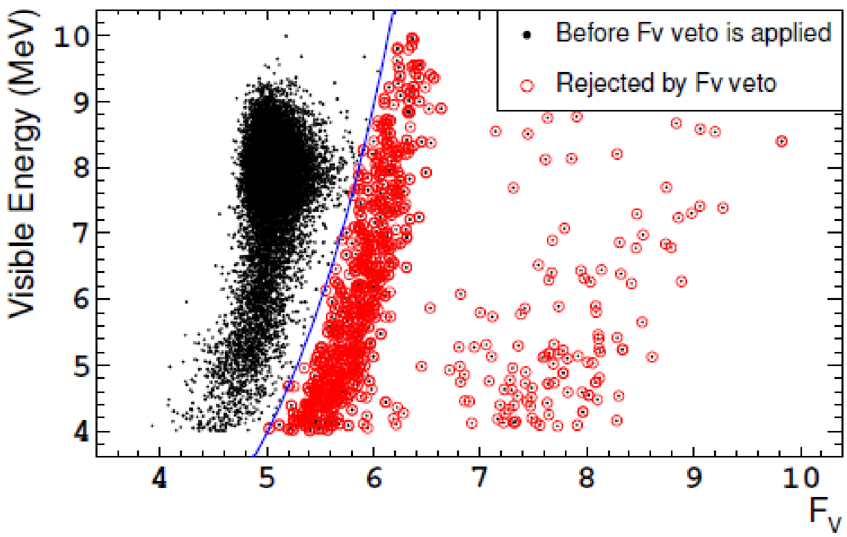

Figure 71:Population of Delay signals before FuncV cut is applied. The events to the left of the blue line are neutron captures on Gadolinium while to the right are events caused by fast neutrons or stopping muons.

The result of all these cuts is seen in Figure 72. The correlation time between the prompt and the delay for the IV Veto, OV Veto and FV Veto show a fast time component which is consistent with the 2.2 µs decay of a stopped muon. This is further evidenced by the shape of the delay spectrum which does not show n-Gd peak at 8 MeV for the case of the IV Veto and OV Veto events. Notice that both the correlation time and the delay spectrum of the Li+He Veto events are undistinguishable from the IBD events. The total IBD selectin inefficiency due to all the cuts is 1.4%.

The θ_{13} value obtained from this data set comes from a fit to the data of both the shape and the rate of neutrino compared to un-oscillated prediction. The best fit of θ_{13} can be seen in Figure 73 and the measured/predicted value in Figure 74. The expected oscillation pattern is seen in the energy range from 0-4 MeV, but there are significant deviations in the energy range from 4-7 MeV. In the region from 4.25-6 MeV the excess is 10% higher than expected with a significance of ~2σ. There is also a deficit of events in the 6-8 MeV range with a significance of ~1.5 σ. Various internal studies were performed to see if there could be an unaccounted background contributing in the energy range but no additional background was found. More likely is that the predicted reactor spectrum deviates from the actual reactor spectrum in this higher energy window. The events in the 4-6 MeV energy range are correlated with the reactor power (Figure 75). If the events were coming from a background there would be no correlation with the reactor power. This result supports the hypothesis that the shape prediction in this energy window is not precise. More discussion on the predicted reactor spectrum can be found in the section title “Reactor anti-neutrino Flux Prediction.” In the future the Double Chooz Near detector will provide valuable information about the reactor neutrino flux.

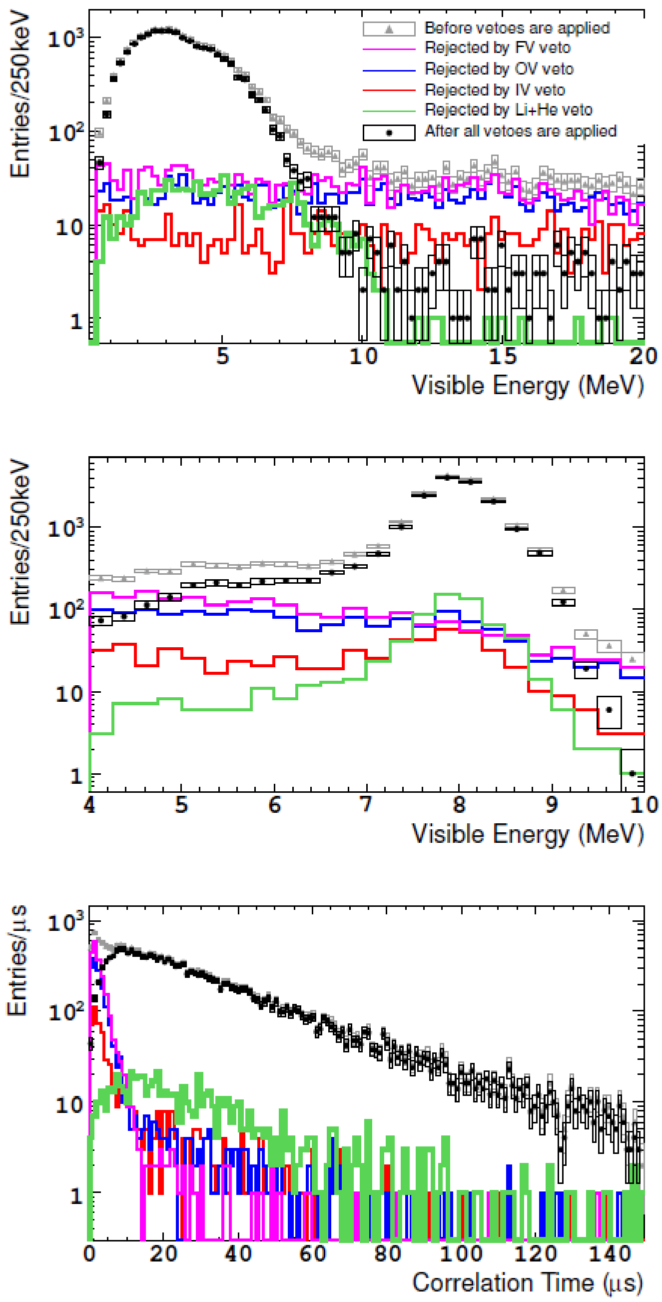

Figure 72: Distributions of the prompt and delay events. Colored lines show the events rejected by the various selection criteria.

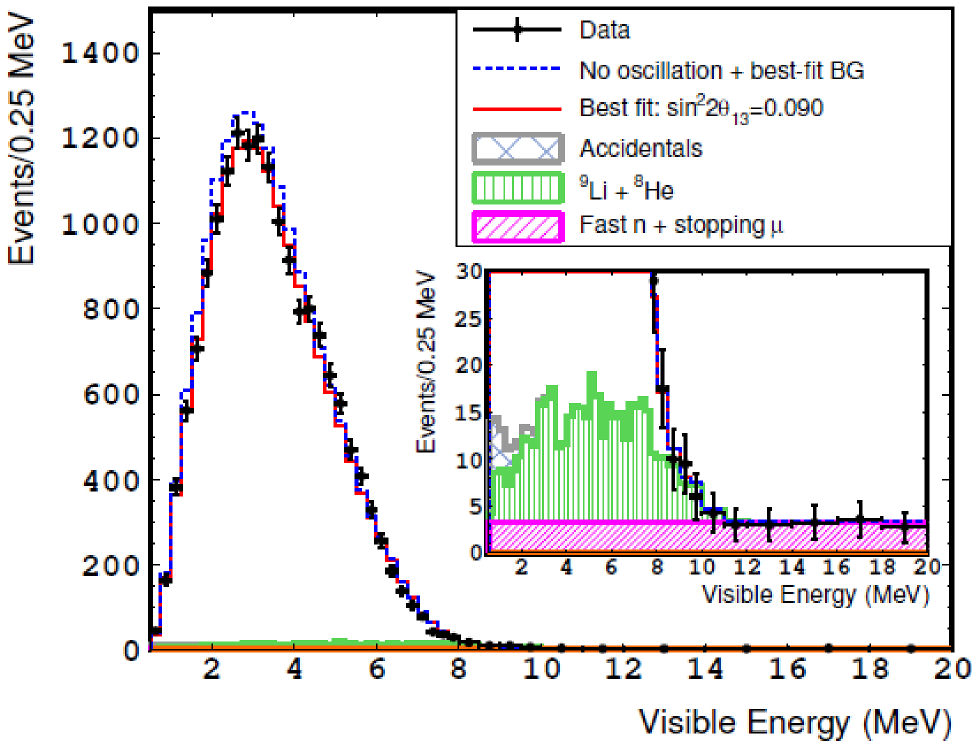

Figure 73: Observed neutrino spectrum with background overlaid with the best fit of $\sin^2 2\theta_{13}$.

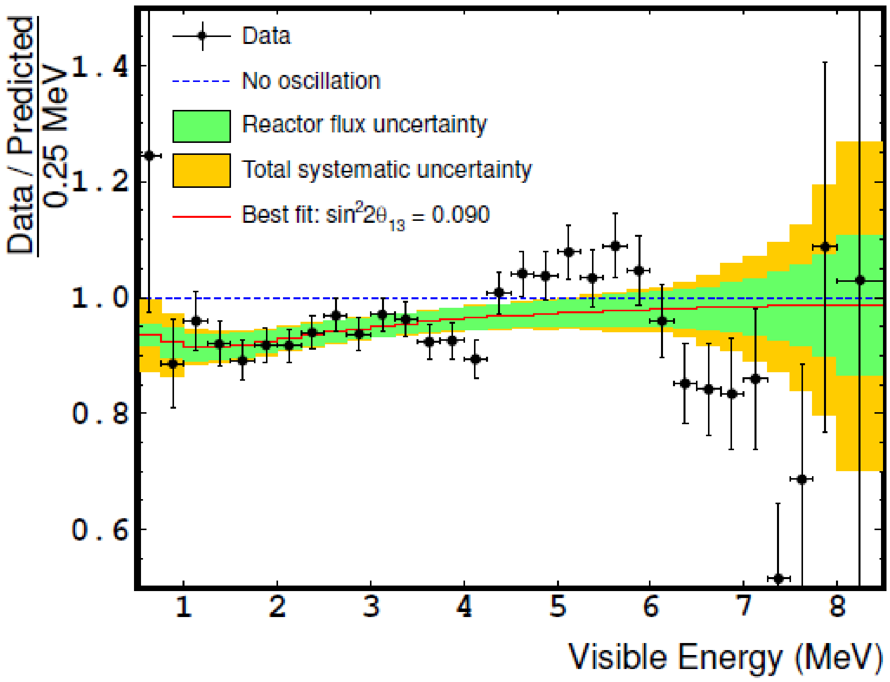

Figure 74: Black points show ratio of background subtracted data to un-oscillated prediction. Red line is the expectation assuming the best fit value of $\sin^2 2\theta_{13}$=0.09.

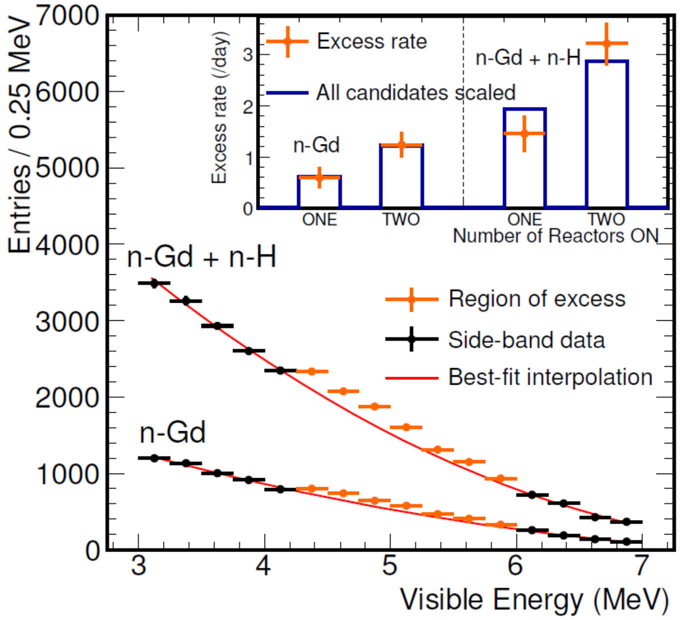

Figure 75: Excess in the 4.25-6 MeV window scales with the reactor power.

Hydrogen

The Double Chooz experiment was designed to detect IBD events with the neutron capturing on Gadolinium. However, it is also possible that the neutron will capture on Hydrogen. In the target, which is Gd doped, only 15% of neutrons will capture on Hydrogen, but in the Gamma Catcher almost all neutrons are captured by Hydrogen (a small percentage capture on Carbon). Since the gamma catcher is a larger volume using n-H capture to select IBD events results in about two time's greater statistics. While the statistics are greater the backgrounds and systematic uncertainties associated with the selection are also great resulting in a slightly less precise measurement of θ_{13} compared to the Gd selection. Double Chooz was the first reactor based θ_{13} experiment to demonstrate IBD selection with n-H capture [33] and is in the process of publishing an update with drastic BG reduction [34]. The background reduction is made possible by employing an Artificial Neural Network (ANN). The ANN uses as input: delay Energy, ΔT and ΔR. It is trained with a sample of accidental coincidences and a sample of IBD MC events. The Accidental background using the selection cuts as described in [33]result in an accidental background rate of 73.45±0.16 per day. The selection using the ANN criteria results in an accidental background rate of only 4.33±0.01 (Figure 76).

The measurement of θ_{13} was completed using rate only information since it has become apparent that the shape of the reactor spectrum is not well understood. The result of $\sin^2 2\theta_{13}=0.098^{+0.038}_{-0.039}$ is consistent with the measurement made with neutron-Gadolinium capture (Figure 76).

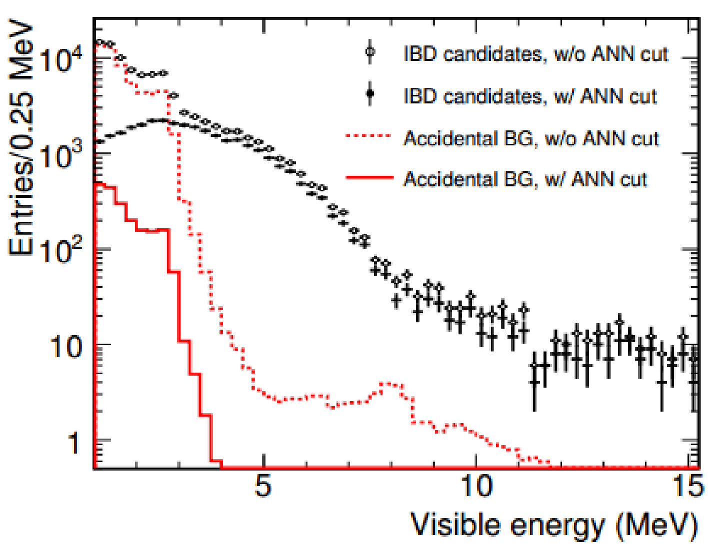

Figure 76: Performance of IBD selection using neutron capture on Hydrogen. ANN cut reduces drastically reduces the accidental background.

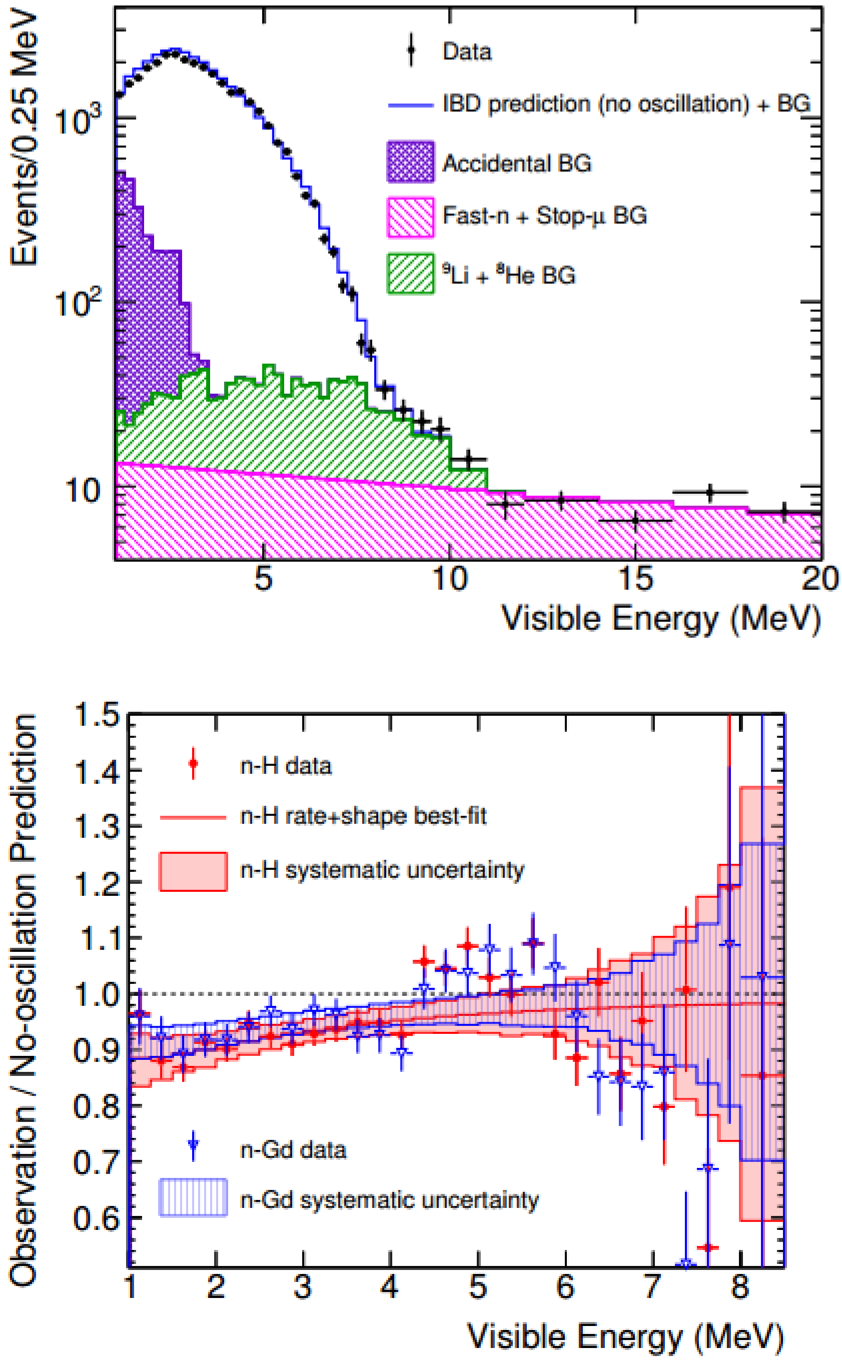

Figure 77: (top) Final IBD selection with backgrounds. (bottom) Result of observed/predicted ratio for different energy bins. Similar shape is seen for neutrino disappearance and 4-6 MeV excess in both n-H and n-Gd selections.

Worldwide θ_{13}

There are three reactor-based neutrino oscillation experiments currently running. There is Double Chooz in France, Daya Bay in China and RENO in South Korea. They all use similar detection technology with different configurations of detectors and reactors seen in Figure 78. The Double Chooz Collaboration was the first to publish a result of θ_{13} for both n-Gd capture and n-H capture. Double Chooz also has the largest uncertainties of the measurement because of lower statistics (both due to lower total reactor flux and smaller detector) and the fact that Double Chooz's publications to date only include results using a single far detector. Both Daya Bay and RENO are using near and far detectors.

The completion of the second Double Chooz detector will allow the Double Chooz Collaboration to make a precise measurement of the θ_{13} angle after a few years of running. Future experiments which seek to measure the CP-violating phase depend on knowledge of θ_{13} and therefore it is important to affirm its value which has been determined by Daya Bay.

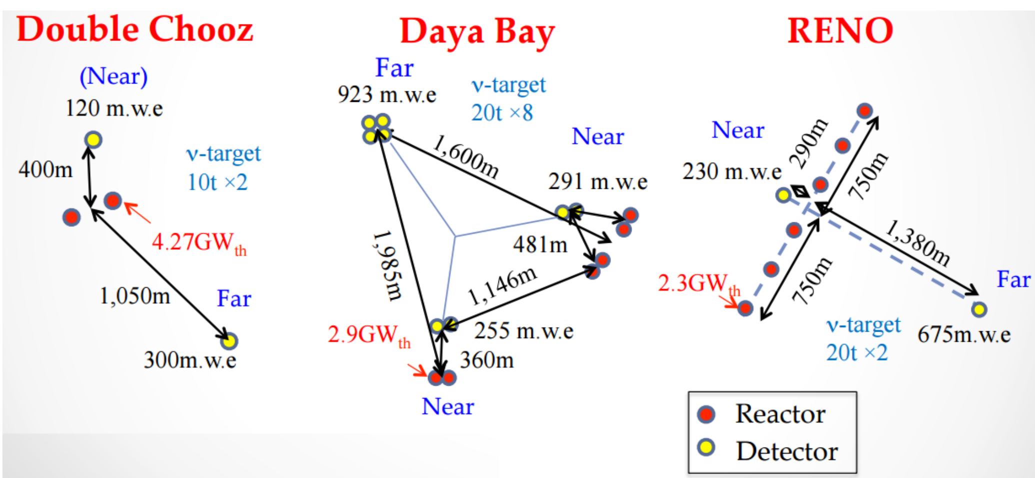

Figure 78: Currently Running θ_{13} experiments.

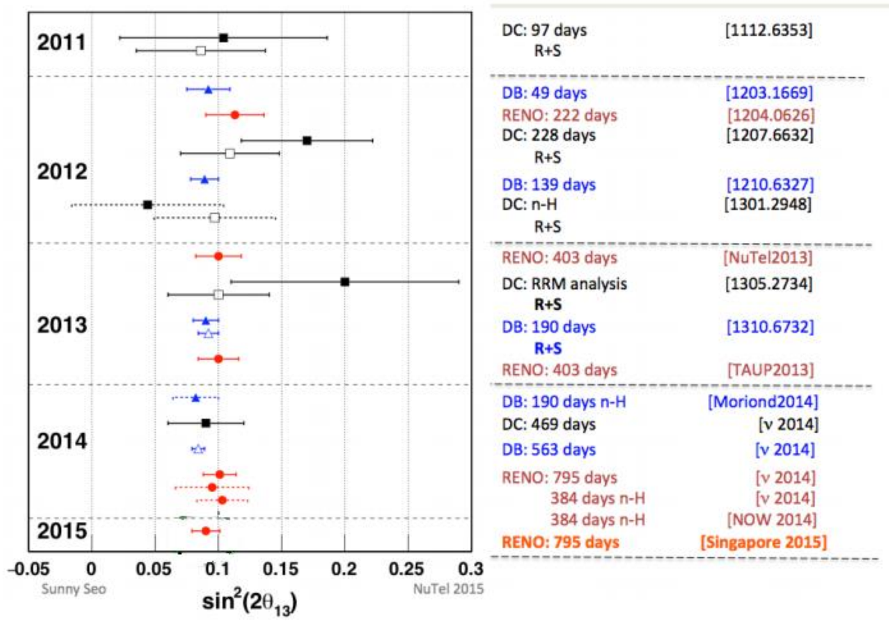

Figure 79: Timeline of World-Wide Reactor based neutrino oscillation. Open point indicate the result is from Rate+Shape fit while close point is from Rate Only fit. Dashed lines indicate n-H analysis while solid lines are for n-Gd only.

Chapter VII: Two Detector Results

In order to cancel systematic detection uncertainties and to measure the un-oscillated reactor flux, the final design for the Double Chooz consists of two identical detectors. In this chapter I describe similarities and differences between the two detectors and show the physics capabilities of a two detector system.

Two detector sensitivity

Using two identical detectors allows the error on $\sin^2 2\theta_{13}$ to decrease by about a factor 2 after three years of data. The projection in Figure 80 was made assuming that the cosmogenic backgrounds were 5x larger in the Near Detector (ND) as the total muon rate was expected (and is confirmed) to be 5x larger. Systematic detection uncertainties are largely suppressed in the two detector phase.

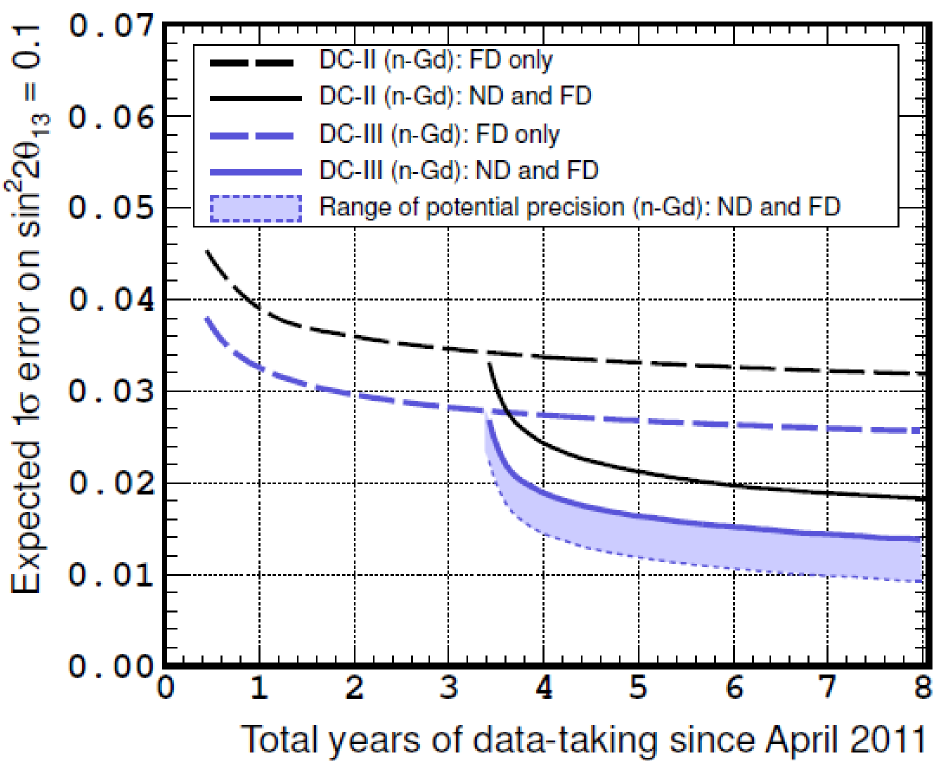

Figure 80: Projected sensitivity with near and far detector. Assumed cosmogenic backgrounds are scaled with the increased muon rate in the near detector.

Near-Far Detector Similarities

The near and far detectors were constructed as identical as possible. They have identical geometries and were constructed using the same methods and materials. The similarities can be seen in the low energy singles spectrum where muon and muon effects have been removed as well as Light Noise (Figure 81). The remaining spectrum is dominated by radioactivity and is normalized in both detectors to the total rate. Most notable is the consistent energy response of the 2.6 MeV gamma from ^{208}Tl. Another demonstration of the consistent Energy response is seen in Figure 82 from the 2.2 MeV capture of neutrons on Hydrogen and the 8 MeV capture of neutrons on Gadolinium. Both figures Figure 81 and Figure 82 are made using 1 hour of data. The rates of after muon events seen in Figure 82 arises from the difference in muon rate between the near and the far detectors.

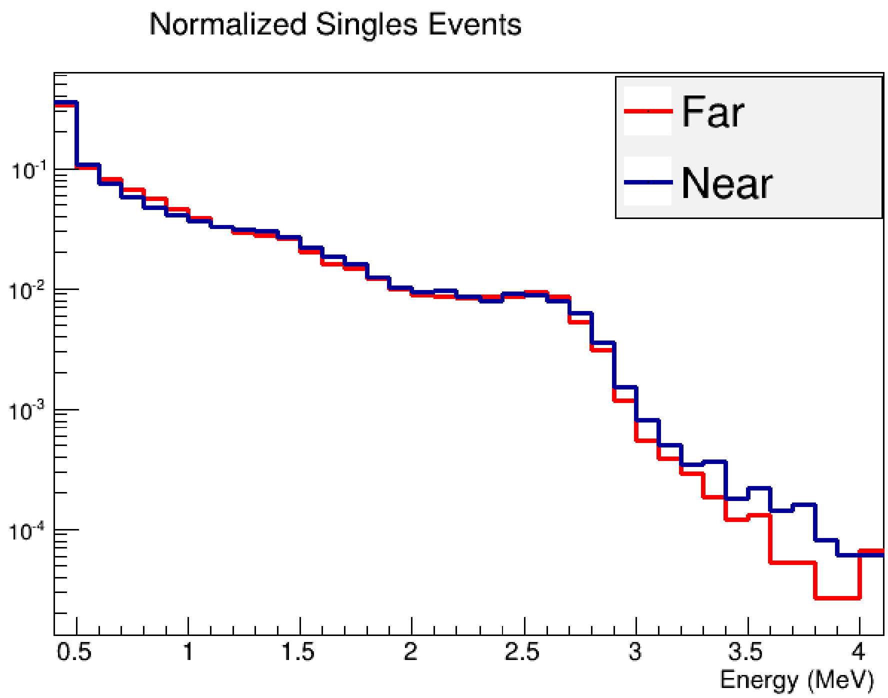

Figure 81: Low Energy Singles in the Near and Far detector taken from two 1 hour runs and normalized to the total singles rate.

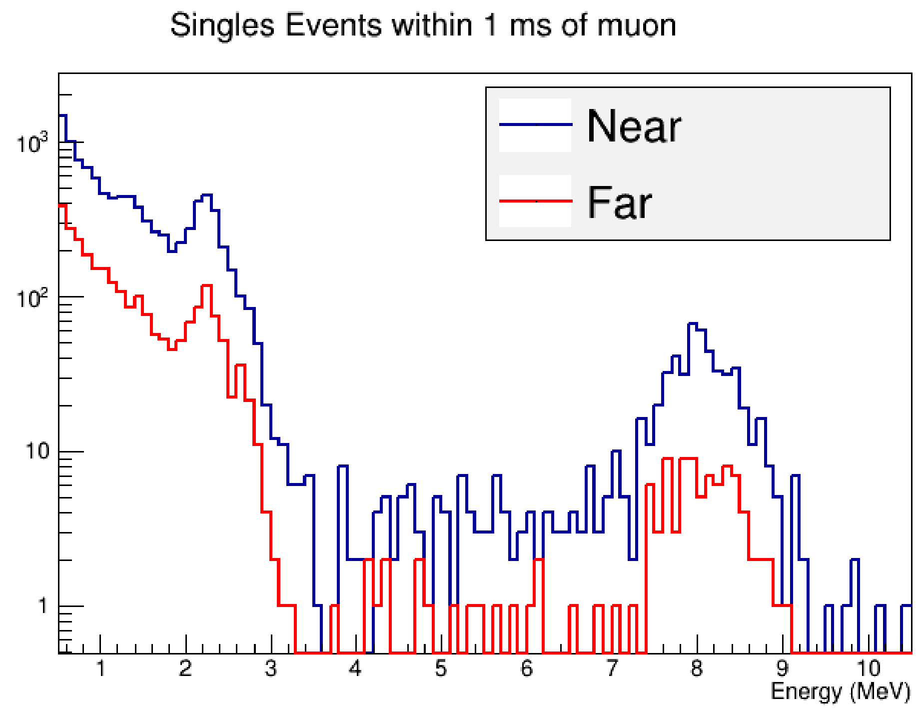

Figure 82: Singles within 1 ms after a muon. Identical Energy response is seen in near and far detectors.

Near-Far Detector Differences

Muon rates are notably different in the near and the far detectors. At a depth of 120 m.w.e. the near detector has a muon detection rate of 244 Hz where the far detector at a depth of 300 m.w.e. detects muons at a rate of only 48 Hz. The high rate of muons and the subsequent 1 ms veto after the muon lead to a detector dead time of 20% where the far detector has a dead time of only 5%. For the first few years of running the Double Chooz result will be statistically limited, therefore it would be advantageous to reduce this detector dead. I will address my contribution to this are in the section entitled "Optimizing Muon Veto".

As a corollary from the increased muon rate, the backgrounds that are created by cosmic rays are increased in the Near Detector. The exact rates have not been determined but it is expected to roughly scale with the number of muons.

As mentioned in the section "Light Noise" in Chapter IV. The PMT bases of the near detector were covered with black plastic in an effort to reduce light noise. This was largely effective as can be seen comparing the rate of light noise. The current rate of Light Noise in the far is 280 Hz up from the original rate of 30 Hz in 2011. The rate of light noise in the near detector is <5 Hz. Of this 5 Hz about 4 Hz has characteristics that are only seen in the near detector which I will call top buffer events.

There is a striking asymmetry in the near detector that prompted further investigation (Figure 83). Samples were taken of the buffer liquid and analyzed. The optical and chemical properties confirmed that the buffer liquid contained PPO and bis-MSB. These compounds should not be in the buffer liquid but they were present in the gamma catcher and inner veto liquids. They were not present in the tank used for filling. The source of the contamination is unknown, but it suggests a leak between the buffer and gamma catcher and/or inner veto. It is not known if there was a one-time spill or an ongoing leak between these volumes. The buffer top events can be explained if there is scintillator in the buffer that is located at the top of the detector. Radioactivity in the PMT glass will create light in the buffer, causing the detector to trigger. In this scenario event vertexes will be located near the PMTs and that is what is observed (Figure 84). What is puzzling is why these events are not observed on the bottom PMTs. It seems to suggest that the scintillator within the buffer is not mixing but rather floating on top the buffer liquid. These top buffer events are under on-going scrutiny, but since they are easily identified as light noise they do no effect the neutrino selection.

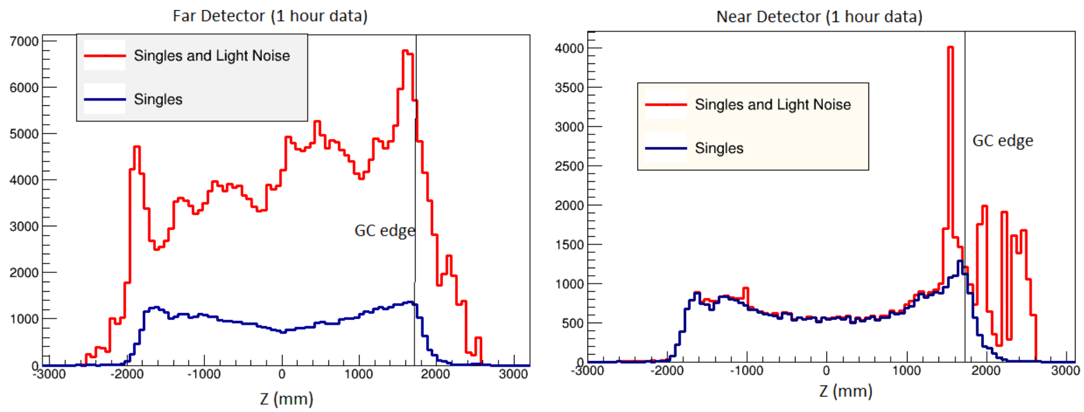

Figure 83: (left) Singles and Light Noise events in Far detector from a one hour run. (right) Singles and Light Noise in Near Detector for one hour run. Events which satisfy light noise cuts are mostly occurring in the top of the detector in the near.

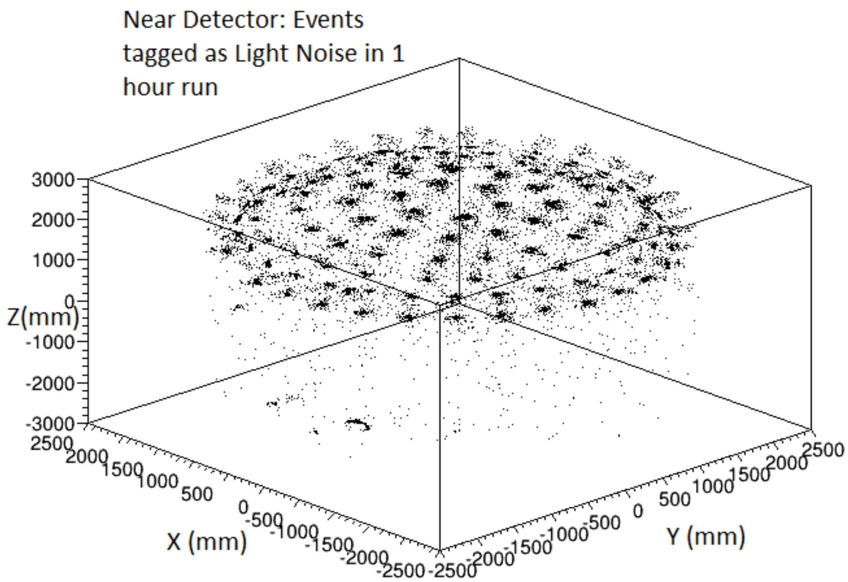

Figure 84: Vertex of Light Noise events in 1 hour run of Near Detector. Events are reconstructed at the face of individual PMTs in the top of the detector.

Uniformity correction maps (Figure 34) which correct the energy scale depending on the position within the detector are different between the detectors. The uniformity maps correct for geometrical acceptance and scintillator properties. Since the geometry of the two detectors is identical the differences in the maps must arise from differences in the scintillator. It is known that there is contamination of GC or IV liquid in the Buffer at the level of ~1000 liters. One can imagine that there is also buffer liquid in the GC or IV. If it is in the GC then there will be an additional effect on the uniformity maps. Preliminary uniformity maps for the near and far detector show slightly different behavior which can arise from differences in the liquids (Figure 85).

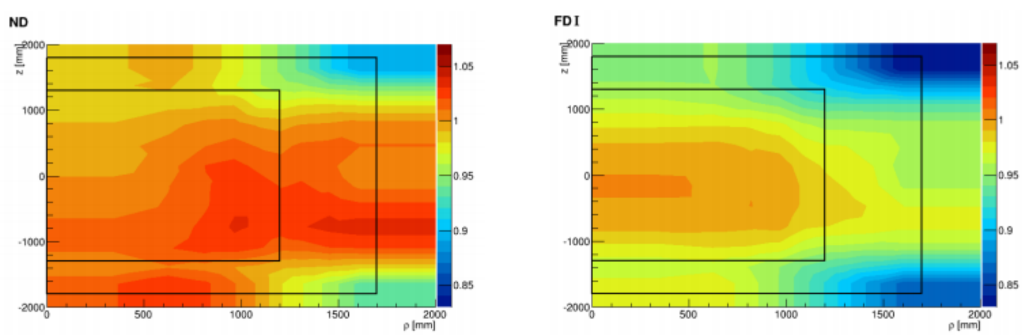

ND: 1 Month data Map

FD: ESv6 Map (FD-I map)

Figure 85: Uniformity correction maps for Near and Far detector. Differences are due to difference in scintillator properties.

Commissioning the trigger

Before the near detector came online it was determined that the extra data flow would tax the data migration system. The far detector was producing ~55 Gb of data per hour and the additional expected rate from the near detector was ~100 Gb per hour. The bulk of the data is from the 500 MHz 14 bit flash ADC. As a baseline the waveform from every PMT was recorded for every event, but for the majority of the events only a small amount of the data encoded in the waveforms was useful. To reduce the total data flow new triggering conditions were proposed and tested. The updated trigger condition is called Dynamic Data Reduction (DDR).The DDR trigger included additional logic conditions into the trigger firmware to sort events into categories where the full waveform was recorded (such as physics events) and categories where only a small part of the information in th waveform would be stored. For example, when the Inner Veto triggers but the inner detector does not, there are empty waveforms recorded from every detector PMT but only the Inner veto PMTs hold any information.

During the DDR studies it was found that a significant fraction of detector triggers were cause by after pulsing of the PMTs. After pulses occur when charged ions are accelerated within the tube causing current signals a few microseconds after the initial muon signal. The goal of the trigger condition was to preserve neutron capturing events after the muon while neglecting the after pulses. Another confounding factor was that after large energy depositing muons the trigger could be dead for a few tens of μs while the electronics recovered from the charge saturation. A goal of the new trigger was to reduce the dead time cause by large energy deposits and reduce the triggering caused by after pulsing. The new trigger should preserve neutron capture signals that occur after muons because they are useful tools for calibration and a good way to tag muons that likely produce ^{9}Li.

During the commissioning phase three trigger configurations were tested: FDI, DDR, and MOD. The FDI was the baseline trigger condition. The DDR trigger raised the triggering threshold after muons for 50 μs to ~5MeV from the normal ~0.4 MeV (Figure 86). The MOD trigger used the same setting as FDI but included a hardware modification where a capacitor was included on every channel to reduce the time it took for the baseline to recover. I tested the performance of each trigger as it applied to the ability to tag neutrons after the muon. To determine neutron captures I defined Energy windows where for n-H and n-Gd then examined the time structure of events satisfying these conditions (Figure 86). The n-H and n-Gd should look like two exponentials with a flat background. One exponential comes from neutrons capturing in the Target with a lifetime of 30 μs the second exponential comes from the 200μs lifetime of neutrons in the gamma catcher. The FDI trigger condition is the worst for Gd because of the deadtime that occurs around 30 μs. I determined the total number of neutrons capture per hour for all three trigger configurations and concluded that the MOD trigger was the best for detection neutrons (Table 6). Although the MOD was the best trigger condition it was decided to use the DDR trigger to avoid adding additional hardware to the detector that could potentially fail.

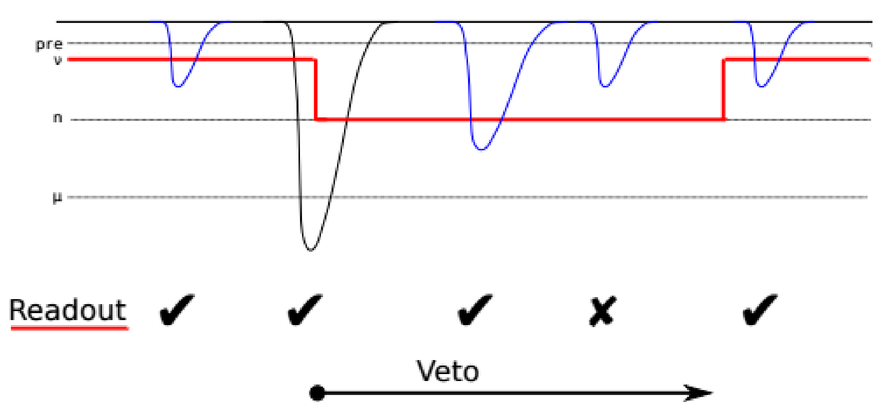

Figure 86: Schematic of the DDR trigger. The trigger threshold is increased for 50μs after a muon and then returns to the nominal level.

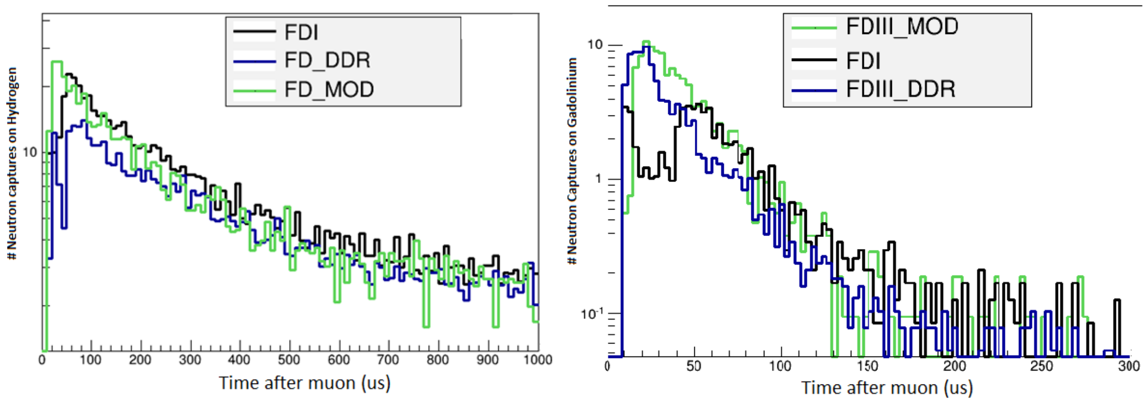

Figure 87: Performance on trigger configuration. Hydrogen captures (left) and Gadolinium captures (right). Both DDR and FDI triggers show decreased neutron detection efficiency compared to MOD trigger.

Table 6: Neutrons detected per hour for various of trigger conditions

Trigger condition	n-H captures per hour (10-1000us)	n-Gd captures per hour (10-30us)	Total neutron captures per hour
FDI	395	70	465
DDR	269	99	368
MOD	398	126	524

Optimizing Muon Veto

The muon rate of 244 Hz in the near detector with the 1 ms after muon veto is responsible for a 20% dead time. In the far detector the muon rate is 5 times lower so the 1 ms veto was never optimized to maximize the IBD signal. The 1 ms veto time was chosen conservatively to ensure no extra background associated with the previous muon entered into the IBD sample (Figure 88). I have examined the source of this muon correlated background and proposed a new cut which adds an additional 10% to the IBD candidates in the near detector while introducing an additional small background. I have completed this study with the first month of data available from the near detector. I demonstrate the procedure to be used once more data becomes available.

The source of the muon induced events is predominantly multiple captures of neutrons created by the spallation process. The prompt energy of the events just after the muon are centered on either the 8 MeV Gd capture peak, or the 2.2 MeV H capture peak (Figure 89). Also visible is a high energy component from 10- 20 MeV at times less than 50 µs after the muon this is made from stopping muon and /or fast neutron events. The difference in capture time is visible for n-Gd and n-H in that all Gd prompts occur within the first 100 µs while the n-H captures extend to ~100s of µs. The same information can be seen as a projection onto the Energy axis is shown for several time windows (Figure 90). In the first 150 µs the prompt is dominated by n-Gd and n-H while in later time windows the prompt spectrum contains a reactor neutrino component with an additional n-H component at 2.2 MeV. From Figure 89 and Figure 90 it is clear that there is some hope to salvage neutrino events in the time window > 150 µs from the muon.

The strategy I will employ to reduce the dead time due to muon veto will involve classifying muons into two categories and then applying a separate veto time for each. I classify muons as Veto Muons and Buffer Muons. Veto Muons are defined such that their Energy in the Inner Detector is < 60 MeV which means that the muon passed through < 30cm of scintillator in the Inner Detector. This is possible if the muon only clips the corner of the gamma catcher liquid. Muons which have > 60 MeV deposited in the Inner Detector must have passed through scintillator and therefore are more likely to create neutrons that could capture on Gd leading to additional muon related backgrounds.

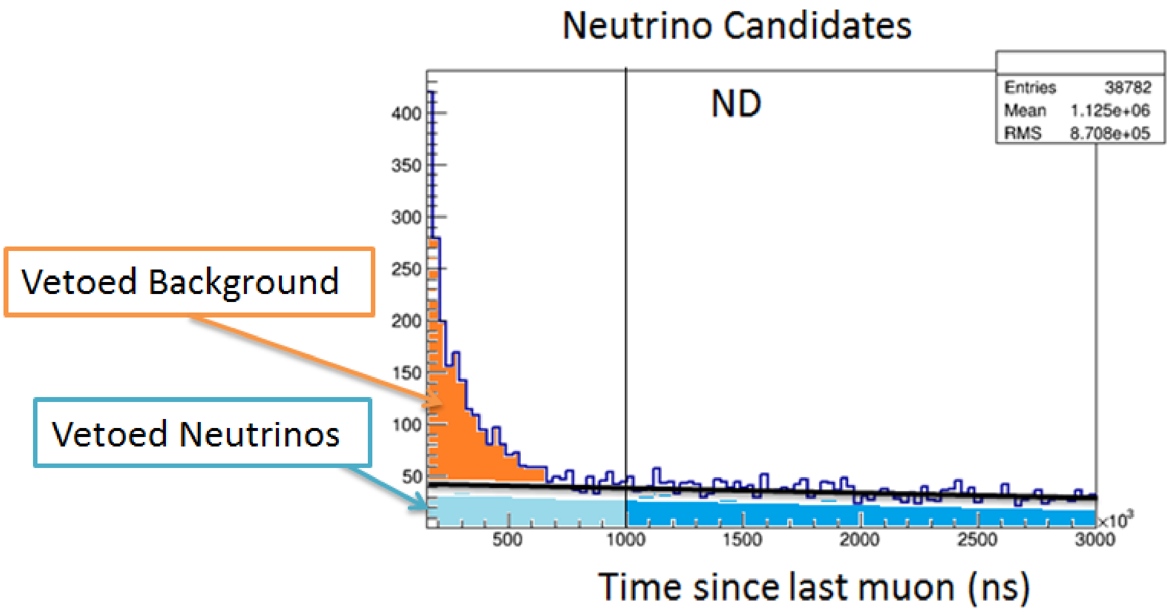

Figure 88: Neutrino candidates in one month data set of near detector. Events to the left of the horizontal line at 1 ms are vetoed by the after muon veto. A clear excess highlighted in orange is seen after the muon.

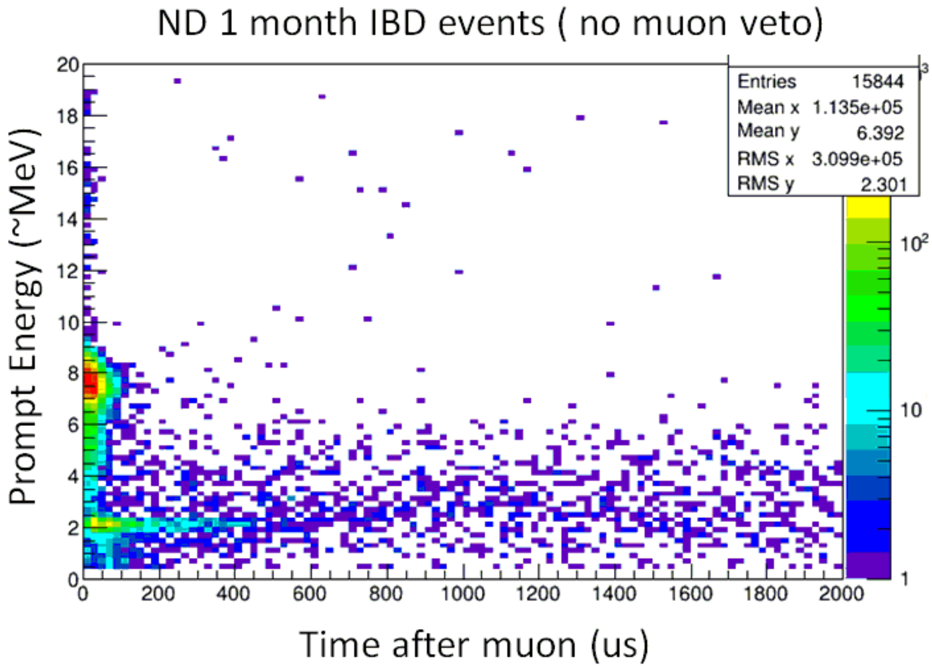

Figure 89: Time after muon verse prompt Energy of IBD candidates. Neutrinos coming from the reactor should provide a constant background as seen for times > 1 ms . Muon induced IBD candidates are seen at times < 1 ms.

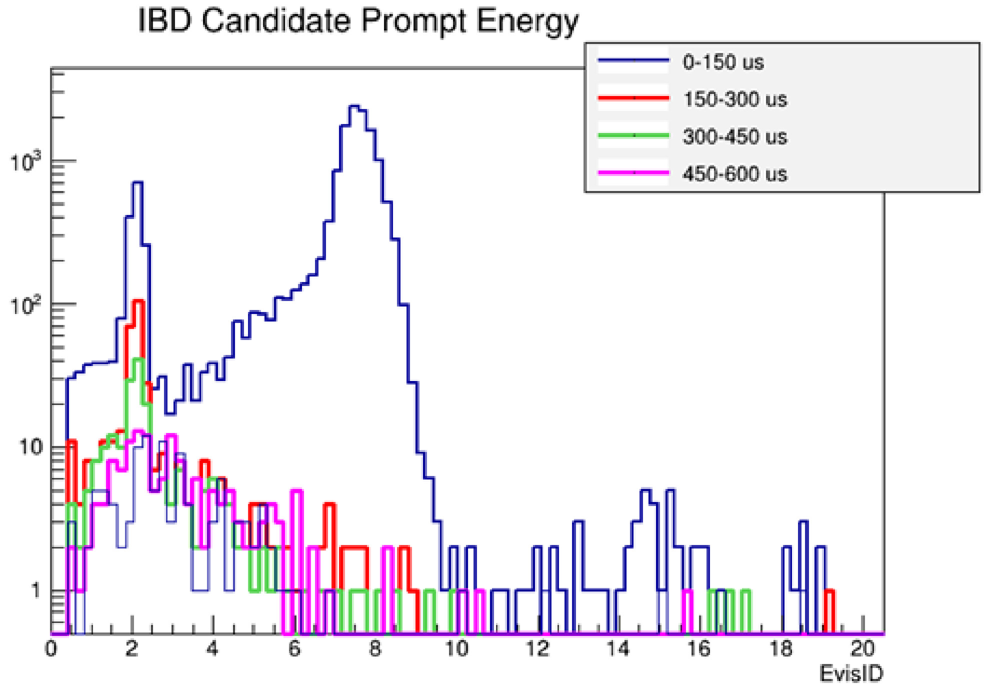

Figure 90: IBD prompt candidates in 1 month data of Near Detector. Different color histograms correspond to different time windows after the previous muon.

Figure 91 shows the difference that Veto and Buffer Muons have on IBD creating backgrounds. Both the Buffer Muon and the Veto muon induce some IBD signals after interacting in the detector but the buffer muon induces a much larger magnitude of events seen in the large excess a short time after the muon. The nature of this background is visible in Figure 92 where the energy spectrum shows a 2.2 MeV n-H capture on top of a reactor neutrino spectrum. Again the n-H background dominates the at short times after buffer muons while the reactor spectrum dominates at short times after Veto muons.

To make a compromise between adding detector live-time and increasing the n-H background, I chose to maintain the 1 ms veto after buffer muon but to shorten the veto after Veto muons to 0.5 ms. This new muon veto definition adds 230 IBD candidates to the existing sample of 2497 candidates in 24.3 days of live time(). This increase of 9% comes at a cost of adding an additional background to the IBD spectrum. I estimate the size of this additional background to be ~10 events which corresponds to ~ 0.5 events /day. To fully characterize the cost/benefit of this altered muon definition and to fully optimize the times of the vetoes I will need more statistics which should be available in the coming weeks.

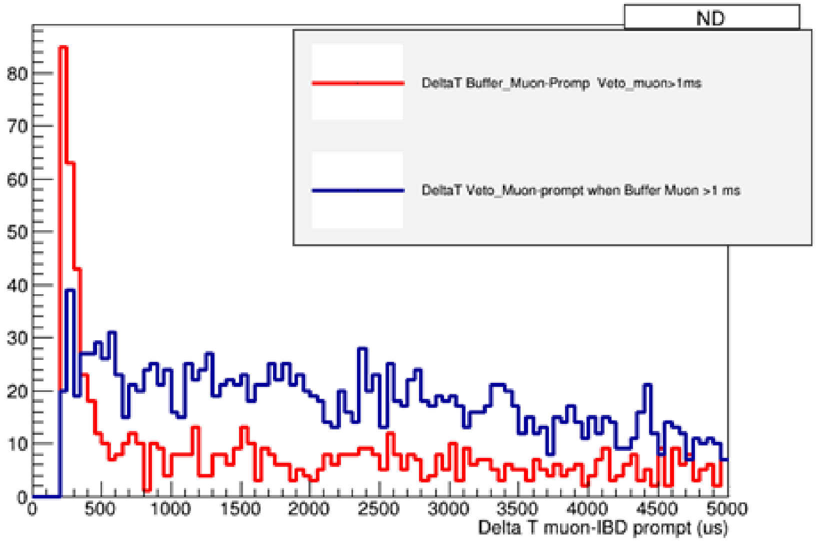

Figure 91: ΔT distributions for the two muon classes and the IBD prompt. (blue) Veto Muon plotted when Buffer Muon veto of 1 ms is applied and (red) Buffer Muon plotted when Veto Muon veto time of 1 ms is applied.

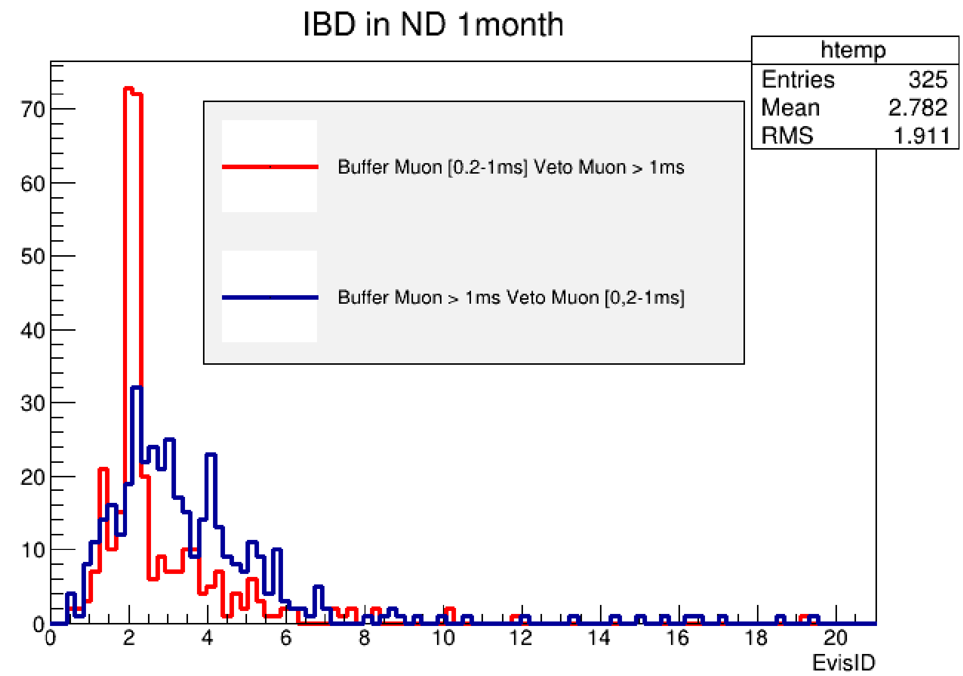

Figure 92: Energy Spectra for alternative muon veto definitions.

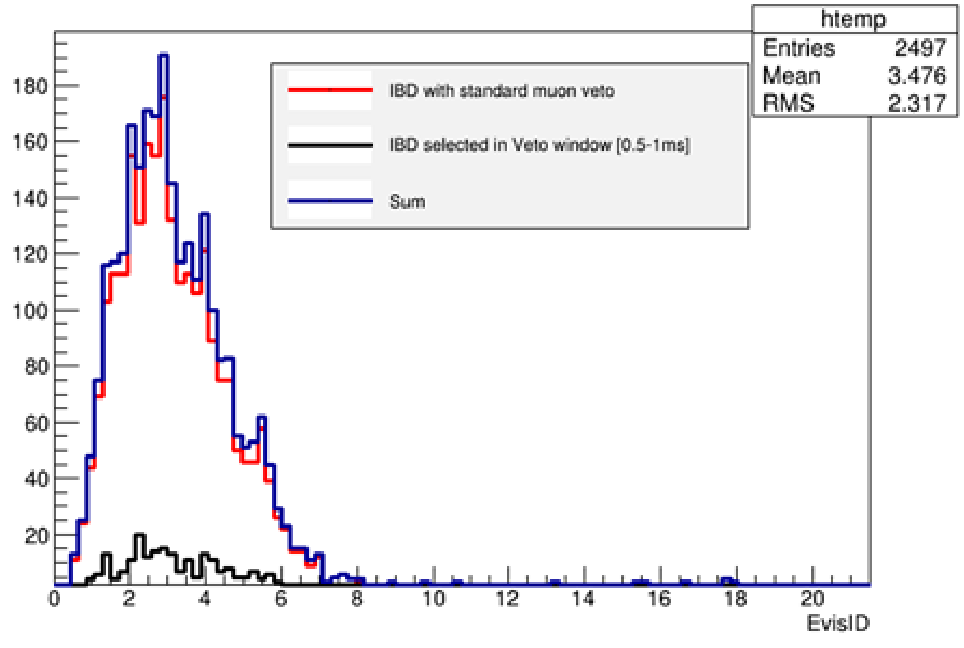

Figure 93: IBD candidates from the 1 month sample of the Near Detector. Standard IBD candidates are shown in red with the additional candidates from a shortened muon veto time in black. The sum of the two is in blue.

Chapter VIII: Detecting a Hidden Reactor with Two Identical Detectors

Knowledge of neutrinos and their properties has drastically increased in the last few decades. A natural next step for the field of neutrino physics is to explore practical applications that might rely on these elusive particles. One such application is to use neutrino detection as a tool to identify breaches in nuclear non-proliferation agreements. The idea is that a nation may secretly build a nuclear reactor to produce the raw material for constructing nuclear weapons. No amount of shielding can hide the neutrinos from that reactor and so if the neutrinos can be detected the existence of the hidden reactor could be uncovered. A few groups [35,36,37] have purposed detection systems that could be used to detect these hidden reactors. These groups propose a system of four neutrino detectors which would be used to locate a hidden reactor. I will use the Double Chooz detectors as an example to explore the differences between using a single detector and two detectors in regards to locating a nuclear reactor.

General formulism

A single neutrino detector can uncover changes in detection rates which are associated with a reactor being on or off (Figure 94). Backgrounds mimicking reactor neutrinos are due to cosmic rays and are stable in time therefore any change in detection rate can be attributed to a reactor. If a large number of neutrinos are detected then it is possible to determine the direction of the neutrino source. This requires a precise vertex reconstruction. On average the positron travels 0.05 cm before it is annihilated and the neutron travels ~2 cm before it is captured. The averaged direction between the prompt and delay points toward the reactor. With the 17,351 events in the Double Chooz Far detector the position of the reactors could be located with a 10 degree accuracy (Figure 95). Another method for determining a reactors distance is to look at the shape differences in the observed and predicted spectrum. Since neutrino oscillation depends on L/E the shape of the oscillated spectrum contains information about L, the distance away from the reactor. Again this oscillated shape method is only useful when you have detected a large number of neutrinos. In order to detect a hidden reactor it is useful to have methods that do not depend on large statistics since in real world applications they will not be available. Instead, I want to explore a method to help localize a hidden reactor based only on rate information and can be used with small statistics.

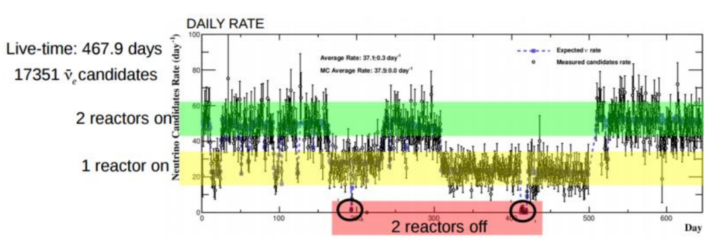

Figure 94: Neutrinos detected per day with the Double Chooz Far detector.

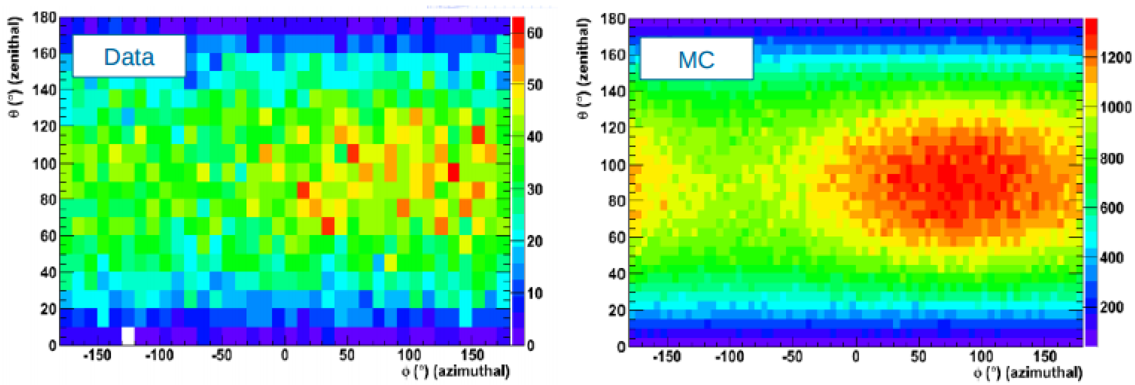

Figure 95: Direction of the vector that points from delay to prompt for the Double Chooz Far detector. (left) is data points while (right) shows Monte Carlo prediction with higher statistics.

Let's suppose a single detector observes a rate above background of R_1. The possible source of R_1 can be nuclear reactor, which ranges in power from 10 MW to ~10 GW , 3 orders of magnitude. The corresponding location can be constrained because the detection rate ∝ reactor power / $\mathbf{r}^2$ where **r** is the distance from the reactor to the detector. The corresponding possible locations range from $\mathbf{r}_{min}$ to $1000^{1/2} \times \mathbf{r}_{min}$ where $\mathbf{r}_{min}$ is the minimum distance your detector would detect a neutrino rate of R_1 from a 10 MW reactor. Therefore the detection of a neutrino signal does not give any information about the reactor power and does not tightly constrain the reactor location.

Now suppose you have two identical detectors which measure R_1 and R_2, the neutrino rate above background at detector 1 and 2 respectively. Since the detection rate is proportional to the power and distance away with two measurements we can constrain the location of the hidden reactor to lie on a circle and the power of the reactor is constrained depending on the geometry of the circle. The proof of this is as follows: the ratio of the detection rates are related to the ratio of the distances to the reactors by:

$R_1 \propto \frac{1}{r_1^2}$ and $R_2 \propto \frac{1}{r_2^2}$

Equation 6

$$A = \sqrt{\frac{R_1}{R_{2}}_{1}} = \frac{r_2}{r_1}$$

Now define a grid such that the detector which measures a greater neutrino rate lies at (0,0) and the other detector lies at (0,-d) the possible location of the reactor is at (x,y). I can transform into Cartesian coordinates by:

$$r_1 = \sqrt{x^2 + y^2} \qquad r_2 = \sqrt{x^2 + (y+d)^2}$$

Substituting these definitions in to Equation 6 and rearranging yields:

A $\sqrt{x^2 + y^2} = \sqrt{x^2 + (y + d)^2}$

Now square both sides and rearrange to yield:

$$(A^2 - 1)x^2 + (A^2 - 1)y^2 - 2yd - d^2 = 0$$

This equation can be solved by completing the square to obtain:

Equation 7

$$(x - 0)^2 + \ (y - \frac{d}{A^2 - 1})\text{^}2 = \frac{d^2A^2}{(A^2 - 1)^2}$$

Equation 7 defines a circle centered at

$(0\,, \frac{d}{A^2 - 1})$

With a radius

$$r = d\frac{A}{(A^2 - 1)}$$

To visualize the result I show possible solutions depending on the value of A (Figure 96). The one exception to the rule above is when R_1=R_2. In this case the solution is not a circle but a line that is equidistant from R_1 and R_2.

For a given value of A, whose possible reactor locations define the specific circle. The reactor power can be constrained. The largest possible reactor lies at the point on the ring furthest from the detector while the smallest possible reactor lies at the point closest to the detector (Figure 97). The strength of this constraint depends on the specific value of A that is observed which will be demonstrated using the Double Chooz detectors as an example.

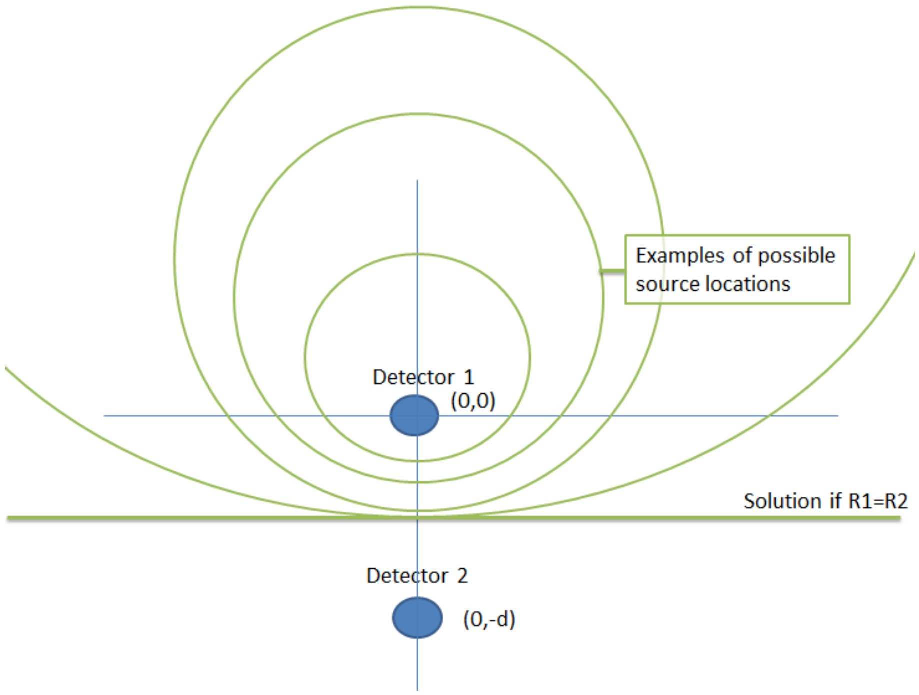

Figure 96: Green circles show possible reactor locations for different values of A.

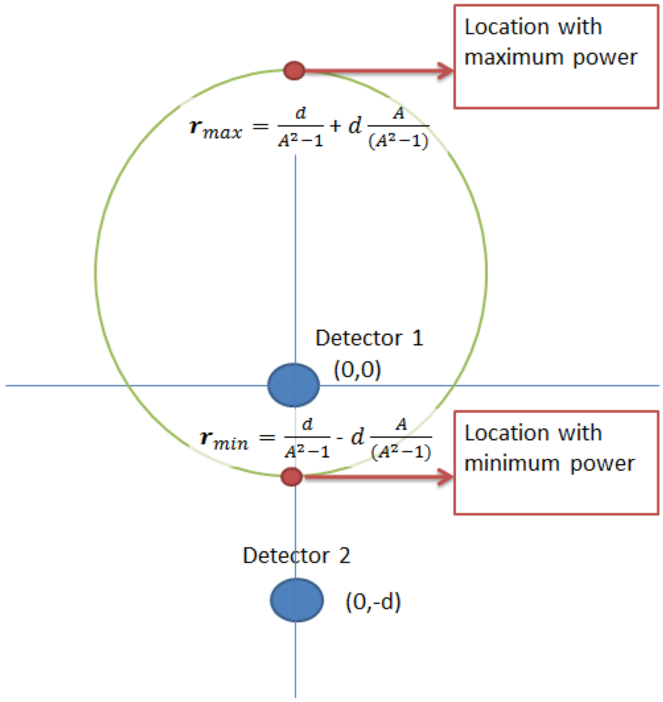

Figure 97: Schematic showing the position of reactors with possible minimum and maximum thermal powers.

Example using Double Chooz

To demonstrate the performance of a two detector system in a real world detector, I will use the first available data set of the near and far Double Chooz detectors. The first step will be to do a neutrino analysis to determine the rates at both detectors, next a circle of possible source locations will be defined and finally an upper and lower limit on the reactor power will be obtained.

Neutrinos are selected in the near and far detectors by with the following procedure:

1) Veto muons and 1 ms after muon, where a muon is defined as either >20 MeV Energy deposition in the ID or 30,000 (50,000) DUQ in the IV for the near (far) detector.
2) Veto LN events witch satisfy the following cuts*:
    a. Qmax/Qtot > 0.12
    b. Qdiff >50,000 DUQ
    c. RMSTstart>60 OR QRMS>1044-18*RMSTstart
3) With the remaining sample select events which contain a prompt and delay pair which satisfies the following
    a. ΔT between prompt and delay is in the interval [0.5,150 μs]
    b. Prompt Energy [0.5,20 MeV]
    c. Delay Energy [4,10 MeV]
    d. Delay Energy < 0.0833 exp(Delay FuncV/1.3) (this cut rejects delay events that are not point like energy depositions, i.e. Stopping muons and multiple scattering fast neutrons)
    e. Reject the event if there is any valid trigger in the [-200,600 μs] time window around the prompt other than the delay
    f. Reject events where the Qmax/Qtot of the delay is <0.03 (this cut removes delay events which occur in the buffer, which is only a problem for the near detector because of scintillator in the buffer oil)

The resulting neutrino candidates (Figure 98) and the detector live times for this data set are used to define the neutrino detection rates. The near detector, with 24.3 live days, has a neutrino detection rate of 118.1 (neutrinos/day) while the far detector with 36.9 live days yields a neutrino rate of 22.4 (neutrinos/day). Using Equation 6 these rate result in A=2.30±0.09 where only statistical errors of the counting rate are considered in the error calculation. The distance (d) between the Double Chooz detectors is 1348m so that from Equation 7 the circle which defines the possible locations of the reactor is centered at (0,314±24) and has a radius of 722±90 m. A schematic picture of this result shows that the actual location of the reactor (R1) is within 1 σ of the predicted location (Figure 99).

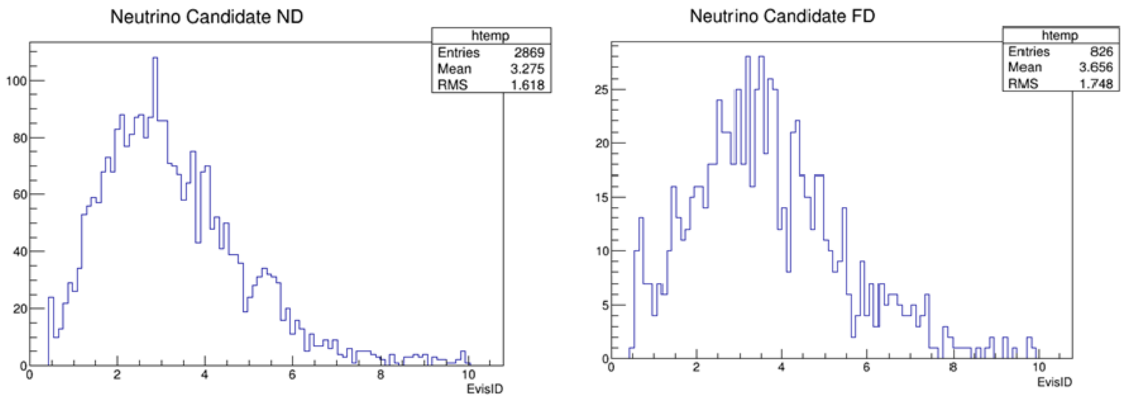

Figure 98:Prompt Energy (MeV) of neutrino candidates from the preliminary "1 month" data set.

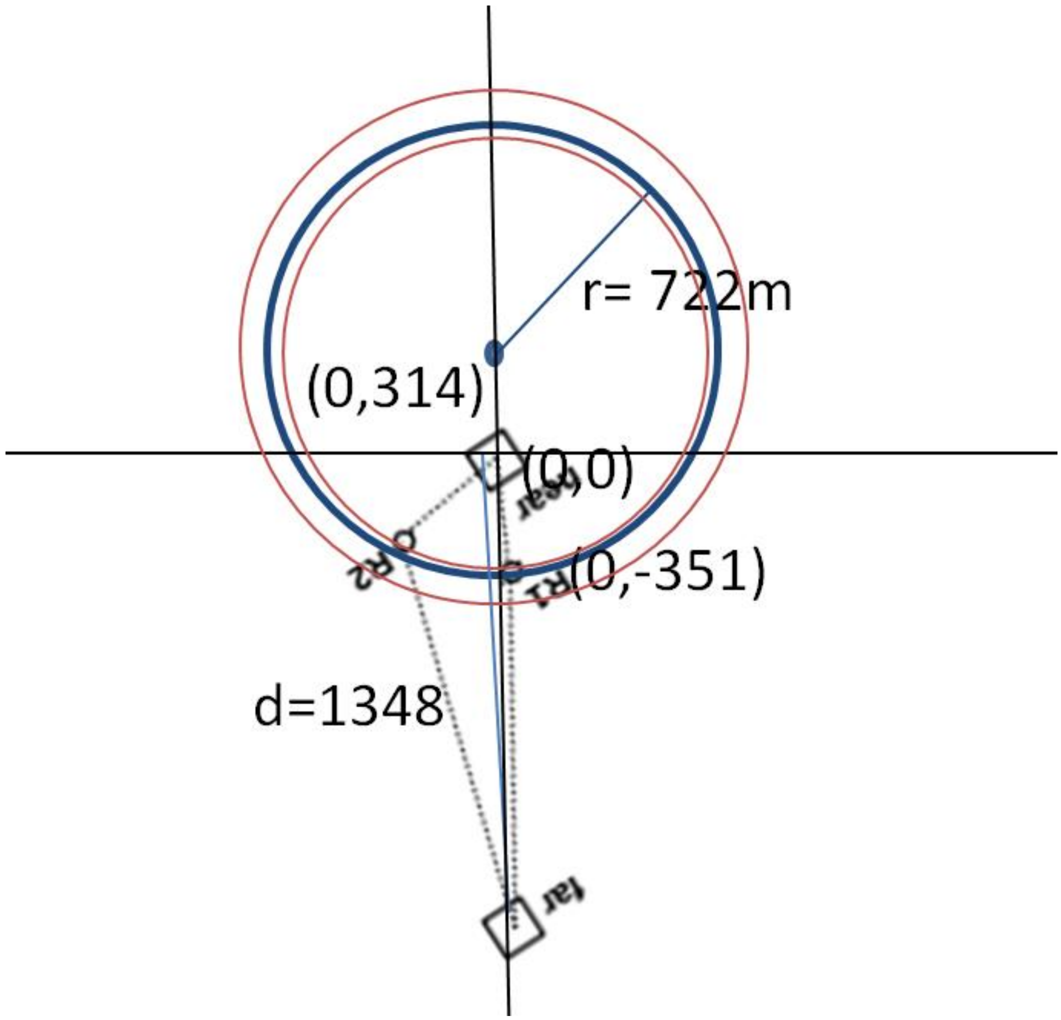

Figure 99: Schematic of the predicted location of the hidden reactor (blue line) with 1 sigma uncertainties (red lines) based on the rate measurement overlaid with the actual location of the reactors (R1 and R2).

Once we have the possible locations of the hidden reactor we can put limits on the reactor power. Within the one sigma statistical uncertainty the minimum reactor power would be located at the nearest possible location of (0, -342 m) and the furthest possible location corresponding to the maximum possible reactor power would be located at (0, 1150 m). The absolute scaling depends on detection efficiency, reactor spectrum, target protons and neutrino cross section. In principle this can be calculated using a general reactor spectrum and any detector geometry. Since I know the power of the Chooz reactors and their distance from the detector I can determine the scaling factor for the Double Chooz detector. At the far detector Observed neutrino rate = C*power/r^2. Using a rate of 25 neutrinos/day, a distance of 1050 m and a reactor power of 4.27 GW results in a scaling factor C= 6.45×10^5 (neutrino m^2)/(day GW). Using this scaling factor at the minimum and maximum distances contained within the 1 σ uncertainty of 342 and 1344 m yields a reactor power between 2.14-24.2 GW thermal.

In the above calculation I have ignored background contributions and oscillations due to θ_{13}. For Double Chooz total background rate is <10% of the neutrino signal and likewise the disappearance due to oscillations is also a 10% effect in the far detector and much less than that at the near. Neutrino oscillations become more important at larger distances, but since neutrino mixing angles and Δm^2 values are measured this effect is accountable.

One detector verse two discussion

I have demonstrated that by detecting a neutrino flux with two detectors you can reduce the possible source locations and the possible hidden reactor operating powers. In a real world application the challenge would be to construct two detectors that would measure a neutrino flux. It is possible that neither detector could discern a signal above the background. In this case the appropriate question is: what is the exclusion area of even the smallest reactor? The number of neutrinos detected scales linearly with the target volume as does the area excluded, so having two detectors of half the size excludes the same area as one detector that is full sized. The other benefit to operating smaller detectors is that the muon flux depends exponentially with the depth so that a smaller detector could be operated at a shallower overburden, saving construction cost. The drawback is that operating multiple detectors is that there are more PMTs required to maintain the same photocathode coverage. If your choice is between one detector of volume V or two detectors of volume V/2 the two detectors will require $2\times(1/2)^{2/3}$ or ~125% the number of phototubes. This is because the volume scales as R^3 so that the radius of a sphere required for ½ of volume is $(1/2)^{1/3}$ but the surface area requiring photo tubes scales with R^2.

Chapter VIII: Conclusions

Double Chooz has measured $\sin^2 2\theta_{13}$ = $0.090^{+0.032}_{-0.029}$ with one detector for 467 live-days. This result is in agreement with the competitive measurements of Daya Bay and RENO, however the results were published first by Double Chooz. The result has been checked and confirmed with the sample where the neutron captures on Hydrogen. Double Chooz observes > 2σ deviations from expected reactor spectrum shape in the region > 4 MeV visible energy which matches measurements from other medium baseline reactor experiment (RENO and Daya Bay). This deviation in the predicted shape is likely due to an overestimate of the neutrino spectrum that is emitted from the nuclear reactors. Double Chooz expects to have a high precision measurement of the un-oscillated spectrum with the near detector which will confirm or deny this hypothesis. I was part of and contributed to the success and publications of the Double Chooz collaboration.

The near detector has been built and commissioned since January 2015. I have contributed to the installation effort in many ways. I have done everything from being responsible for the quality assurance of every PMT installed to cleaning and connecting hundreds of cables. I was one of the first to ensure data quality of the finished detector by doing commissioning quality checks. Despite some small differences between the near and the far detectors, the data quality from the near detector is excellent. With two quality detectors we will improve systematics. I consider this as my major contribution to the Double Chooz collaboration.

Future applications of neutrino detectors may include reactor monitoring. I have devised a method to locate a hidden reactor using two identical detectors. I have used initial data from the Double Chooz near and far detectors to demonstrate the capabilities of the method. The method relies on measured rates and can be used in cases with small statistics, which makes it applicable to future reactor monitors that may only detect a handful of events.

Given a few years of statistics the error on $\sin^2 2\theta_{13}$ in Double Chooz is expected to shrink to 0.015. At this high precision the recent results from Daya Bay and RENO will be tested and the combination of all three will yield high confidence to the worldwide community and enable future test of the CP violating phase. Precision measurement techniques developed by Double Chooz will guide future short baseline experiments (e.g. PROSPECT) and detectors designed for nuclear non-proliferation (e.g. WATCHMAN).

List of References

1. http://pdg.lbl.gov/2013/reviews/rpp2013-rev-neutrino-mixing.pdf
2. Y. Abe et al. [The Double Chooz Collaboration]. Indication for the disappearance of reactor electron antineutrinos in the Double Chooz experiment. *Phys. Rev. Lett.* 108:131801, 2012.
3. Pauli's Letter to Tubingenr: https://cds.cern.ch/record/83282/files/meitner_0393.pdf
4. F. Reines. Reines-Cowan Experiments Detecting the Poltergeist. *Los Alamos Science Num.* 25, 1997.
5. J. N. Bahcall, A. M. Serenelli, and S. Basu. New solar opacities, abundances, helioseismology, and neutrino fluxes. ApJ 621, L85 (2005)
6. Bruce T. Clevland et al. Measurement of the Solar Electron Neutrino Flux with the Homestake Chlorine Detector. ApJ 496, 505 (1998)
7. Raymond Davis, Jr. Solar Neutrinos. II. Experimental. Phys. Rev. Lett. Vol. 12 N 11 (1964)
8. Ahmad et al. [SNO collaboration]. Measurement of the Rate of ve+d→p+p+e− Interactions Produced by B8 Solar Neutrinos at the Sudbury Neutrino Observatory. Physical Review Letters Vol 87 N.7 (2001)
9. Ahmad et al. [SNO collaboration]. Measurement of the Total Active B8 Solar Neutrino Flux at the Sudbury Neutrino Observatory with Enhanced Neutral Current Sensitivity. Vol 92 181301 Physical Review Letters (2004)
10. Y Fukuda. [Super-Kamiokande Collaboration].Evidence for Oscillation of Atmospheric Neutrinos .Phys. Rev. Lett. 81, 1562 (1998)
11. M.H.Ahn et al.[K2K collaboration]. Measurement of neutrino oscillation by the K2K experiment Phys.Rev.D74, 072003 (2006)
12. K. Eguchi et al. [KamLAND Collaboration] First Results from KamLAND: Evidence for Reactor Antineutrino Disappearance. Phys. Rev. Lett.90 .021802 (2003)
13. T. Araki et al. [KamLAND Collaboration] Experimental investigation of geologically produced antineutrinos with KamLAND. *Nature* **436**, 499-503 (28 July 2005)
14. M. Apollonio. [CHOOZ Collaboration].Search for neutrino oscillation son a long base-line at the CHOOZ nuclear power station. Eur.Phys.J.C27:331-374 (2003)
15. F. Boehm et al. *[Palo Verde collaboration].* Final results from the Palo Verde neutrino oscillation experiment, , Phys. Rev. D64 112001 (2001)
16. Y. Abe et al. [The Double Chooz Collaboration]. Indication for the disappearance of reactor electron antineutrinos in the Double Chooz experiment. *Phys. Rev. Lett.* 108:131801, 2012
17. F.P. An et al. [Daya Bay Collaboration]. Observation of Electron-Antineutrino Disaaperance at Daya Bay. Phys. Rev. Lett. 108, 171803 (2012)
18. Soo-Bong Kim et al. [RENO collaboration]. Observation of Reactor Electron Antineutrino Disappearance in the RENO Experiment, Phys. Rev. Lett. 108 191802 (2012)
19. C. Aberle et al. Large scale Gd-beta-diketonate based organic liquid scintillator production for antineutrino detection. JINST 7 P06008 (2012)
20. T Masabara et al. Development and evaluation of 10-inch Photo Multiplier Tubes for the Double Chooz experiment. arxiv:1104.0786
21. T. Koblesky et al. Cathode Position Response of Large-Area Photomultipliers Under a Magnetic Field. arxiv:1109.4666

22. E. Calvo. et al. Characterization of large area photomultipliers under low magntic fields: design and performances of the magnetic shielding for the Double Chooz neutrino experiment. arxiv 0905.3246
23. *Y. Abe* et al. Waveform Digitiser of the Double Chooz Experiment: performance and quantisation effects on photomultiplier tube signals. *JINST* **8** P08015 (2013)
24. D. Dwyer et al. Spectral Structure of Electron Antineutrinos from Nuclear Reactors. arxiv 1407.128
25. Mueller et al. Improved Predictions of Reactor Antineutrino Spectra Phys.Rev.C83:054615,(2011)
26. Huber . Deteermination of antineutrino spectra from neuclear reactors. Phys.Rev.C84:024617,(2011)
27. K. Schreckenbach et al. Determination of the antineutrino spectrum from ^{235}U thermal fission products up to 9.5MeV , Phys. Lett. 160B, 325 (1985).
28. F. von Feilitzsch et al. Experimental beta-spectra from ^{239}Pu and ^{235}U thermal neutron fission products and their correlated antineutrino spectra. Phys. Lett. 118B, 162 (1982).
29. A. Hahn et al. Antineutrino spectra from ^{241}Pu and ^{239}Pu thermal neutron fission products. Phys. Lett. B 218, 365 (1989)
30. C. Bauer et al. Qualification Tests of 474 Photomultiplier Tubes for the Inner Detector of the Double Chooz Experiment. arxiv:1104.0758
31. T. Matsubara et al. Development and evaluation fo 10-inch Photo-Multiplier Tubes for the Double Chooz Experiment. arxiv:1104.0786
32. Y.Abe et al. [Double Chooz Collaboration]. Improved measurements of the neutrino mixing angle theta_13 with the Double Chooz detector, JHEP 10 (2014) 086
33. Y. Abe et al . [Double Chooz Collaboration]. First Measurement of theta_13 from Delayed Neutron Capture on Hydrogen in the Double Chooz Experiment, Phys. Lett. B723 (2013) 66-70
34. Y. Abe et al . [Double Chooz Collaboration]. Measurement of θ_{13} in Double Chooz using neutron captured on hydrogen with novel backfround rejection techniques. arxiv:1510.08937
35. M. Askins. et al. The Physics and Nuclear Nonproliferation Golas of WATCHMAN: A Water Cherenkov Monitor for Antineutrinos. arxiv:1502.01132
36. Thierry Lasserre et al. SNIF: A Futuristic Neutrino Proble for Undeclared Nuclear Fission Reactors. arxiv:1011.3850
37. E. Guillian. Far Field Monitoring of Rogue Nuclear Activity with an Array of Large anti-neutrino Detectors. arxiv: 0607095
38. V.N.Aseev et al. Upper limit on the electron antineutrino mass from the Troitsk experiment. Phys.Rev. D. 84 112003 (2011)

VITA

Ben Thomas Rybolt was born in Royston, GA. He spent his childhood in Chattanooga TN. He completed his undergraduate education at the University of Richmond where he earned a Bachelor's of Science in Physics. He started graduate school at the University of Tennessee in 2011 and earned his Ph.D in Physics in 2015.